ScuDo

Scuola di Dottorato ~ Doctoral School

WHAT YOU ARE, TAKES YOU FAR

Doctoral Dissertation

Doctoral Program in Mechanical Engineering (33^{th}cycle)

Structural Testing of Composite Crash Structures

By

Iman Babaei

******

Supervisor(s):

Prof. Giovanni Belingardi

Prof. Davide Salvatore Paolino

Doctoral Examination Committee:

Prof. Valentina Lopresto, Referee, Università degli Studi di Napoli Federico II

Dr. Pietro Russo, Referee, CNR Istituto per i Polimeri Compositi e Biomateriali

Politecnico di Torino

2021

Declaration

I hereby declare that, the contents and organization of this dissertation constitute my own original work and does not compromise in any way the rights of third parties, including those relating to the security of personal data.

Iman Babaei
2021

* This dissertation is presented in partial fulfillment of the requirements for **Ph.D. degree** in the Graduate School of Politecnico di Torino (ScuDo).

I would like to dedicate this thesis to my loving family
my parents ***Karamat*** *and* ***Zinat***
my sisters ***Elham*** *and* ***Rezvan***
and my brother in law ***Siamak***

Acknowledgements

The results of this dissertation have been mainly obtained within the framework of ICONIC project which has received funding from the European Union's Horizon 2020 research and innovation program under the Marie Skłodowska-Curie grant agreement No 721256.

I would like to thank my supervisors Prof. Giovanni Belingardi and Prof. Davide Salvatore Paolino for their continuous guidance and crucial comments during the life of this project. Furthermore, I would like to thank my past colleagues in Centro Ricerche Fiat Vito Lambertini, Lucio Cascone and Ranieri Lupicino who hosted me for the past three years and helped me to pursue my research activities as smooth as possible.

I would like to appreciate as well my colleagues in Politecnico di Torino, Dr. Raffaele Ciardiello who help me extensively with performing characterization tests, Ravin Garg and Lorenzo Vigna who helped me in the design of the anti-buckling fixture and performing impact tests. Last but not least, I should thank Dr. Andrea Calzolari and Dr. Giuseppe Galizia from Instron ITW for their help in the manufacturing and preliminary investigation steps of the fixture developments.

Abstract

Since 1980s scientists have demonstrated that fiber reinforced polymer composites exhibit high specific energy absorption capabilities. However, lack of understanding of their energy absorbing mechanisms under different conditions has hindered full potential applications of composite structural components. Testing the final structures under various scenarios is complex, expensive, and time consuming. Therefore, it is necessary to have a methodology for assessing energy absorption capacities in element levels. With the help of the building block approach, a testing methodology has been developed to solve this problem.

For the element level experiments, saw-tooth triggered flat rectangular specimens with dimensions of 150×100 *mm* have been used. A new fixture has been designed and manufactured to support this flat specimens under impact and initiate stable failure by preventing global buckling. Four cylindrical anti-buckling columns with adjustable heights have been adopted to support the specimens from two opposite sides. Cylindrical columns to avoid tearing of the elements, gap in the bottom to avoid jamming, up to 50 *mm* of crushable lengths, and the possibility of capturing the fracture mechanisms with high speed camera from the lateral side are some of the advantages of this fixture compared to the previously developed ones.

Using this fixture, effects of unsupported height, impact velocity, and impact mass on the crashworthiness evaluations have been studied. The promising reproducible results have proven the reliability of the fixture. These results have been used for the optimization of the numerical simulations performed in a companion PhD work. Moving upward in the building block, quasi-static and dynamic crush tests have been performed on Formula SAE crash boxes made of carbon fiber/epoxy composite. These results have proven the validity of the proposed approach.

Contents

List of Figures

List of Tables

Nomenclature

Roman Symbols

δ	crush displacement
$\dot{\varepsilon}$	Strain rate
ε	Strain
ε_l	Longitudinal strain
ε_t	Transverse strain
ν	Poisson's ratio
ρ	Material density
σ	Stress
τ_{12i}	Shear stress at i^{th} data point
A	Cross sectional area
b	Width
B_y	Bending percentage of the coupon udder compression
CFE	Crush force efficiency
D	Diameter
D	Maximum deflection of the center of the beam
d	Depth

E^{chord} Tensile chord modulus of elasticity

F Force

G_{IC} Interlaminar toughness

L Support span

LU Load uniformity index

m Material strain rate sensitivity

P Load

PAS Polyarylsulfone

$PEEK$ Polyetheretherketone

PEI Polyetherimide

PI Polyimide

$PMMA$ Polymethylmethacrylate

PP Polypropylene

S Width

SCS Sustained crush stress

SEA Specific Energy Absorption

SEM Scanning electron microscopy

$SSCS$ Specific sustained crush stress

t Thickness

T_g Glass transition temperature

UD Unidirectional

W Total energy absorbed during the experiment

CFC Channel Frequency Class

CFRP Carbon fiber reinforced plastic

FE Finite elements

FEA Finite element analyses

GFRP Glass fiber reinforced plastic

ICONIC ITN improving the crashworthiness of composite transportation structures Innovative Training Network

NCF Non Crimp Fabric

Chapter 1

Introduction

The adjective *crashworthy* was coined in 1942 by John Lane, director of the aviation medicine in Australia, to describe a structure able to protect its occupants in survivable crashes [6]. Derived from this term, "crashworthiness" became a characteristic of different materials and structural designs, measuring their ability in achieving this goal. It was mainly used in aerospace industry in the beginning and gradually found its importance in the automotive sector when efforts took place to reduce the number of severe injuries and fatalities in car accidents.

Unlike active safety system which is responsible to avoid having accidents, passive safety aims to minimize the damages and save lives when incidents happen. Crashworthiness is a part of passive safety system and stands for the ability of the vehicle to deform in a way that sustainable deceleration loads are transferred to the occupants and still maintain a sufficient survival space for them. Figure 1.1 shows the aluminum crash boxes of Alfa Romeo 4C which absorb crash energy by undergoing extensive plastic deformations.

Aluminum structures have been widely used for decades to absorb energies during crashes and its behavior and responses are well understood. Carbon Fiber Reinforced Plastics (CFRPs) have shown interesting features such as lower density, good tensile strength, high strength to weight ratio, and high corrosion and fatigue resistance. Nonetheless, lack of understanding of their energy absorption mechanisms and crash behaviors under various circumstances have hindered complete exploitation of their

Fig. 1.1 Alfa Romeo 4C monocoque made of carbon fiber composites [1]

potentials. That is the main reason behind using aluminum crash box in cars even if the monocoque is made of CFRP, Figure 1.1.

The prime purpose of this research study was to gain comprehensive understanding of CFRPs energy absorption mechanisms through various experimental tests. This goal was pursued alongside other research activities inside the EU Horizon 2020 Marie Skłodowska-Curie Actions Innovative Training Network ICONIC[2] which stands for improving the crashworthiness of composite transportation structures. The aim of the program was to develop the next generation of lightweight transportation structures with superior crashworthiness. Fifteen PhD students from nine different beneficiaries in six EU countries were working towards this goal. Aligned with numerical and analytical simulations of other PhD students, the experiments performed in this research study served as the proof of concept for virtual testing of composite structures.

The main methodology to achieve these objectives was the building block approach. This approach has proven its functionality and efficiency in decreasing the number of complex tests and increasing the reliability of the numerical analysis. It has been applied in commercial projects like Boeing 777 and suggested by the

[1] http://driving.ca/alfa-romeo/reviews/road-test/first-drive-2015-alfa-romeo-4c-spider
[2] https://blog.qub.ac.uk/wordpress/iconic/

authors of Composite Materials Handbook [7]. Figure 1.2 schematically illustrates this approach.

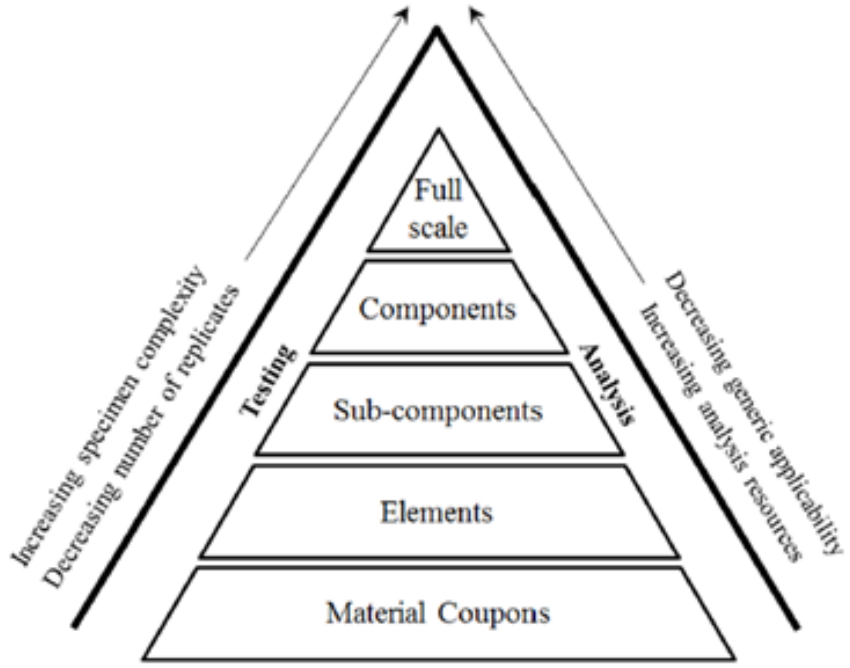

Fig. 1.2 The building block approach for combining analytical and experimental evaluation of composite structures [7].

For the base level tests, ASTM standard characterization tests were carried out. Theses results were used for materials screenings and selection purposes and also provided the necessary input data for the simulation. Then, for the element level experiments, a new anti-buckling fixture was developed and manufactured which helped design value developments and tuning of the simulation analysis at the meantime. Finally, impact tests with elevated energies and velocities were performed on the composite structures under drop tower to provide the essential data for the virtual analysis verification.

In the next chapters, first an overview of the crashworthiness of composite materials and detailed review of the previously developed anti-buckling fixtures are provided. Then, materials and methodologies used in this study are described. The simulation steps towards the manufacturing of the newly developed anti-buckling fixture are demonstrated. After that, results and discussions obtained from this fixture and other experiments are thoroughly analyzed. Finally, the main results and

achievements are concluded and an introduction to the future research possibilities derived from this work is provided.

Chapter 2

Literature Review

In this chapter, first an introductory description about energy absorption of materials and different calculation methods is provided. Then, focusing on polymer matrix composite materials, various parameters affecting the final values of absorbed energy are discussed. Finally, a chronological review of the previous attempts to standardize a method for crashworthiness characterization is reported.

2.1 Energy Absorption

Figure 2.1 compares the results of dynamic collapse tests on composite and metallic specimens. Figure 2.1a illustrates an example of typical raw and filtered force-displacement results for a composite specimen undergoing progressive failure under crushing experiment [8]. Two important aspects of these curves are maximum force and mean crush force. Figure 2.1b shows the response of nanostructured ultrafine-grained multi-phase (UFG-MP) and dual-phase (DP) steels under dynamic tests [9]. The wavy pattern of drop and increase in the force data for metallic specimens, in comparison to the fluctuation of the force data around mean force after reaching the peak, proves the existence of different failure mechanisms between metallic and composite structures.

Beside these differences, similar approaches exist to quantify the energy absorption capabilities of materials. One way of evaluation is to calculate the crush force efficiency (CFE), using the Equation 2.1. CFE values close to one are desirable and they mean that after reaching the elastic load limits, material continues to sustain

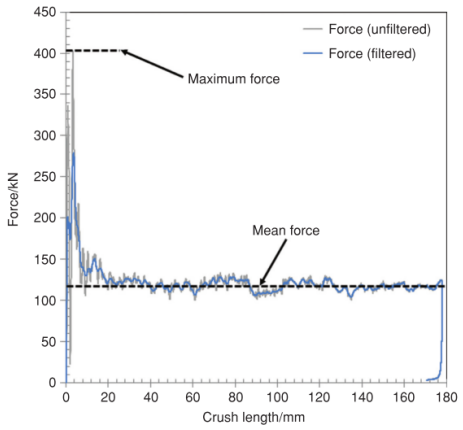

(a) Example for a typical force/displacement result of composite specimens [8]

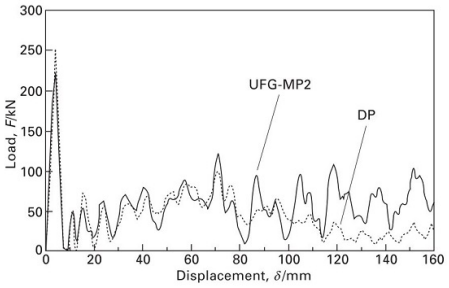

(b) Nanostructured steel columns under dynamic collapse tests [9]

Fig. 2.1 Examples of the load-displacement curves for composite and nanostructured steel columns under crush tests.

those loads while being crushed. Here is the formula to calculate CFE:

$$CFE = \frac{F_{Mean}}{F_{Peak}} = \frac{1}{LU} \tag{2.1}$$

where F_{Mean} is the mean force after reaching the maximum value, F_{Peak}, and LU is the load uniformity index which is the inverse of CFE [8].

Similar to CFE, the sustained crush stress (SCS) is another way to assess the crashworthiness of the materials. It is less commonly used compared to other methods but still could be interesting for structural design purposes. Equation 2.2 shows the formula for SCS:

$$SCS = \frac{F_{Mean}}{A} \tag{2.2}$$

where A is the cross sectional area of the specimen [8].

Another approach for crashworthiness quantification is to calculate the Specific Energy Absorption (SEA) that is the energy absorbed per unit mass of the material [10] and is calculated using the formula below:

$$SEA = \frac{W}{\rho A \delta} = \frac{\int_0^\delta F d\delta}{\rho A \delta} = SSCS \tag{2.3}$$

where W is the total energy absorbed during the experiment, ρ is the material density, δ is the crush displacement, and F is the crush force. In some older publications

SEA is referred to as Specific Sustained Crush Stress (SSCS) as well [8]. SEA is not an intrinsic property of the material and depends extensively on the design factors and testing conditions which could enable different failure mechanisms to occur [11–13]. This could be both "a blessing and a hinderance" for the designer, as stated by Farley and Jones [14].

2.2 Failure Mechanisms

Different failure mechanisms result in different energy absorption capabilities, even for the same material. For composites, compared to the well studied and understood metals, these mechanisms are not fully comprehended. Figure 2.2a shows an aluminum cylinder after the crush test [15]. The specimen has mainly absorbed the energy by undergoing drastic plastic deformations and progressive folding.

On the other hand, Figure 2.2b shows an identical cylinder but made of carbon fiber reinforced polymers (CFRPs) undergoing the same test. Since the brittle nature of CFRP does not allow the plastic deformation, it has to absorb the energy by undergoing other mechanisms such as rupture, splaying, fragmentation, and etc. [15].

(a) Metallic specimen (b) CFRP specimen

Fig. 2.2 Schematic drawings and real pictures of two different specimens after crush tests demonstrating differences in their energy absorption mechanisms [15].

Generally, failures of composite materials can be stable and progressive, or unstable and catastrophic. Stable failure means that after reaching the maximum force and crush initiation, the specimen still manages to sustain quite high compression loads. However, in unstable failure, loads drop to near zero values after crushing is initiated. Figure 2.3 shows load displacement curves for these two cases of failure

[16]. Stable failure allows the material to continue absorbing higher portions of energy by further displacements of the crushing front. Therefore, it is highly desired and researchers have tried for decades to find the perfect conditions to initiate and maintain stable failures in the composite components.

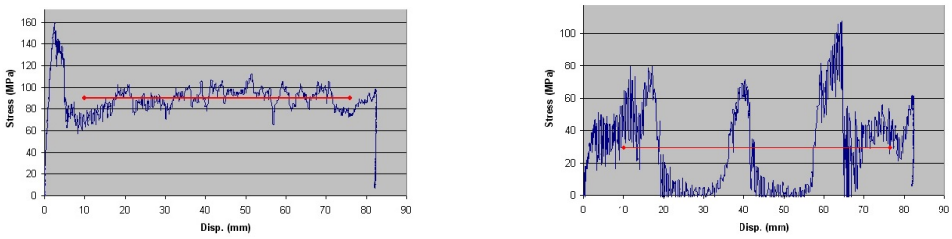

(a) Stable failure (b) Unstable failure

Fig. 2.3 Examples of the stress-displacement results obtained from stable (a), and unstable (b) failures of composite plates made of different materials. The red lines indicate the mean force in each test after the crush initiation [16].

Some of the reasons for unfavorable unstable failure modes are buckling of the specimen, interpenetration in the middle of the specimen that itself might be due to the buckling, and/or barreling of the outermost composite layers [13]. Schematic drawings of these unstable modes are shown in Figure 2.4.

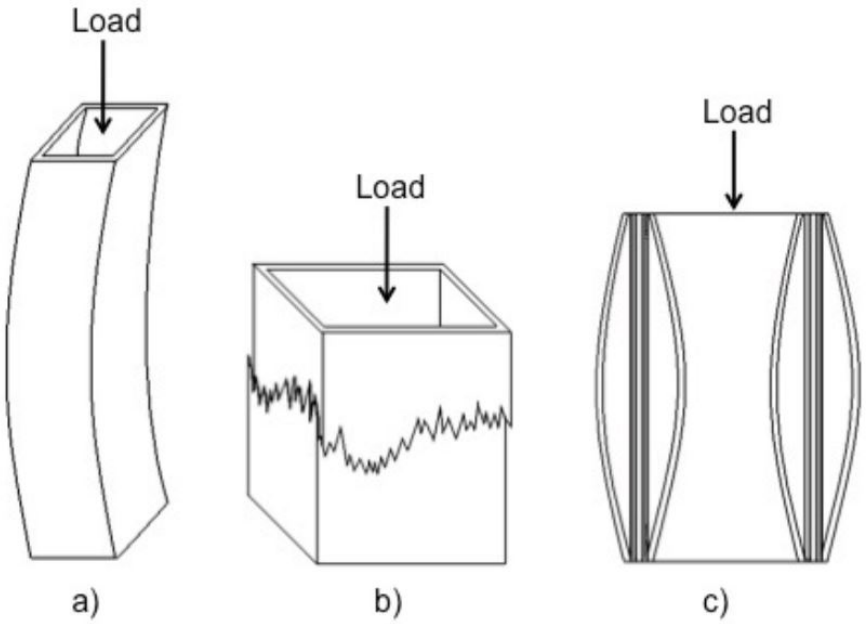

Fig. 2.4 Different modes of unstable failure: (a) buckling, (b) interpenetration, and (c) barreling. [17]

Since late 1980s, researchers have tried to understand and classify different stable failure modes in progressive crushing of composites. Figure 2.5 shows different modes of failure for fiber reinforced polymer composites with layup structure [17]. Farley and Jones, among the pioneers to objectify the progressive crushing modes, classified four different modes for composite tubes:

1. Transverse shearing
2. Brittle fracturing
3. Lamina bending
4. Local buckling

The first three modes happen during the progressive crushing of the composite structures. However, the writers warned about the overgeneralizing of the results given that various parameters influence the final crush response of the specimen [14].

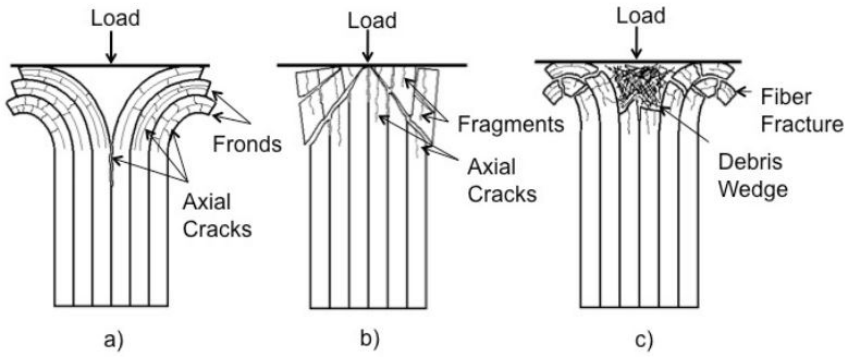

Fig. 2.5 Different crush failure modes: (a) fiber splaying, (b) fragmentation, and (c) brittle fracture [17].

Less than a year after them, Hull declared his classification of the progressive crushing modes in brittle fiber reinforced composite tubes. He identified two general modes of splaying and fragmentation which depend on the geometrical, microstructural, and testing parameters. He noticed a serration in force displacement results inside progressive crushing zones of brittle specimens, Figure 2.6, and related that to the sequences of "stick-slip form of propagation." Hull concluded that these modes are related to the primary micro-mechanisms of fracture in the composites. He added that by changing the layup structure of the layers it would be possible to change the micro-mechanisms of crush and control the transition between splaying and fragmentation modes [13].

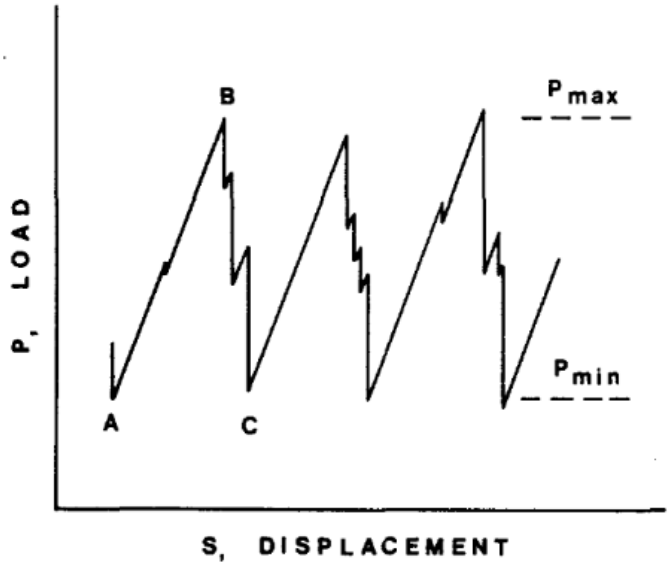

Fig. 2.6 Schematic of force displacement curve of progressive crushing. Hull associated the load relaxations with rapid crack growth in the crush zone [13].

In 1998, Carruthers et al. conducted an extensive literature review of the research works performed on the crashworthiness of composite structures. They concluded that among the authors who have worked on the failure mechanisms of composites, Hull and Farley have "provided the most comprehensive treatments." They went even further and claimed that both Hull and Farley have categorized the same mechanisms but named them differently. Splaying is the same as lamina bending and occurs when cracks are parallel to fibers. Fragmentation is the same as transverse shearing and happens when short cracks form partial lamina bundles [18].

Reviewing the experimental works on progressive crushing mechanisms in composites, reveals two common trends in the classifications of failure modes. First trend classifies macrofailure modes, like Bisagni's four collapse modes as tearing, socking, splaying, and microfragmentation modes [19]. Second one categorizes microfailure modes such as fiber breakage, matrix cracking, and delamination [19], or fiber debonding, transverse shearing, and matrix fragmentation [20]. The analysis of the collapse modes pictures and microfailure mechanisms, indicates that they are just combination of the two extreme cases explained earlier by Farley and Hull [21].

2.3 Different Parameters Affecting Crashworthiness

From the very beginning of the experimental crashworthiness evaluation of the composite structures, researchers found out that there are too many parameters affecting the obtained results. Extensive studies have been performed since then, trying to understand the way each parameter affects the energy absorption capacities of the whole specimen. In the next pages a brief review over some of these parameters is provided.

2.3.1 Constituents

Since the early years of 1980s, researchers figured out that different materials show different failure mechanisms and SEA. Those very first studies were performed mainly on thermosetting matrix, often epoxy, reinforced with graphite, glass, Aramid, or carbon fibers. Some of these studies were performed by Thornton and Edwards [22], by Farley [14, 12, 23], and by Hull [13].

Their main objectives were to understand and categorize different failure mechanisms and reached similar conclusions that more brittle fibers, like glass and graphite, crush in fiber splitting and delamination modes while more ductile fibers, like Kevlar, crush in buckling mode. In all these studies, matrix material was epoxy which is a thermosetting polymer. The lower manufacturing costs and faster processing time of thermoplastic polymers alongside their recyclability and interesting chemical and mechanical properties, have made them attractive alternatives for thermosetting matrices [24].

In 1992, Hamada et al. compared the energy absorption of unidirectional (UD) carbon fiber/epoxy composite tubes with UD carbon fiber/polyetheretherketone (PEEK) ones. They reported SEA of 180 kJ/kg for 0° carbon fibre/PEEK samples which was much higher than the 53 kJ/kg for $\pm 45^\circ$ carbon fibre/epoxy specimens. They argued the superior SEA value was related to the higher interlaminar toughness (G_{IC}) of PEEK matrix composites [25].

They continued their research by examining differed thermoplastic matrices like polyetherimide (PEI), polyimide (PI), and polyarylsulfone (PAS) with altering fiber orientations [1]. Also in that study, carbon fiber/PEEK specimens showed the superior SEA capabilities. This was again related to the larger number of frond

splitting and fiber fracture in the crushing zone and the higher G_{IC} values for PEEK matrix composites.

After proving experimentally that PEEK matrix composites have exceeding energy absorption capabilities, the effects of fiber materials on the crashworthiness of these composites were evaluated [26]. It was shown that carbon fiber specimens have about 20% higher SEA values. The authors suggested that it might be partially due to the lower masses of CFRP specimens, since SEA is energy absorbed divided by mass.

Jacob et al. concluded that matrix material can change the fracture mechanisms if the fibers are brittle. However, in the case of ductile fibers the change in matrix material does not have any significant impact on the final results [10].

Boria et al. studied the energy absorption of fully thermoplastic composites, where both fibers and matrix are thermoplastic polypropylene (PP). Several specimens with different diameters and thicknesses were manufactured and crushed for SEA calculations. The crush response of the specimens was a sequence of localized plastic hinges, similar to the metallic ones. The writers reported these specimens to be "3/4 times lower in energy absorption capacity" compared to common thermoset composites. However, because of their full recyclability and rapid process time, still could be an interesting counterparts for thermoset composites [27].

2.3.2 Design and Geometry

From the first experimental studies, scientists noticed that changing fiber directions affects the absorbed energy [14, 13, 25, 26]. However, they observed that the influence of fibers direction is not the same in all materials.

Generally, if the specimen is breaking due to bending or local buckling, having some fibers off the axial axis of the crush increases the energy absorption. The reason is the lateral support from these off axis fibers. Ramakrishna et al. experimentally studied four different thermoplastic matrices with carbon fibers from $\pm 0^\circ$ up to $\pm 30^\circ$ with respect to the axis of the tube. In all cases they reported an initial increase of the SEA [1].

On the contrary, if the main failure mode is brittle fracture of the composite, like most carbon fiber epoxy composites, these off axis fibers decrease the axial

stiffness and hence the energy absorption characteristics of the specimen [10]. Table 2.1 reports the results of fiber orientations affecting SEA of carbon fiber/PEEK composite tubes [1].

Table 2.1 Specific energy absorption of carbon fiber/PEEK composite at different fiber orientations [1]

Fiber Orientation	SEA (kJ/kg)
0°	194.1
$\pm 5^\circ$	205.3
$\pm 10^\circ$	225.3
$\pm 15^\circ$	226.8
$\pm 20^\circ$	202.3
$\pm 25^\circ$	181.1

Stacking sequence also plays a similar role like fiber direction. It can be explained through classical laminate theory since various sequences have different extensional, coupling, and bending stiffness. Because the combination of fiber orientation and stacking sequence is countless, manufacturing different specimens and comparing them experimentally would be time consuming. More sophisticated approach could be using numerical analysis to compare different designs and geometries and validate the obtained results through experiments. For instance, Jiang et al. numerically studied the stacking sequence effect of fabric and UD fibers on energy absorption of carbon fiber/epoxy sinusoidal plates [28].

Similarly, same materials with different structural geometries illustrate diverse SEA values. This effect was also known for more than 39 years, since Thornton and Edwards studied energy absorption in cylindrical, square and rectangular composite tubes with a wide range of thickness over diameter (t/D) or width (t/S) ratios in 1982. They indicated more stable failure modes in cylindrical tubes rather than those with planar walls for a given stacking sequence [22]. The main reason was reported to be stress concentration in the corners and therefore splitting of square and rectangular tubes.

Other early researchers in this field studied further the effect of t/D ratios on progressive stable crushing of composite structures and declared that it undeniably affected energy absorption capacity of composites [23, 29]. They reported an increment in SEA when the ratio increased up to a critical value. The initial increase was related to the higher interlaminar cracking and more frond splitting and fibers

fracturing but after the critical value the fracture mechanism was changed to splaying mode [10].

Mahdi et al. [30] experimentally examined elliptical specimens aiming to understand the relationship between ellipticity ratio and specific energy absorption. The tubes were made of woven roving glass fibers with $[0/90]$ orientations. Some of them were filled with a foam consisting of chopped oil palm fibres/resin mixture and the others had hollow geometries. The ellipticity ratio varied from 1.00, circular, to 2.00. Even though no linear relation between this ratio and energy absorption capability was observed, highest crushing stress and normalized SEA values were reported for specimens with ellipticity ratio of 2.00 in both hollow and filled samples [30].

Wang et al. studied both fiber direction and wall thickness effects of carbon fiber/epoxy composite tubes used for crashworthy subfloor structures. Similarly, they reported decrease in SEA with increasing carbon fibers angles with respect to the tube axis. For the thickness effect, they witnessed an initial increase followed by a decrease in SEA while increasing the thickness of specimens [31].

Haolei et al. studied stacking sequence and geometry effects on the failure and energy absorption of circular, square, and sinusoidal composite specimens [32]. They reported the possibility of changing failure modes in thin-walled composite structures from low energy absorbing local buckling, $[\pm 45]_{3s}$, to medium energy absorbing lamina bending, $[0/90]_{3s}$, and high energy absorbing transverse shearing failure mode, $[\pm 45/0/0/90/0]_{3s}$. Also, regarding the geometrical aspects, they observed the highest SEA in cylindrical tubes [32].

2.3.3 Trigger

Beside constituents and design factors affecting crashworthiness of composites, also triggering mechanisms play crucial roles in the final results. Thornton in 1979 explicitly stated that composites have higher energy absorption capabilities than metals, "provided that the correct trigger mechanism was used to initiate the failure" [11]. In this section different triggers and their efficiencies are discussed.

Composites absorb desirable amount of energy only if progressive crushing is initiated and catastrophic failure is avoided. After having the right constituents with the correct design and geometry, triggers help to concentrate the applied forces in

the proper sections with reduced initial load peak and initiate progressive failure from those locations in the composite components like flat plates, tubes, crash boxes, etc. [10]. They can be intrinsic like ply drop offs, chamfer, notch, saw-tooth, etc. or extrinsic like plugs or external cavity triggers. Figure 2.7 schematically shows some of these trigger systems [33].

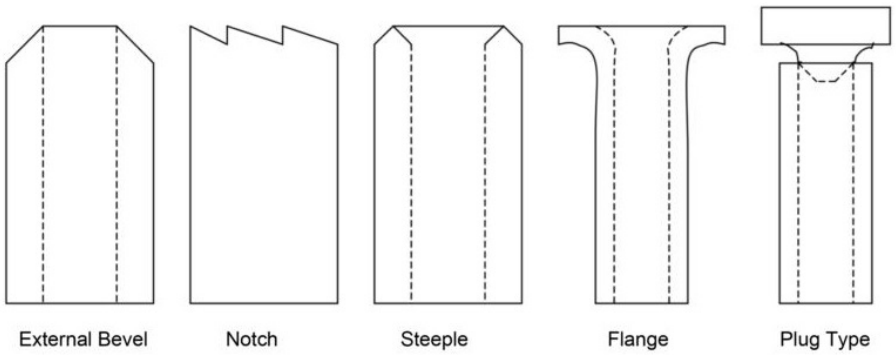

Fig. 2.7 Different trigger mechanisms. [33]

Cauchi Savona and Hogg chose 45° steeple chamfer triggers to crush flat glass fiber reinforced composite plates which were held in their place using knife-edged supports [34]. Meanwhile, Ueda et al. machined a symmetrical V-shaped triggers at one end of the unidirectional CRFP plates and achieved stable progressive crushing with delamination and splaying of the outer layers and fragmentation of the inner ones [35].

Ma et al. quasi-statically crushed flat carbon fibre reinforced polyamide 6 composites coupons triggered with single and double bevel triggers at various angles. They observed that only triggers with 40° to 60° angles succeeded in initiating progressive crushing while steeper triggers caused global and local buckling [36]. Similar research was done by Guillon et al. on carbon epoxy laminated plates with three different triggers, 45° chamfer, 140° steeple, and external triangular trigger on the base plate. They as well showed a great variation in the calculated values based on the trigger mechanism [37].

Lombarkia et al. compared the effects of steeple and 45° chamfer triggers on the hat shaped carbon fiber reinforced epoxy open section and reported higher energy absorption for 45° chamfer triggers. They reasoned it was due to the delayed response in reaching the peak crushing force and more splaying mode which itself

was because of more intense propagation of the delamination in the case of steeple trigger [38].

Tong and Xu assessed energy absorption of the 2D braided CFRP tubes with two external crush-cap triggers, traditional chamfer-flat trigger and their innovative semi-circle cavity. Their experimental and numerical investigations showed similar peak loads for two caps but the sustained crush loads, and therefore SEA values, were higher for semi-circle cavity caps. This could be a result of restricted space that forces greater amounts of longitudinal cracking to occur which does not happen when using chamfer-flat plugs [39].

All the intrinsic triggers mentioned in the previous paragraphs were cut in the composite specimens through some machine working. Another approach could be gradual ply drop off during the manufacturing phase. For instance, Belingardi et al. tested formula SAE front impact attenuators and achieved "almost" constant force-displacement results with decelerations under 20g, satisfying the safety requirements, with smooth reduction of the thickness as a trigger mechanism [40]. In the literature, it is not completely agreed on which trigger mechanism delivers the bests results and each research group goes with their desired trigger system [21].

2.3.4 Strain Rate

Another important aspect which was noticed by researchers since the beginning, was the variation between quasi-static and dynamic results of impact experiments performed on specimens with the same materials, geometries, and triggering systems [13, 12, 41]. However, it is not reported unilaterally a specific relation between speed of the experiment and absorbed energy. Some reported an increase in the SEA with higher test speeds [42, 43], some announced no effects [11, 44], and some others declared and inverse relation [45, 46].

Mamalis et al. studied the effects of constituent materials and the structural geometry on the crashworthiness of thin-walled fiber reinforced circular tubes. They categorized three modes of fracturing as delamination mode, brittle fracture, and mixed mode. They concluded that the test speed has a negative impact on the crashworthiness in delamination and positive effect in the two other modes. They claimed high frictional resistance, due to the debris penetration in the composite material, being the main reason of higher crashworthiness. Since in delamination

mode there is not much debris, compared to brittle fracture, increasing speed has a negative effect on energy absorption capabilities [46].

To better understand the effects of testing speed, it is fundamental to understand how the constituents response to the change in strain rate. Figure 2.8 represents how materials with different sensitivities to strain rates react. In some of them the yield stress increases with strain rate, in some decreases, and in the others remains unaffected.

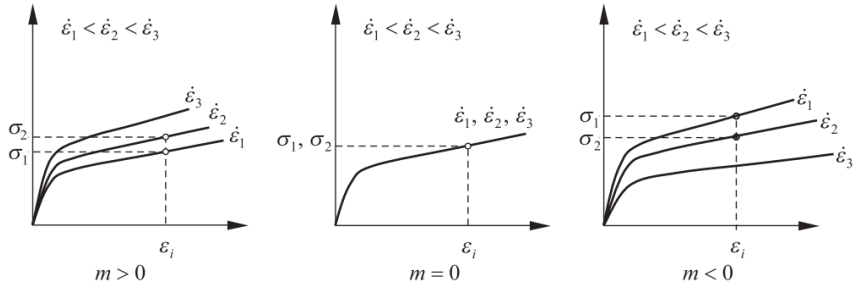

Fig. 2.8 Various relations between stress and strain based on differences in strain rate sensitivity [47].

Equation 2.4 from Hosford's book on mechanical behavior of materials [48] shows the relation between strain rate's effect on flow stress at constant temperature and strain rate:

$$\sigma = C \cdot \dot{\varepsilon}^m \tag{2.4}$$

where σ is the flow stress, $\dot{\varepsilon}$ is the strain rate, and m is the material strain rate sensitivity [48]. To calculate m, stress strain response of the material for two different strain rates are measured and Equation 2.5 in a given strain, like in Figure 2.8, is used. The formula is given below:

$$\frac{\sigma_2}{\sigma_1} = \left(\frac{\dot{\varepsilon}_2}{\dot{\varepsilon}_1}\right)^m \tag{2.5}$$

At room temperature many engineering metallic materials have strain rate sensitivities between - 0.005 and 0.015 values [48]. Walley and Field studied compressive strain rate sensitivity of 17 polymers and figured a positive strain rate sensitivity, mostly linear, for strain rates up to $10^3 s^{-1}$ [49]. Li and Lambros studied polymethylmethacrylate (PMMA) response in various strain rates and found out that the material characteristics changes from a ductile material to a brittle one with increasing the

compressive strain rate [50]. Both studies were performed at room temperature, while researchers were concerned about the adiabatic heating under very high speed loading conditions which might cause thermal softening [49–51].

Mulliken and Boyce developed an analytical method for strain rate dependency of amorphous polycarbonate and PMMA by taking into consideration the secondary molecular motions, β, and viscoelastic data from experiments [52]. Here as well, isothermal nature of the model was unable to predict the post yield response in moderate strain rates for PMMA. Rittel paid deeper attention to the thermomechanical analysis of polycarbonate and managed to measure the conversion rates of mechanical energy into thermal energy which could help analytical solutions for strain hardening and thermal softening predictions [53].

Epoxy was also studied by many researchers at different strain rates, typically using hydraulic testing machines for low to moderate rates and split Hopkinson bar technique [54] for higher rates. Gilat et al. discovered increase in tensile and shear modulus by increasing strain rate. They reported around 100% higher shear strength when strain rate was changed from $10^{-4}\ s^{-1}$ to $700\ s^{-1}$ [55]. Similar results of yield stress growth from 85 MPa at $0.001\ s^{-1}$ to 220 MPa at $12000\ s^{-1}$ strain rates were reported by Tamrakar et al. [56].

Almost identical results about strain rate effect on epoxy resin were reported by other researchers as well. For example Iwamoto et al. studied bulk materials made of epoxy resin structural adhesive [57] or Gómez-del Río and Rodríguez synthesized and evaluated thermosetting epoxy polymer system [58] and both studies claimed higher stiffness and maximum stress by increasing the strain rate. Tay et al. [59] performed an empirical analysis on pure epoxies and also glass fiber reinforced ones and reported increase of mechanical properties, Young's modulus and maximum stress, for both specimens.

In 1991, Farley [60] analyzed chamfered circular tubes of graphite and Kevlar reinforced epoxies with six different ply orientations under crushing speeds of $0.01\ m/s$ and $12\ m/s$. He concluded that crushing speed affects the measured SEA only if the crushing mechanism is a function of strain rate. For instance, $[0/\pm\Theta]_2$ graphite epoxies did not show any change in SEA while $[\pm\Theta]_3$ exhibited 35% increase [60].

Okoli examined woven glass/epoxy laminate in the limited range of $10^{-4}\ s^{-1}$ up to $.3\ s^{-1}$ strain rates and showed increase in tensile, shear, and flexural energy

absorption of the specimens by increasing the strain rate [61]. He performed SEM analysis of the fractured surfaces and stated that brittle fiber failure and fiber pull-out under quasi-static conditions was changed to matrix damage and this was the reason for enhancement in the absorbed energy.

However, the detailed review paper by Jacob et al. in 2004 did not prove a unique dependency of composite mechanical properties on the strain rate. They reported 8 rate insensitive cases and two cases of decreasing mechanical properties out of 39 reviewed references [62]. This makes it clear that in each material system the response will be different and should be studied.

Gilat et al. studied strain rates effects on carbon fiber reinforced epoxies with different fiber alignments [63]. They observed higher stiffness in all cases with increasing strain rate but only in $[\pm 45^{\circ}]$s specimens max stress was increased considerably. They concluded that composite materials behavior is driven by the resin sensitivity to strain rate [55].

Zhang et al. also drew a similar conclusion about the orientation of carbon laminates and claimed that viscoelasticity of epoxy matrix and interface strength play an important role when studying epoxy matrix composite mechanical behaviors under different strain rates [64]. By performing SEM analysis, they have showed that at the interface between carbon fibers and epoxy resin, the brittle fracture becomes ductile by increasing the strain rate which enhances interfacial strength [64].

2.3.5 Temperature

As it was mentioned by some of the articles in the previous section, elevated temperatures due to thermal conversion of kinematic energy caused thermal softening in some experiments. An important temperature in polymer materials is the glass transition temperature (T_g) above which the mechanical properties change dramatically. Tamrakar et al. studied compressive response of pure epoxy specimens with T_g range $70-100\ ^{\circ}C$ in various temperature and reported no definite yield point ($d\sigma/d\varepsilon = 0$) and rubbery behavior above $100\ ^{\circ}C$, Figure 2.9 [56].

Joostsen et al. examined crashworthiness of carbon fiber epoxy open sections with hat geometries and steeple triggers at $-35\ ^{\circ}C$, $23\ ^{\circ}C$, and $70\ ^{\circ}C$ [65]. They reported a lower steady state crush loads, and hence lower energy absorption, for specimens at either low or elevated temperatures compared to the ones at room

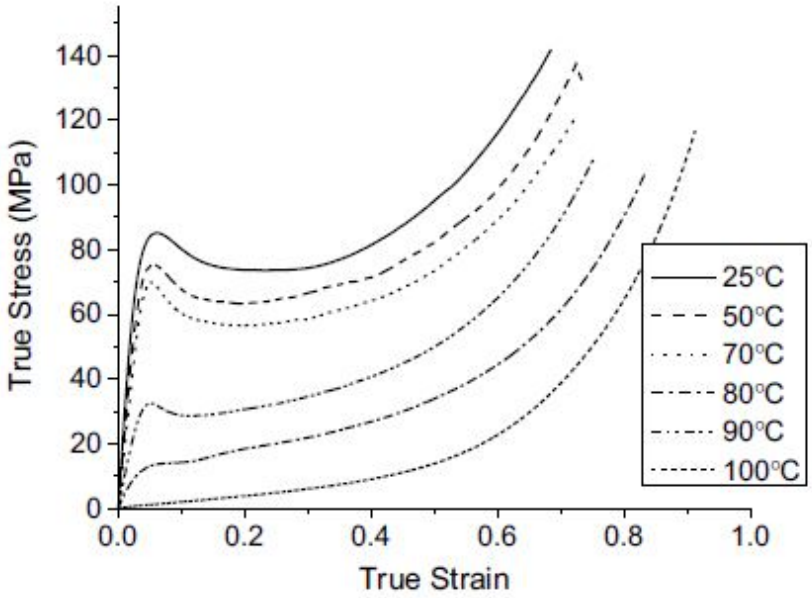

Fig. 2.9 True stress true strain response of the pure epoxy with T_g range $70-100\ ^{\circ}C$ under compression in different temperatures [56].

temperature. They noticed brittle fracture mode for lower temperatures and splaying and delamination for higher temperatures. The delamination crack length and curvature of the fronds increased by increasing the temperature. Their findings are inline with the previously reported articles, Figure 2.10, and emphasizes that environmental conditions must be taken into account during the characterization of the composite elements [65].

Jia et al. experimentally studied temperature effects on the mechanical properties of CFRPs and reported a linear decrease of the strength and toughness of the composite by increasing temperature [66]. By performing both static and dynamic three point bending tests, they also observed a change in fracture mechanisms from microbuckling to tensile breakage in elevated temperatures and related these results to the brittle nature of the polymer matrix in lower temperatures.

Similar results, change in the fracture mechanism and decrease of the mechanical properties, were observed by Liu et al. in composite sandwich panels with pyramidal truss cores [67], by Panaitescu et al. studying enviromental effects on glass-fiber reinforced polyurethane [68], and by Thornton assessing crashworthiness of various graphite, Kevlar, and glass fiber reinforced composites [11].

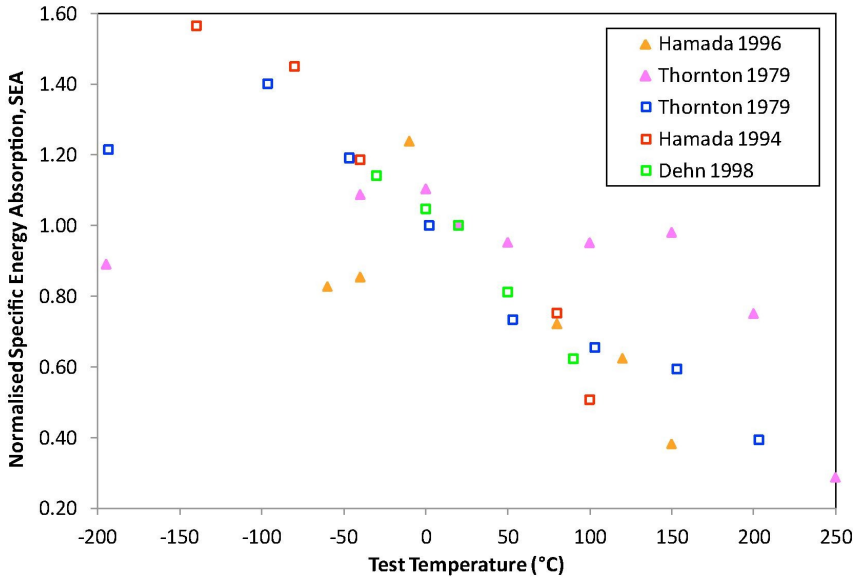

Fig. 2.10 True stress true strain response of the pure epoxy under compression in different temperatures [65].

2.4 Energy Absorption Characterization Techniques

The absence of standardized characterization method for evaluating energy absorption capabilities of composite materials, has forced each research group to choose a technique which better fits their requirements. Some use tiny flat coupons, some crush rectangular plate elements, and others test self-supporting specimens, either open or closed sections. In this section, first a brief review over the application of coupons and self-supporting specimens for SEA calculations is provided. Then, in the following subsection, a detailed literature review is performed over anti-buckling fixtures for crushing flat composite elements.

Gutkin and Pinho used small unidirectional flat coupons with wedge trigger under quasi-static conditions to understand the effect of contact and friction at microcrack on the accuracy of their FE models [69]. With only 4 mm of the crushing length and simple geometries, the writers aimed to eliminate the uncertainties of loading conditions and geometrical features.

Bru et al. proposed a similar testing method consisting of a flat specimen mostly clamped along its length with a novel triangular through-thickness trigger [70]. Figure 2.11 illustrates the test method and triggering system. Their main goal was to evaluate the crushing behaviour of unidirectional laminates with dominating in-

plane failure mode or fragmentation crushing. This was achieved due to their new triggering method that reduced out-of-plane splaying by conventional bevel triggers. Also here the crushing displacement was short and only 5 mm.

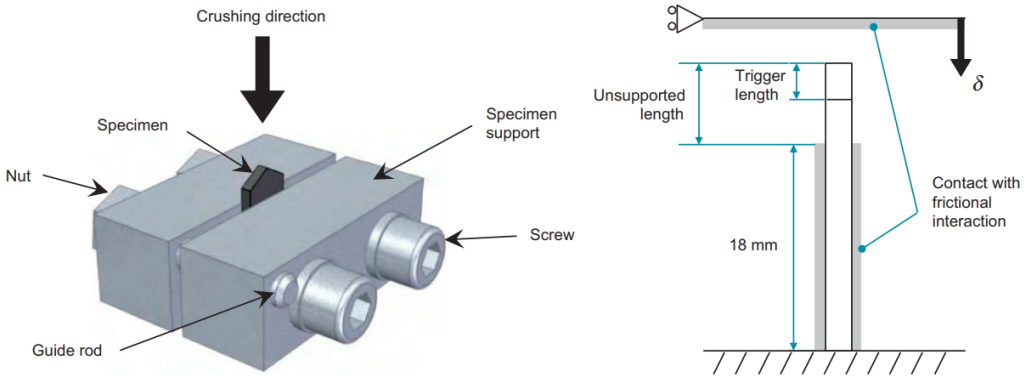

Fig. 2.11 Test method proposed by Bru et al. evaluating the crushing behaviour of unidirectional laminates with triangular through-thickness trigger [70].

Dalli et al. have also used similar methodology to characterize the failure mechanisms and stresses in the coupon level and used it for the elaboration of their modelling techniques [71]. Crushing distance was higher than previous studies, up to 20 mm, and they have performed dynamic tests as well. But even this crushing length is considered short comparing with tests on self supporting specimens and flat plates. However, these simple testing studies assisted researchers to quantify the crushing stress and helped them to elaborate and validate predictive models developed inside their research groups [69–73].

Short crushing distances and small testing specimens might be good for understanding the crush initiations and effects of various internal and external forces, but they cannot perfectly represent the progressive crushing phenomenon happening in composite structures. To overcome this issue, researchers have been testing on self-supporting specimens or flat plates constrained with anti-buckling fixtures. Figure 2.12 shows some images of these specimens.

2.4.1 Anti-buckling Fixtures

Various types of self supporting specimens, tubes, omega (Ω) shaped, sinusoidal, etc. were introduced and studied by researchers. On the other hand, to avoid the manufacturing complexities related to these specimens and move toward standardized,

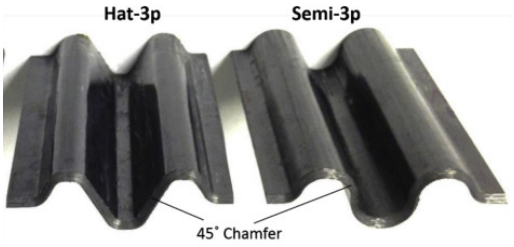

(a) corrugated trapezoidal, or 'hat' cross section and semi-circular cross section [74]

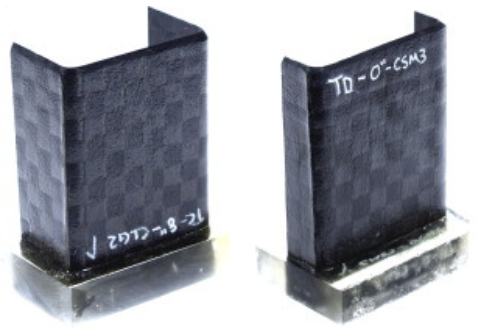

(b) Large and small C-channel specimens [75]

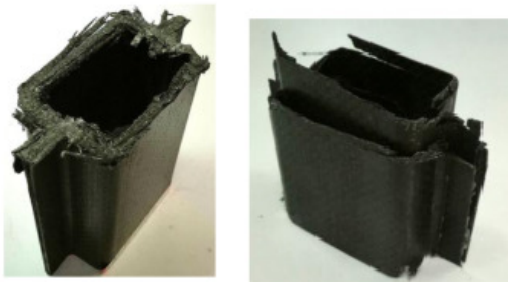

(c) Damaged double hat shaped tube specimens [76]

(d) CFRP truncated cone [77]

Fig. 2.12 Different self-supporting specimens used for crush analysis of composites.

reproducible, and reliable characterization methods, test specimens ought to be flat. Since composite plates tend to buckle, an anti-buckling fixture is necessary during the crush experiment.

This idea goes back to the beginnings of 1990s when Lavoie in a collaboration between NASA and Virginia Polytechnic Institute redesigned a quasi-static crush test fixture for composite plates, Figure 2.13 [78]. With the lateral knife edge supports the plate was fixed in its position while being crushed. The fixture was used in other studies as well to study the effects of geometric scaling, stacking sequence, and trigger mechanism of different materials under both quasi-static and dynamic conditions [78–80].

Dubey and Vizzini developed a similar fixture in 1996, Figure 2.14a, and tested 34 composite plates under quasi-static conditions with it [81]. Their fixture had the possibility of having an inclined crushing platen to study how it affects energy absorption of the plates. Couple of years after them, Daniel et al. designed a similar fixture with the supporting knife edges through the length of specimen, Figure 2.14b,

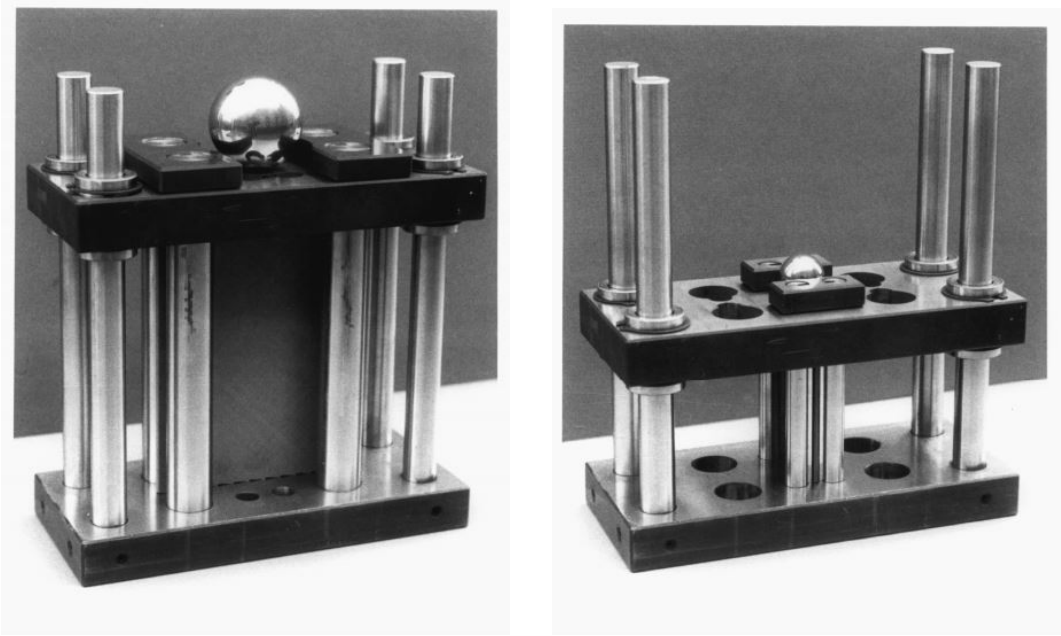

(a) Full scale specimen (b) Half scale specimen

Fig. 2.13 NASA fixture to test scale effect in energy absorbing composite plates [78].

[82, 83]. It was capable of having specimens with various thicknesses and changing the support position to study how unsupported width could affect plates crushing.

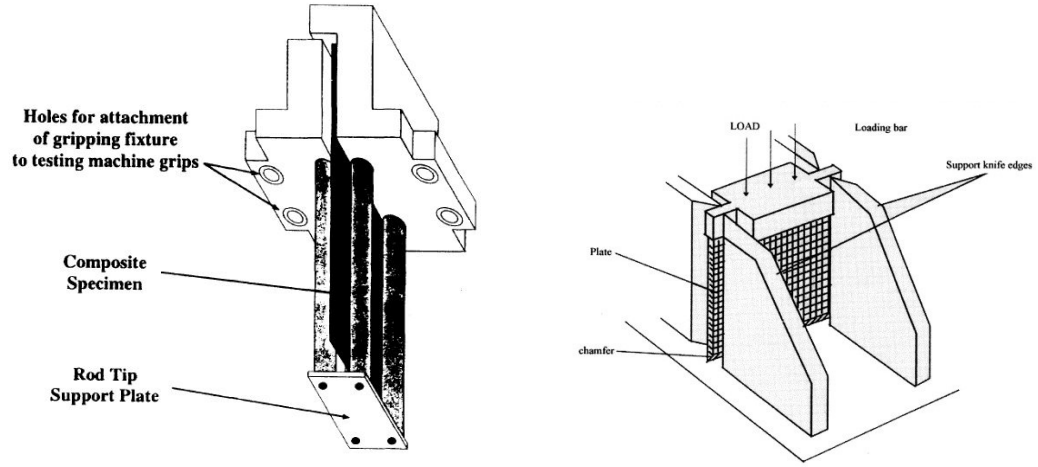

(a) Fixture by Dubey and Vizzini [81] (b) Fixture by Daniel et al. [82]

Fig. 2.14 Examples of two fixtures with fully lateral edge supports developed in 1990s.

In all of these three fixtures, the full lateral edge supports made composite plates to tear at the edges. Furthermore, fronds formation and curling up was not allowed

which caused jamming of the specimen and obtaining unrealistic compression force data. In 2003, Jacob et al. suggested a new test method to evaluate mechanisms of energy absorption in composite plates rather than using tubes [84]. A new test fixture was designed to progressively crush composite plate specimens under quasi-static test conditions and claimed to have the possibly for dynamic tests with minor modifications [85].

Some of the new features of their fixture were roller supports to prevent buckling, observable crush zone, long crush length of 51 mm, and interchangeable contact profile [84]. Figure 2.15 shows the fixture and its feature of interchangeable contact profiles. The fact that fixture was designed to replicate splaying mode in composite tubes and produced only damage modes related to fronds formation, held it back from exactly representing crush of composites.

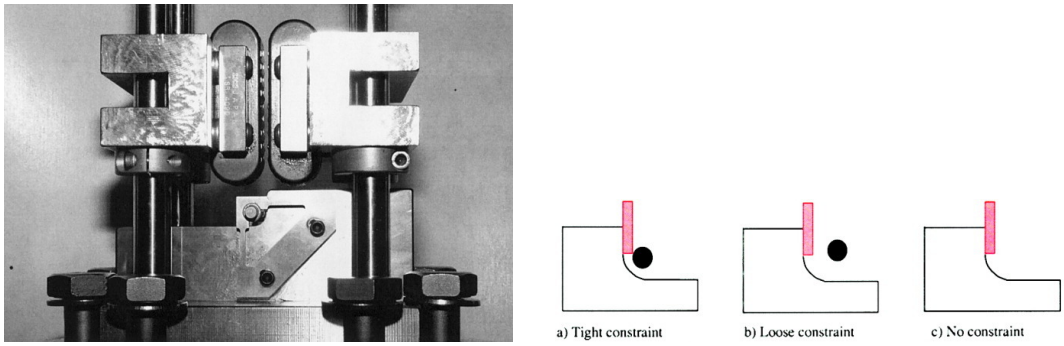

(a) Roller ways and contact profile constraint. (b) Different constraint conditions.

Fig. 2.15 Fixtures developed by Jacob et al. to study the splaying mode happening in crushing composites [85].

Couple of years after Jacob et al., Engenuity [1], a company conducting design and stress analysis for the various industries, in collaboration with other beneficiaries of Composite Materials Handbook-17 committee developed their testing fixture, Figure 2.16. Using this test rig under quasi-static and dynamic conditions, they succeeded in developing CZONE software for composite crash prediction.

[1] https://engenuity.net/

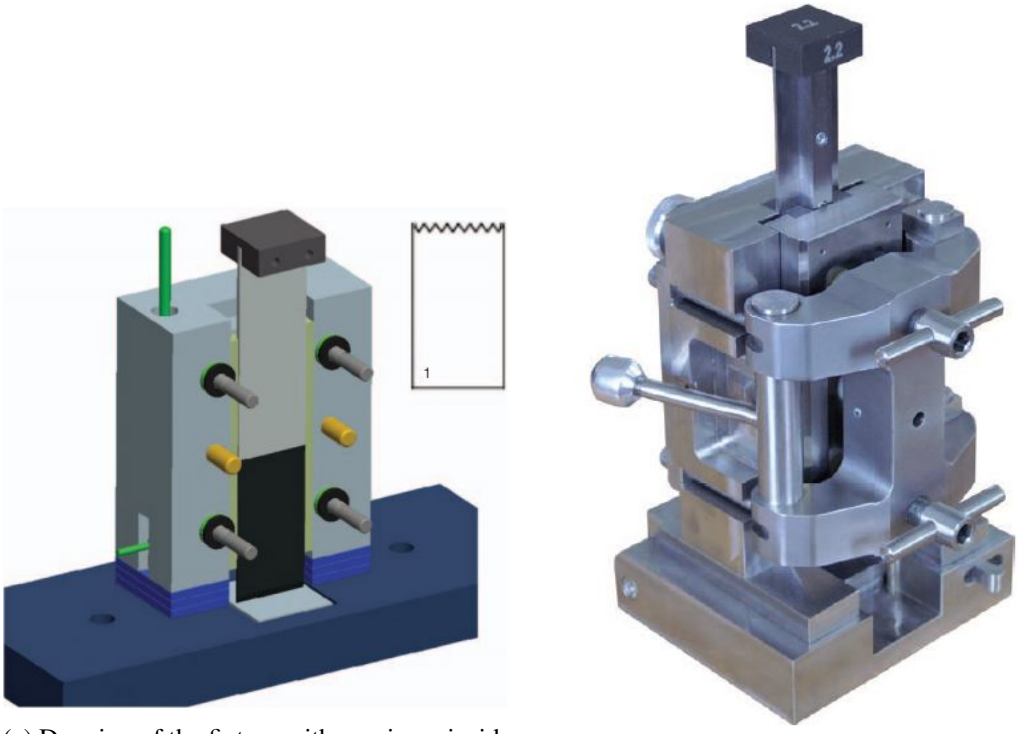

(a) Drawing of the fixture with specimen inside [86]

(b) Image of the fixture [87]

Fig. 2.16 Drawing and image of the test fixture developed by Engenuity.

The fixture was designed for specimens with various thicknesses between 1.2 and 10 mm and could produce stable crushing under quasi-static and dynamic conditions. Its drawbacks were requiring extensive calibration, fully constraining the specimen, and the probability to jam because of large fronds and debris [88].

In 2009, considering the absence of standard test methods for SEA characterization of composites, Feraboli designed and developed a fixture for crush energy absorption evaluations with the utilization of flat plate-like specimens, Figure 2.17 [88]. The adjustable unsupported height and the gap between supporting plates allowed the researchers to study various parameters effects and observe failure mechanisms such as fragmentation, frond formation, local and global buckling based on the chosen parameters [21, 88, 89, 75].

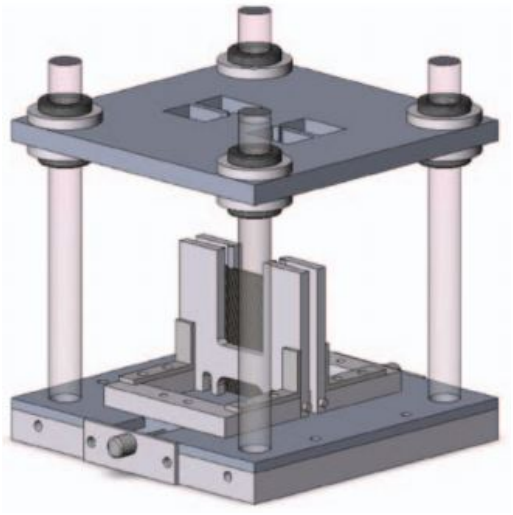

(a) CAD design

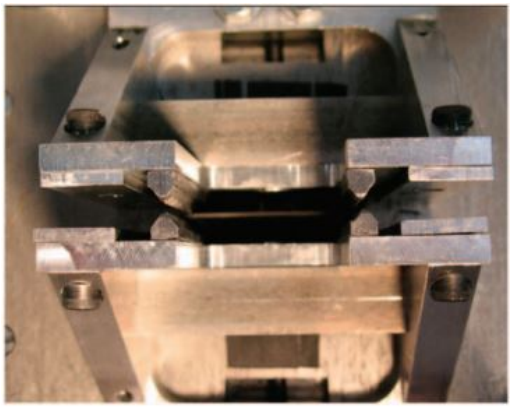

(b) Top view showing the knife-edge supports

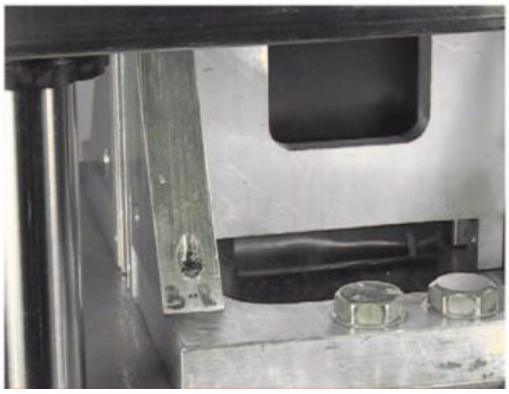

(c) Space for fronds formation and curling up

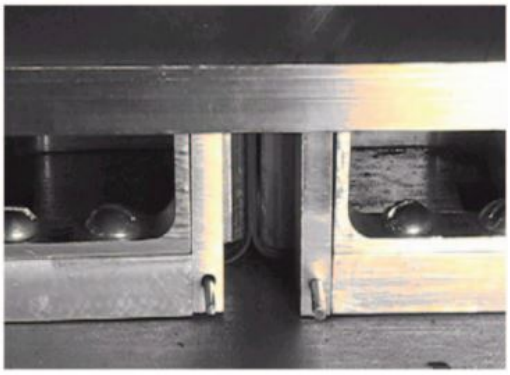

(d) Side view showing the unsupported height

Fig. 2.17 The specialized test fixture developed by Feraboli to measure composite crush energy absorption using flat-plate specimens [88].

Tearing at the edges due to the knife-edge supports, upper plate exclusively designed for 2mm thick elements, and using half scale specimens were some of the main shortcomings of this fixture. In other standard test methods for composite plates, such as ASTM D7136 for damage resistance of a composite to a drop-weight impact [90] or ASTM D7137 for compressive residual strength properties of damaged polymer matrix composite [91], the suggested size for the rectangular plate is twice the size used by Feraboli.

Another more recent test fixture for composite plates is developed by Feindler during his doctorate studies at TU Munich, Figure 2.18 [92]. The author could successfully stimulate progressive crushing and study various triggering system

effects and use the acquired data as input for further numerical studies. However, the fact that testing sample is constrained on three edges causes tearing of the specimen from those regions and therefore higher SEA values. This will be efficient only if tearing occurs in the final structure as well.

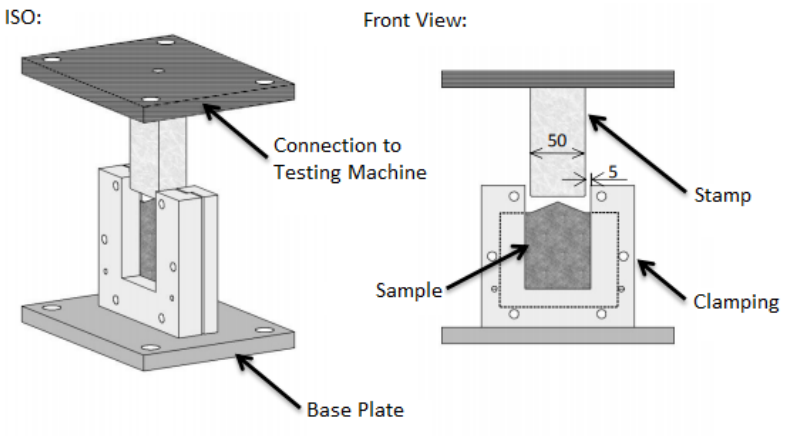

Fig. 2.18 Fixture developed at Technische Universität München [92]

The most recently developed fixture is designed by Lausch et al. [93] which to some good extend is similar to the fixture developed by TUM researchers. In order to eliminate the effects of unsupported length, as in the case with Feraboli and Engenuity fixtures, their specimen is fully constrained on the edges. Lausch et al. claim that the force displacement results obtained during the test is combination of crushing force and splitting force and to measure the specific energy absorption, the portion of energy related to each of these forces should be calculated [93]. Figure 2.19 shows the schematic drawing of the fixture and the whole testing setup.

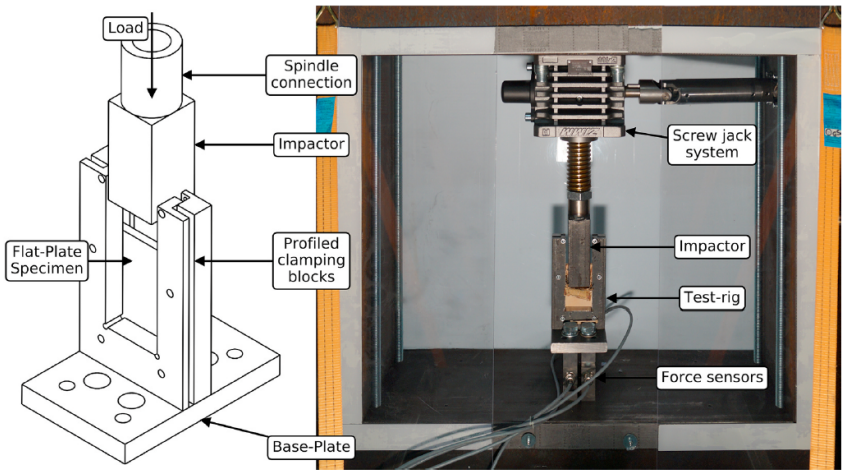

Fig. 2.19 Schematic drawing of the fixture developed by Lausch et al. and the whole testing setup [93].

To isolate and separate the contribution of either of these forces in the final absorbed energy, the authors consider splitting energy being independent of the crushing width. Therefore, by performing several tests with different crushing width and then extrapolating the results to hypothetical zero width, they have been able to calculate the splitting energy. Deducting this splitting energy from the total energy, they have evaluated the SEA for discontinuous carbon fiber composite and three wooden plates [93]. The paper is new and further investigations and experiments on different materials are needed for the through evaluation of the authors' claims.

Chapter 3

Materials and Methods

In this chapter first the materials and specimens used for the tests at different levels of the building block approach are described. After that, the testing methods and facilities used to perform them are discussed.

3.1 Materials

Two kinds of materials were used for this research study. The main material was high strength carbon fiber reinforced epoxy fabric with 2×2 twill structure produced by Microtex Composites SRL[1] with the commercial name GG630T-37 [5]. It was used during all test levels in the building block.

The other material was glass fiber fabric and epoxy resin with commercial name NEMA FR4 [94] which was used only during the element level tests to evaluate the reliability of the newly developed fixture and the repeatability and reproducibility of the obtained results for the crashworthiness evaluation of composite plates. Table 3.1 reports the mechanical properties of these two materials according to the data-sheets provided by the suppliers.

[1] https://microtexcomposites.com/en/

Table 3.1 Mechanical characteristics of the composites according to the suppliers' data sheets.

	NEMA FR4 Glass Fiber Epoxy [94]	GG630T-37 Carbon Fiber Epoxy [5]
Density	2.07 kg/dm^3	1.56 kg/dm^3
Elastic modulus	24 *GPa* (ISO 178)	60 *GPa* (ASTM D3039)
Tensile strength	300 *MPa* (ISO 527)	946 *MPa* (ASTM D3039)
Flexural strength	500 *MPa* (ISO 178)	624 *MPa* (ASTM D0790)
Compressive strength	350 *MPa* (ISO 604)	325 *MPa* (ASTM D3410)

Flat rectangular specimens of these materials with 150×100 *mm* dimensions were used for the element level experiments. For the better initiation of the progressive crushing, they were triggered with saw tooth pattern. Figure 3.1 shows images of these specimens.

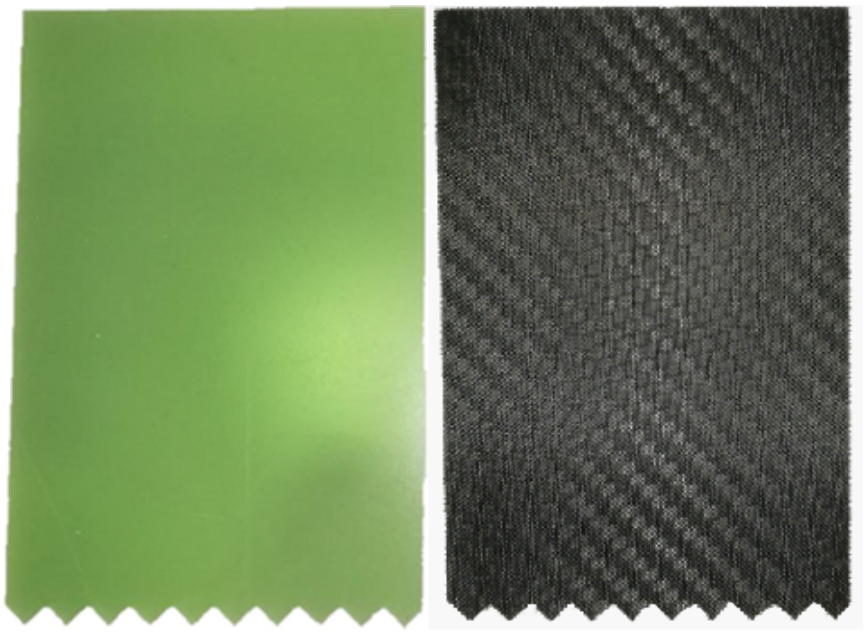

Fig. 3.1 Saw tooth triggered flat specimen made of NEMA FR4 glass fiber, left, and GG630T-37 carbon fiber, right, used for element level tests.

3.2 Methods

As explained in the previous chapters, the main approach of this research study was according to the building block. For the coupon level tests, standards characterizations based on ASTM International standards were performed on the carbon fiber reinforced specimens. Table 3.2 summarizes these standards and the mechanical property characterized according to them.

Table 3.2 ASTM standards for material characterizations in the coupon level

Mechanical Property	Standard
Tensile	ASTM D3039 [95]
Compressive	ASTM D3410 [4]
Shear	ASTM D3518 [3]
Flexural	ASTM D790 [2]

To perform these tests, Instron® 8801 servohydraulic testing machine and ZwickRoell® Z100 with electromechanical drive at the laboratories of Politecnico di Torino were used. Both machiens were equipped with 100 kN universal hydraulic wedge action grips to hold the coupons in place during the tests. Figure 3.2 shows images of these machines.

3.2.1 Newly Developed Fixture

Moving upward in the building block's pyramid, a new anti-buckling fixture was needed to perform the element level tests on the flat specimens. As discussed thoroughly in the previous chapter, already available fixtures are either designed for a specific thickness [96] or for samples with smaller dimensions [86] than ASTM standards requiring composite plates [90, 91]. Therefore, having a fixture to support rectangular $150 \times 100\ mm$ specimens with various thicknesses was the main objective in this section.

To understand effects of different parameters on the reliability of the final fixture, finite element analyses (FEA) were performed in close collaboration with another PhD student at Politecnico di Torino, Ravin Garg. With this method, expensive and not efficient trial and error approach to manufacture the fixture was also avoided. Figure 3.3 shows the model used for FEA steps and gives information about the

(a) Instron® 8801 (b) ZwickRoell® Z100

Fig. 3.2 Testing apparatuses in laboratories of Politecnico di Torino used for the mechanical characterizations of CFRP specimens in the coupon level tests: (a) servohydraulic Instron® 8801 and (b) electromechanical ZwickRoell® Z100

properties chosen for the component materials and their contacts. HyperWorks simulation software packages were used in these steps. Final model was pre-processed by HyperMesh, solved by Radioss, and analyzed with HyperGraph and HyperView.

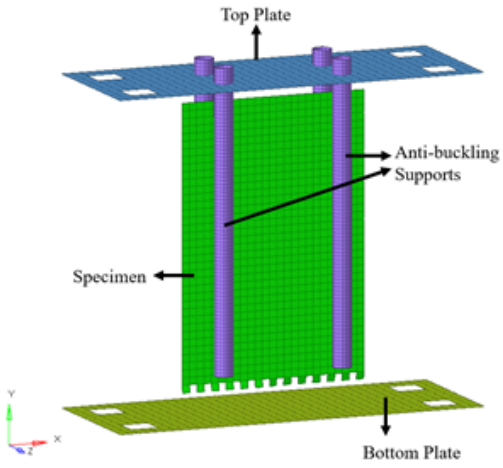

Component	Material (Numerical Material Law)
Top Plate (Rigid Body)	C40 Steel (Johnson-Cook Elastoplastic Law 2)
Specimen	Carbon fibre reinforced epoxy (CRASURV Law 25)
Supports (Rigid Body)	C40 Steel (Johnson-Cook Elastoplastic Law 2)
Bottom Plate (Rigid Body)	C40 Steel (Johnson-Cook Elastoplastic Law 2)

Component Pair	Contact Model	Friction Co-ef
Top Plate + Specimen	Node-to-element (Type 7)	0.3
Supports + Specimen	Surface-to-surface (Type 24)	0.3
Base + Specimen	Node-to-element (Type 7)	0.3
Specimen Self Contact	Node-to-element (Type 7)	0.2
Top Plate + Supports	No contact defined	--

Fig. 3.3 FEA model setup of the newly developed fixture and materials and contacts information for different components using HyperWorks simulation [97].

The first property which was simulated was the thickness of the upper plate. The main purpose of the upper plate is to transfer the force and energy from the impactor to the supported specimen. Since the fixture was being designed to withstand impacts with up to 1850 *J* energy, the upper plate was virtually impacted at this energy and deformations and damages in the impacted zones were closely monitored for three different thickness of 10, 20, and 30 *mm*.

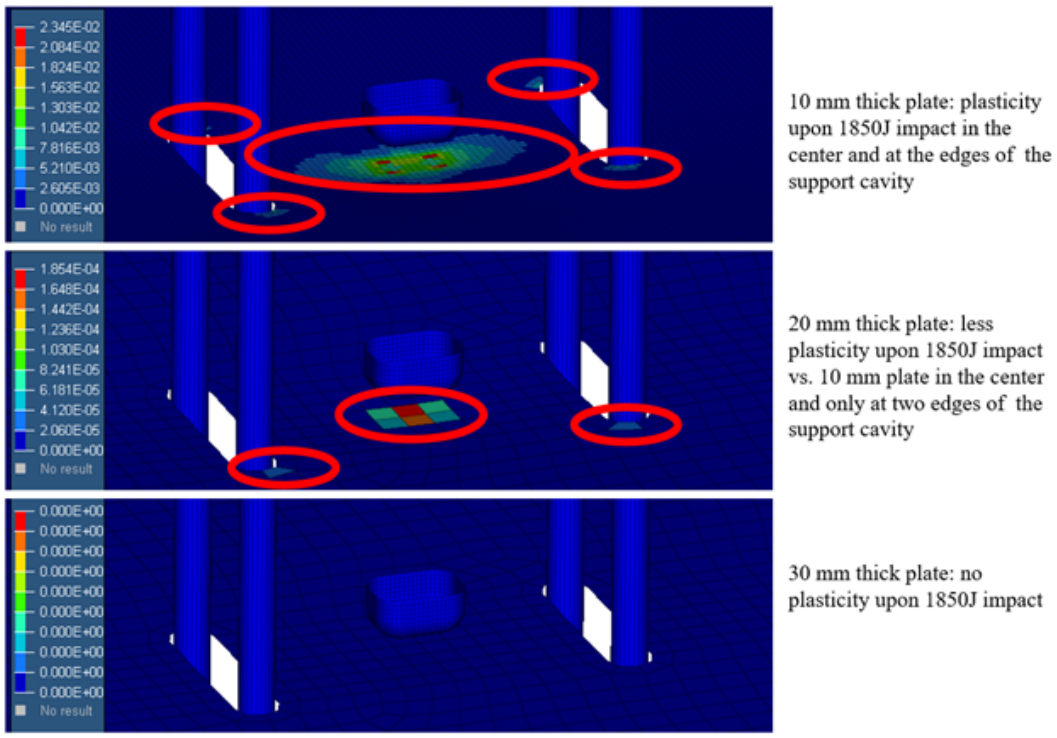

Fig. 3.4 Deformation of the upper plate under impacts with 1850 *J* energy having thicknesses of 10, 20, and 30 *mm* [97].

As illustrated in Figure 3.4, plastic deformations in the center of the plate and damages on gap edges for the supporting columns were observed for both 10 and 20 *mm* thick plates. On this account, 30 *mm* was chosen for the thickness of the upper plate in the final design. This thickness for the square shaped upper plate made of C40 Carbon Steel would have weighted 17 *kg*. This could affect the functionality and user experience of the final fixture. Therefore, some design optimization procedures were followed. Figure 3.5 outlines these undergone steps which helped to reduce the upper plate's weight to 4.152 *kg*.

After gaining confidence that the upper plate will tolerate ultimate impact energies of the Instron drop towers, the distance between the columns and their effects

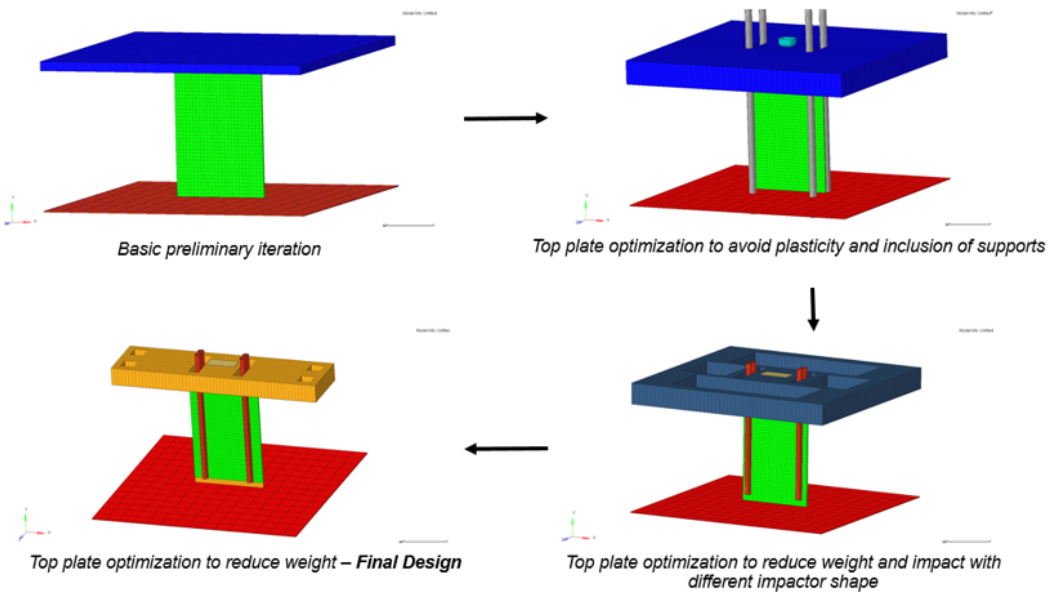

Fig. 3.5 Design optimization of the upper plate with weight reduction purposes [97].

on the specimens buckling were studied. Since in the literature it was proven that knife edge supports cause tearing of the specimen, only cylindrical columns were modeled. These simulations were performed at three different distances of 50, 65, and 80 *mm* between the central axis of supporting columns. In the case of 50 *mm* distance, local buckling was observed. On the other hand, when the distance was set to 80 *mm*, damages at the upper part of the specimen took place. However, at 65 *mm* gap between the columns neither of these drawbacks were observed and therefore it was chosen as the distance for the final design. Figure 3.6 illustrates the results for these simulated cases.

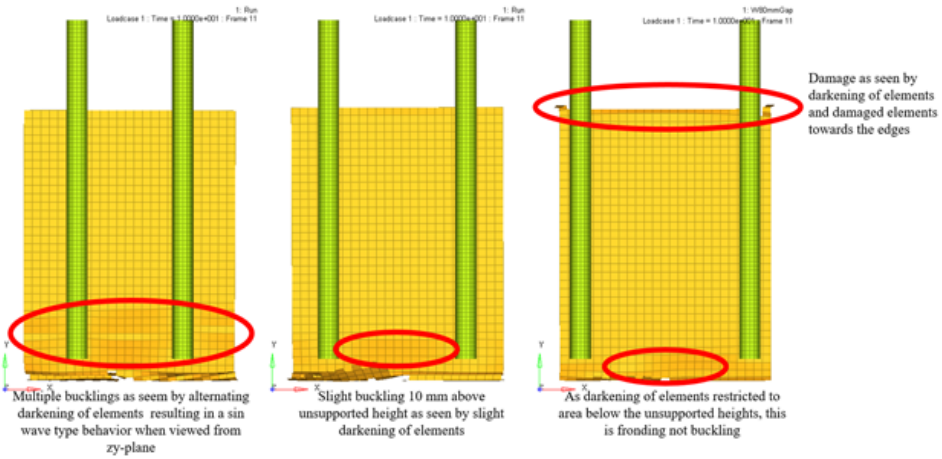

Fig. 3.6 Effects of distance between the cylindrical columns supporting flat specimens under impact [97].

The other studied aspect was the diameter of the supporting columns. Three different diameters of 5, 10 and 20 *mm* were investigated. The largest case of 20 *mm* led to fronding at the top and transformed the damage into a non progressive one in the bottom of the specimen. 5 *mm* thick columns caused local buckling due to the lack of lateral supports against vibrations. Meanwhile, 10 *mm* thick columns did not exhibit any of these flaws and proved to be the choice for the diameter of the anti-buckling supporting columns. Figure 3.7 demonstrates the results for these simulated cases.

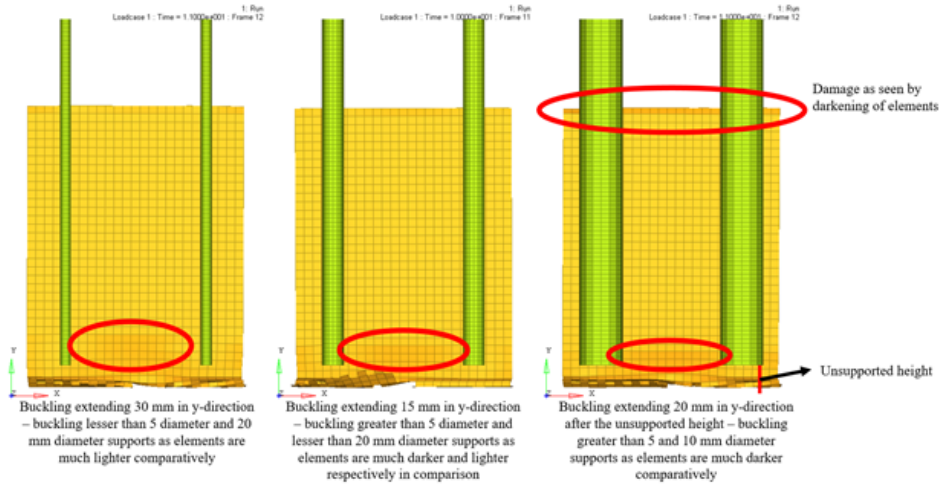

Fig. 3.7 Effects of the anti-buckling column diameters on the impact of the specimens. From left to right: 5 *mm*, 10 *mm*, and 20 *mm* in diameter [97].

Based on these optimization and simulation results, the first prototype version of the fixture was designed and manufactured. Figure 3.8a shows this fixture equipped with glass fiber reinforced epoxy for preliminary tests. Figure 3.8b demonstrates the fixture fixed in the bottom part of the Instron drop tower and the head of the impactor touching the upper plate.

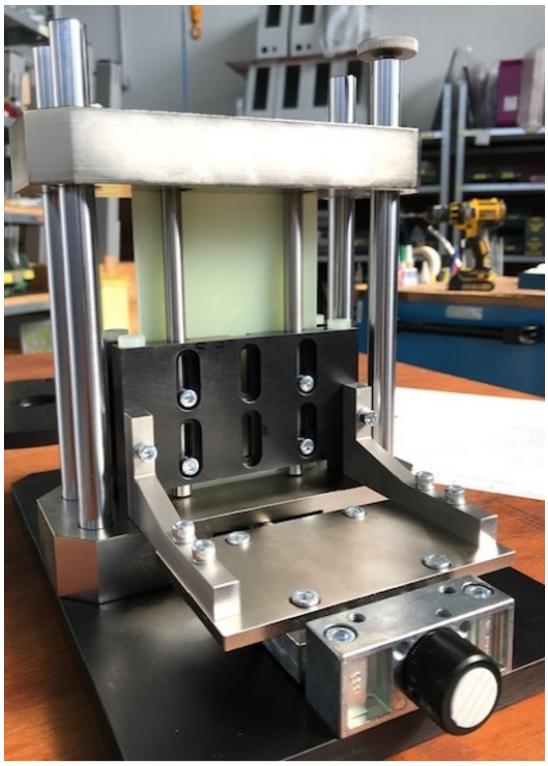

(a) Prototype fixture with GFRP element

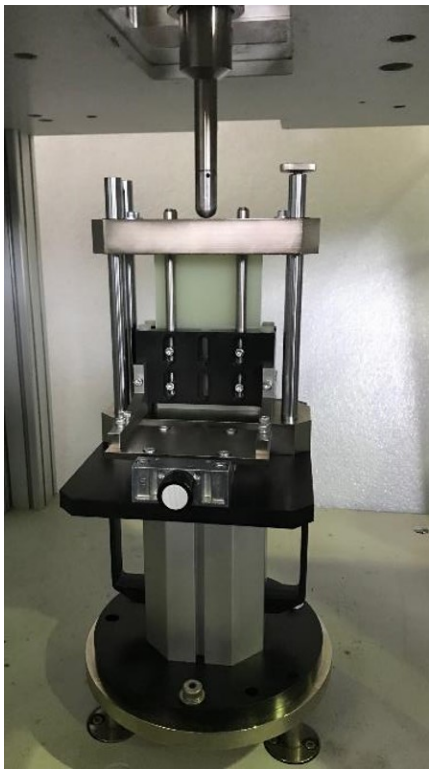

(b) Fixture at the chamber of drop tower

Fig. 3.8 First prototype anti-buckling fixture supporting a GFRP flat specimen, (a), and the same fixture set at the chamber of Instron drop tower with the cylindrical impoactor touching the upper plate, (b).

To perform the preliminary tests, flat elements were triggered with a saw-tooth shape. It was proven to be reliable for progressive failure initiation in the composite plates in the literature [98]. Figure 3.9 shows the drawing of the specimen and its triggering mechanism.

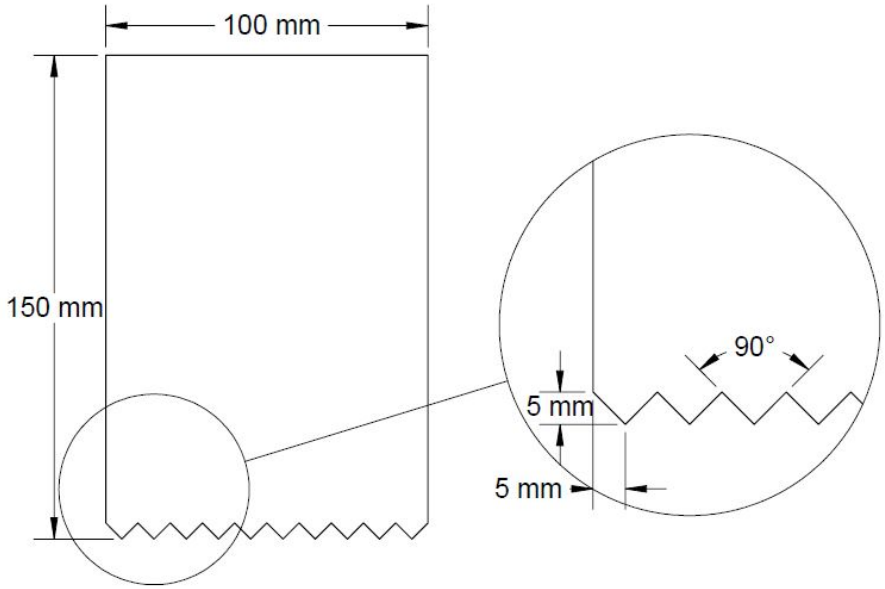

Fig. 3.9 Drawing of the sample and triggering system used for SEA calculation of flat elements

While primarily evaluating the functionality of the fixture, outward opening of the supporting plates was observed. Figure 3.10 illustrates these failures which caused buckling and fracture of the specimens in the top portions.

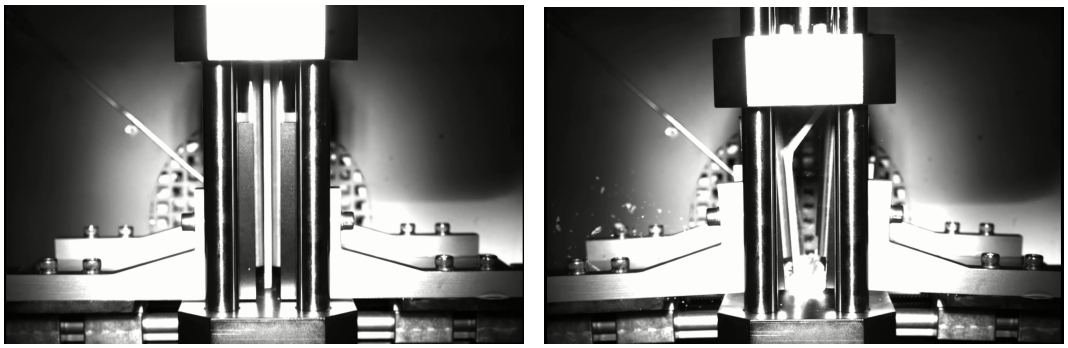

(a) Beginning of the experiment (b) At the end of the experiment

Fig. 3.10 Failure of the initial lateral supports in the first prototype of the newly developed fixture under impact tests.

This failure was due to the lack of supports by lateral supports. To overcome this drawback, these "L" shaped supports were substituted with triangular ones which properly supported the specimens. Figure 3.11 compares these two kinds of supports.

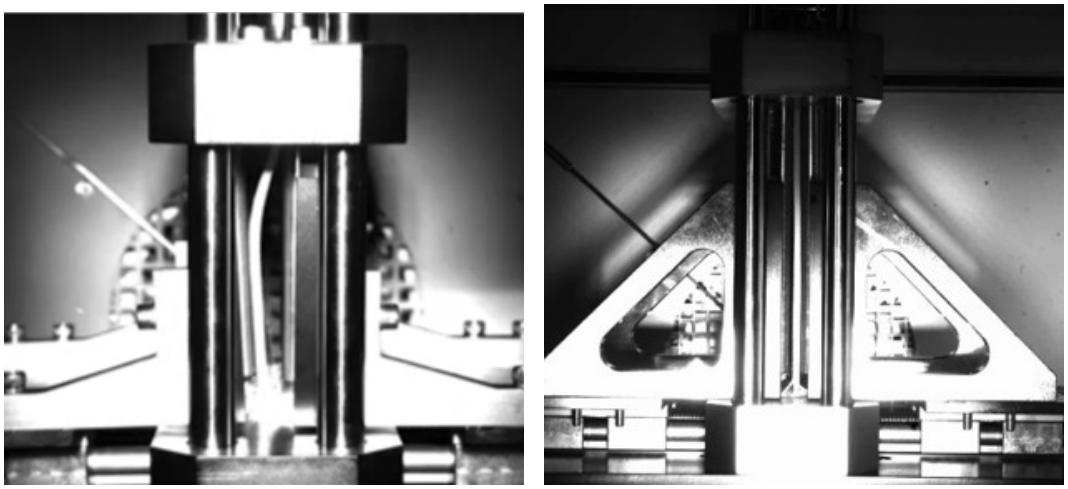

(a) L-shape supports failing to maintain specimen in position under impact

(b) Triangular supports successfully holding the specimen in position while being crushed

Fig. 3.11 Two different lateral supports: (a) L-shaped ones which caused opening of the fixture and buckling of the specimen. (b) Triangular ones that kept the flat specimen in place while being crushed under impact.

Figure 3.12 shows the final version of the newly-developed anti-buckling fixture and explains its various parts. A top plate with 30 *mm* thickness positioned above the CFRP element with four guide columns to transfer the load from the dropping weight impactor to the specimen. 10 *mm* gap was designed at the base of support plates to avoid the undesired interaction between fronds and fixture while being crushed and allow the curling up to take place. This interaction was a problem in fixtures developed by NASA and University of London [99, 100]. Four rubber inserts on the top of support plate would take the residual energy not absorbed by the specimen and prevent damaging the fixture.

The gap between guide columns makes it possible to have a high speed camera in place and study the procedure of progressive crushing from that angle in real time. This was an advantage compared to the Engenuity fixture which required extensive calibration and fully constraint specimen [86]. The fixture is screwed to the chamber at the bottom of Instron CEAST 9400 drop tower impact apparatus, Figure 3.13a [101], capable of providing up to 1850 *J* impact energies. The top plate transfers the

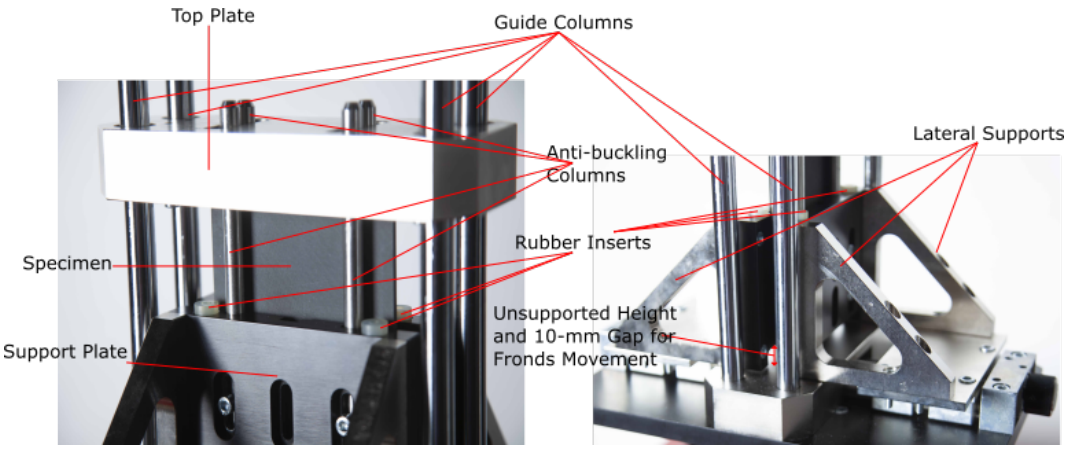

Fig. 3.12 Newly developed anti-buckling fixture for crashworthiness evaluations of flat composite plates.

load from the impactor cross head, integrated with a load cell to measure the force, to the supported triggered specimen.

Impact energy for test programs during the element block were provided by a falling weight of known mass and velocity inside Instron 9450 drop weight tower. The striker was equipped with a 222 kN load cell and connected to the acquisition system with sampling frequency of 1 MHz. To achieve different impact energies, either impact height or mass was modified. These tests were recorded using a Photron FASTCAM Mini AX [2] high speed camera with a resolution of 1024×1024 pixels at the rate of 6400 frames per second. These videos helped observing the failure modes and also track the displacement of the specimen being crushed.

[2] https://photron.com/mini-ax/

(a) Instron 9400 Series Impact Drop Tower [101] (b) Newly developed anti-buckling fixture.

Fig. 3.13 Images of the drop tower (a) and the anti-buckling fixture (b) used for energy absorption evaluations of the flat composite specimens.

Since metallic cross head impacts the metallic upper plate, huge initial peaks in the range of $60-90$ kN appear at the beginning. Immediately after that, due to inertia, the contact between the cross head and top plate is lost and for some milliseconds the measured force drops to zero values. When the cross head and top plate contact each other again, the second peak appears in the obtained data but this time the contact is not lost until the end of experiment. Results in this range are used for calculating specific energy absorption and mean forces [102]. All these areas are shown in Figure 3.14.

SEA is measured with the cumulative trapezoidal numerical integration of the force displacement data in the stable area, shown in Figure 3.14, and dividing it by

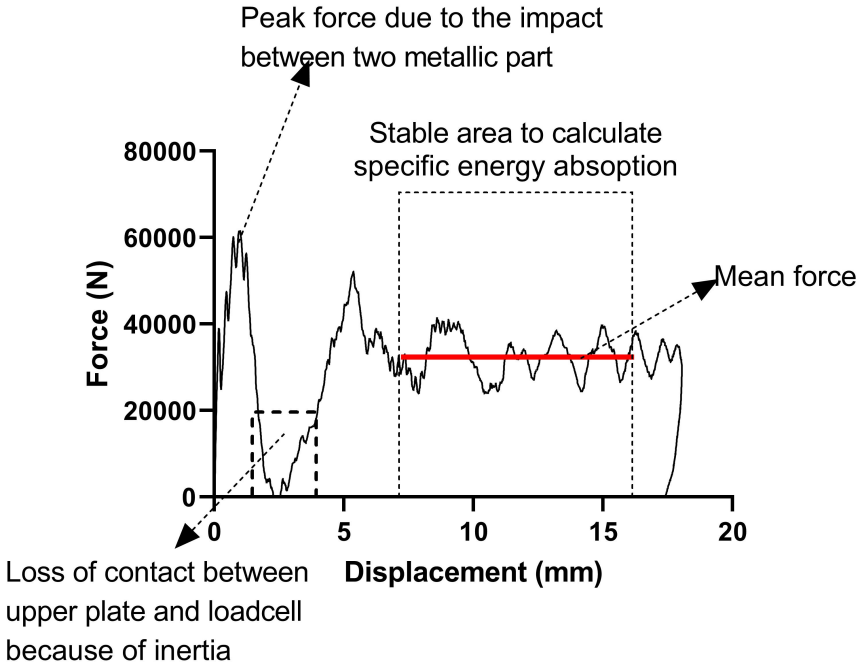

Fig. 3.14 Force displacement result obtained from the newly developed fixture.

the mass of crushed part in this area. To calculate the mass, cross sectional surface area is multiplied by the displacement inside stable area and then by the density, as suggested by Equation 3.1, which was discussed in the previous chapter and is reported here again:

$$SEA = \frac{W}{\rho A \delta} = \frac{\int_0^{\delta} F d\delta}{\rho A \delta} \tag{3.1}$$

where W is the total energy absorbed during the experiment, ρ is the material's density, A is the cross sectional surface area, δ is the crush displacement, and F is the crush force.

Another PhD student, Lorenzo Vigna, is currently working on further modification of the fixture in collaboration between PoliTo and Instron ITW. One of the suggested modifications is eliminating the upper plate and applying the force directly to the element by using a falling circular disk. Figure 3.15 shows the falling disk on striker beside the hemispherical insert of the striker impacting upper plate.

Results obtained from this slightly modified version were encouraging, because the initial peak forces were omitted and contact between the element and striker was never lost. Figure 3.16a compares the results acquired from these both meth-

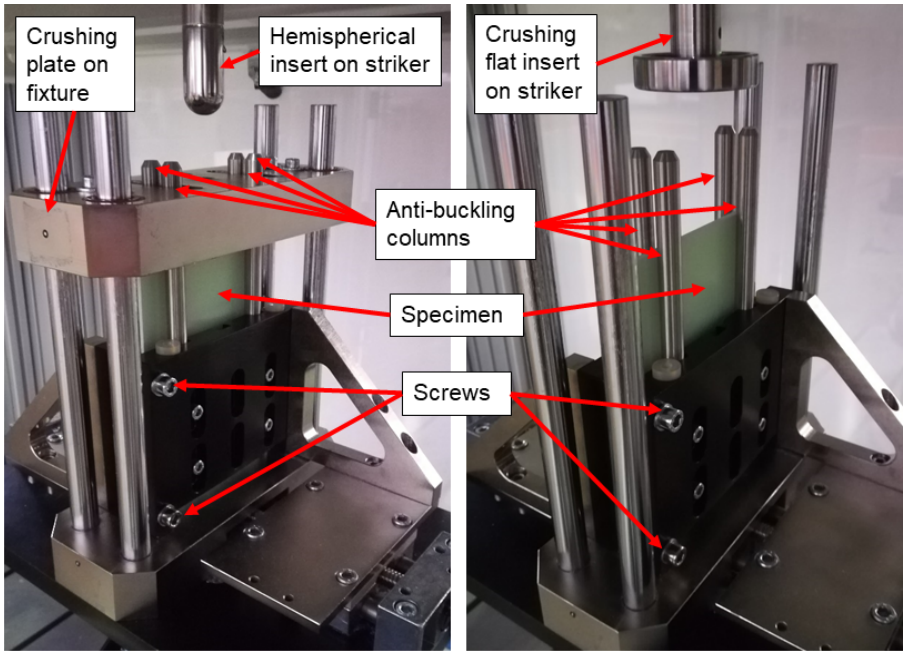

Fig. 3.15 Two methods of apply the impact force on the flat element: impacting the upper plate with the hemispherical insert on the striker, left, or impacting directly the element by using the flat insert, right [102].

ods. Since the forces are similar in the stable progressive crushing area, results acquired from the original method of impacting the upper plate with hemispherical insert on striker are reliable and not affected by the interaction between the metals. Unfortunately, around 50% of elements were crushed from the upper part, Figure 3.16b, which necessitates further modification of the fixture if direct impacting of the element is desired. This is an ongoing research activity.

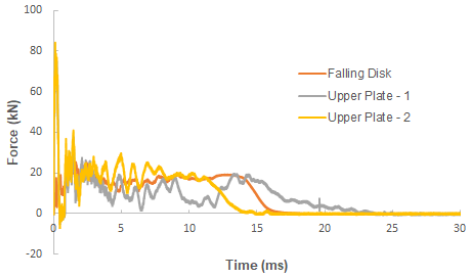

(a) Comparison of obtained results between impacting upper plate and using falling disk

(b) Improper crush of element from the top

Fig. 3.16 Results from directly impacting the elements using circular disk insert on the striker, (a), and unfortunate topside fracture of the specimen. All tests performed on CFRP elements at 550 J energy with 4.67 m/s velocity and 50 kg impact mass.

Looking at the high speed camera videos of the experiments and analyzing the crushed elements at the end of each test, reveals the efficiency of triggers and the energy absorption mechanisms. The two outer layers open outward and absorb energy by splaying and delamination. Two inner layers are partially crushed and absorb energy by fragmentation. These results are fully discussed in the next chapter. Figure 3.17 shows a crushed element from two angles.

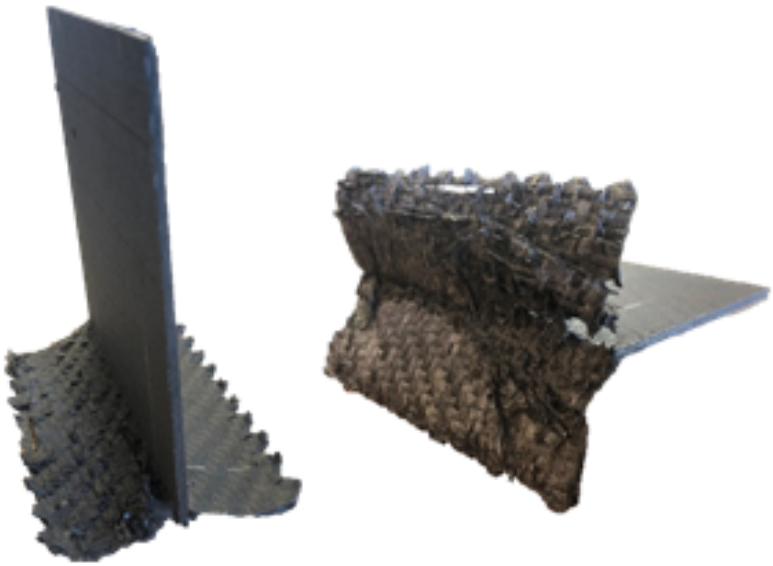

Fig. 3.17 Crushed elements after being impacted. Splaying of the outer layers and fragmentation of the inner ones are the main energy absorption mechanisms.

These results were promising enough to perform actual experiments on the CFRP specimens for the element level of building block approach for our research. Two main goals were pursued during the experiments in this level. First, to develop a methodology for crashworthiness evaluations of polymer matrix composites. Second, to help tuning the simulation results performed by another PhD student at Politecnico di Torino, Ravin Garg.

3.2.2 Crash demonstrator

Moving upward in the building block pyramid, for the final tests of the component level, six crash demonstrators were manufactured. These demonstrators had three sections with different thicknesses that acted as a triggering mechanism and helped to have a stable progressive crush of the specimen. Figure 3.18 shows an image of

this demonstrator and specifies the length of different sections. This geometry of the impact attenuator was manufactured for a Formula SAE racing car and proven to ascertain progressive and controlled deformation under numerical and experimental investigations by Boria et al. [103].

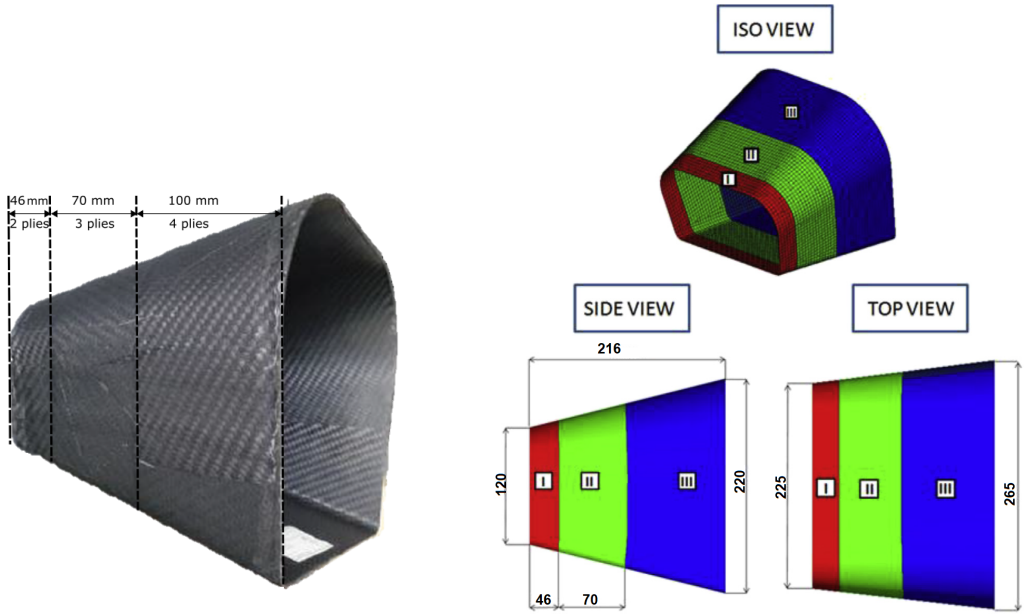

(a) Crash demonstrator (b) Geometrical configurations [103]

Fig. 3.18 (a) Crash demonstrator manufactured with different number of plies in each section to initiate a stable crush and (b) schematic of the geometrical configurations of the component.

Two of them were used in quasi-static tests with the application of ZwickRoell® electromechanical testing machine at 10 mm/min speed. The remaining four components were used for dynamic crash evaluations using drop weight testing facility at Picchio Spa[3] in Ancarano, Italy. Their drop tower has a maximum height of 6 meters and is capable of providing up to $26,000$ J impact energies. For our test program, falling mass of 300 kg equipped with MMF_KD38V piezoelectric accelerometer, photocell to measure the impact velocity, and high-speed camera to record the test with 1000 frames per second were used. Figure 3.19 shows the drop tower and its data acquisition facilities.

[3] http://www.picchio.com/

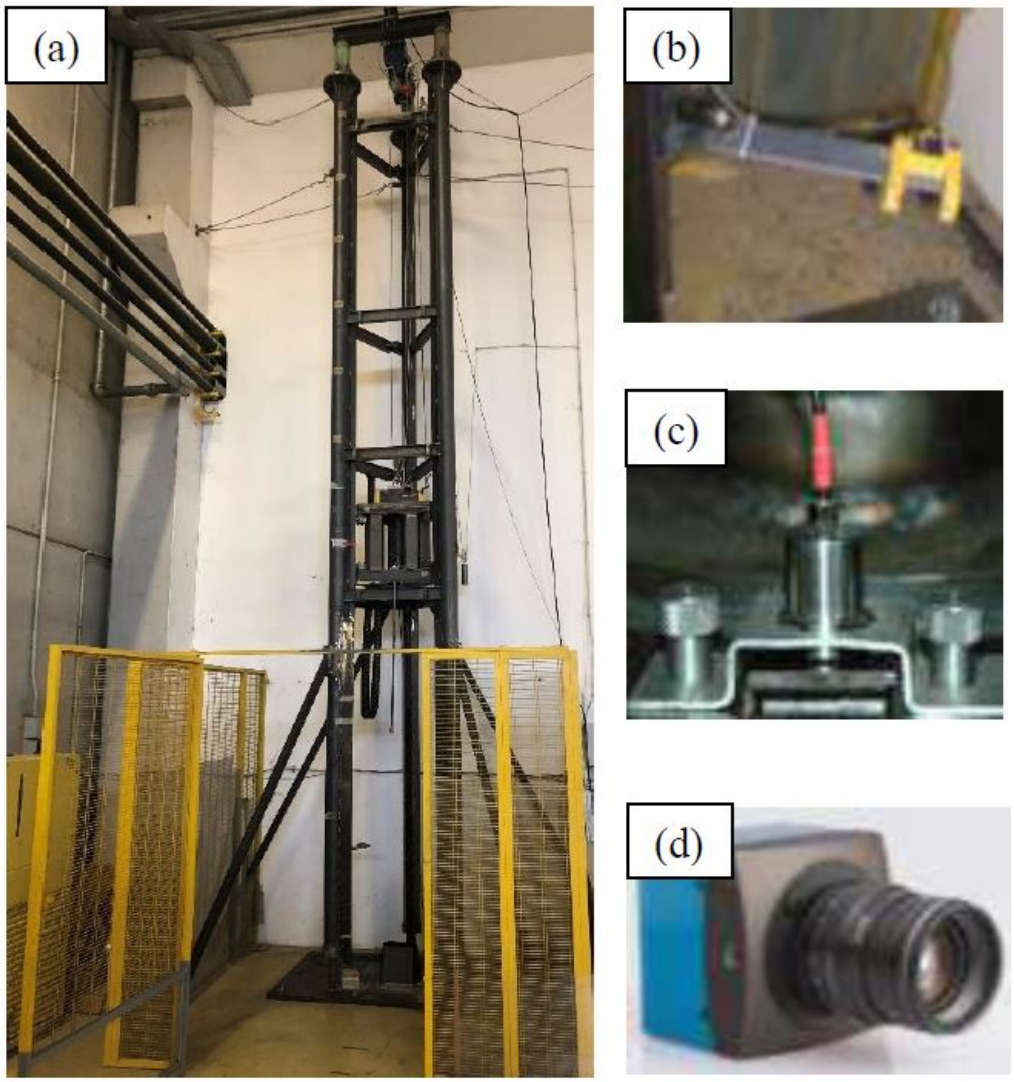

Fig. 3.19 Image of the drop tower at Picchio Spa (a), photocell in the exact height for impact velocity measurements (b), MMFKD 38V piezoelectric accelerometer (c), and high-speed camera (d).

The main purpose of these tests on the components was to compare the results with the simulated ones and to work as a proof of concept for the modelling process. In the next chapter the results obtained from these methods and materials are reported and discussed.

Chapter 4

Results and Discussion

In this chapter, results of the experiments carried out in the past three years are reported and discussed. In the first section, materials characterization tests in the basic coupon level of the building block approach are discussed. Then, the element level tests results and the newly developed anti-buckling fixture for these tests are discussed. Finally, in the last section, results for the component level tests on CFRP demonstrators are presented.

4.1 Coupon Level

Tests in this basic level were performed according to different ASTM standards for the mechanical characterization of the polymer matrix composite materials. To carry out these characterizations, two testing apparatuses (Section 3.2.1) available in the laboratories of Politecnico di Torino were utilized.

First, in-plane tensile properties were obtained following the ASTM D3039 [95] test method. Initially, five samples with constant rectangular cross sections were mounted in hydraulic wedge action grips and monotonically loaded in tension. These not-tabbed specimens had widths of 25 mm, lengths of 250 mm, and thicknesses around 2.5 mm. The cross head had a constant displacement rate of 2 mm/min to keep the strain rate around 0.01 min^{-1}. The 100 kN universal hydraulic grips recorded the force data which were later used for calculating the stress and the ultimate strength of the material, from the maximum force before failure.

By employing extensometer, strain data in the longitudinal direction were gained and used for studying the stress-strain response of the material, Figure 4.1a. From that, the ultimate tensile strain and tensile modulus of elasticity were calculated. All these characterizations are summarized in Table 4.1. Then, two more coupons were tabbed using the rectangular parts made of same material and glued by curing epoxy resin inside the oven. These tabbed ones showed the same stress strain curves as before. Therefore, no more tabbed specimens were examined to save in the time and material.

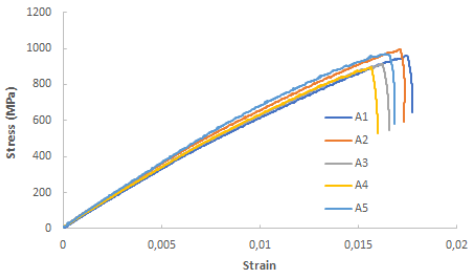

(a) Stress-strain response of CFRP specimens under tension

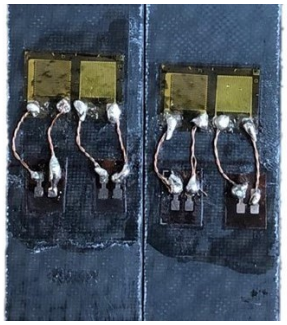

(b) Coupons with strain gauges

Fig. 4.1 (a) Stress-strain responses of five not-tabbed CFRP specimens under tension; (b) CFRP coupons with HBM® strain gauges attached to their centers.

For tensile chord modulus calculations, obtained data in the longitudinal strain range of 1000 $\mu\varepsilon - 3000\ \mu\varepsilon$ and Equation 4.1 were used.

$$E^{chord} = \Delta\sigma/\Delta\varepsilon \tag{4.1}$$

where E^{chord} is the tensile chord modulus of elasticity in GPa, $\Delta\sigma$ is the difference in tensile stress between 0.001 and 0.003 absolute strain points in MPa, and $\Delta\varepsilon$ is the difference between these two strain points (0.002) [95].

Table 4.1 Tensile properties of GG 630T-37 carbon fiber laminate folowing ASTM D3039 standard.

	Tensile Strength (MPa)	Tensile Modulus (GPa)	Yield Strain
A1	961	56.3	0.018
A2	994	60.8	0.017
A3	911	60.9	0.016
A4	893	58.3	0.016
A5	968	62.6	0.017
Average	946	59.8	0.017
Std Dev	37.5	2.2	0.001

To calculate the Poisson's ratio, HBM® 1-XY38-6/350 strain gauges with active gauge length of 6 *mm* and resistances of 350 Ω were attached to the surface of the samples. The active gauge length was greater than the characteristic repeating unit of the woven composite and with this high resistance, heating effects were eliminated. These double strain gauges accurately measured strain in both longitudinal and lateral directions. Equation 4.2 was used to quantify the Poisson's ratio.

$$\nu = -\Delta\varepsilon_t / \Delta\varepsilon_l \tag{4.2}$$

where ν is the Poisson's ratio, $\Delta\varepsilon_t$ is the difference in lateral strain between 0.001 and 0.003 absolute strain points, and $\Delta\varepsilon_l$ in the difference in longitudinal strain between these points [95].

Figure 4.2 shows the transverse and longitudinal strains under tensile traction for two tests performed according to the ASTM D3039 standard specifications. Due to the high data acquisition frequencies, close to 2 kHz, high oscillations of data were observed in both directions. Therefore, moving average filters with the application of rational transfer functions were used to obtain better visualizations of the data.

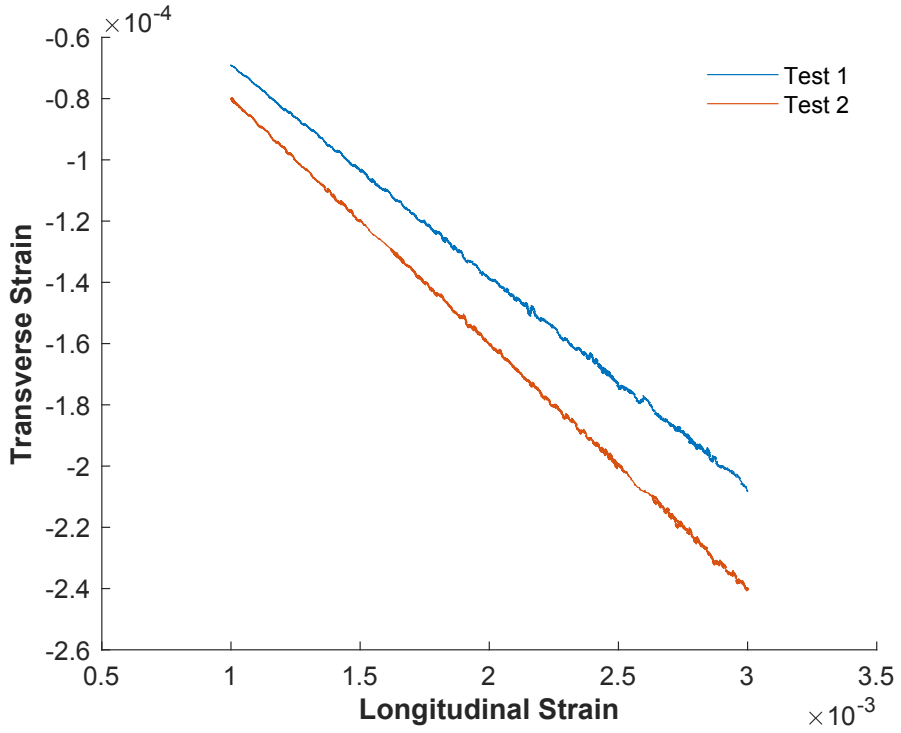

Fig. 4.2 Transverse and lateral strains during tensile characterization of CFRP coupons used for calculations of Poisson's ratio.

Later, using the same Instron servo hydraulic testing machine as before, but changing the cross head fixture, flexural properties of the material were measured following ASTM D790 standard steps [2]. To meet the span-to-depth ratio of 16 : 1, given that the specimens were 2.9 *mm* thick, span length of 47.04 *mm* was chosen. The overall length of the coupon was 150 *mm* which provided sufficient overhanging to prevent slipping of the specimens. Figure 4.3 shows an image of the specimen during the experiment alongside the schematic representation of supports and loading positions.

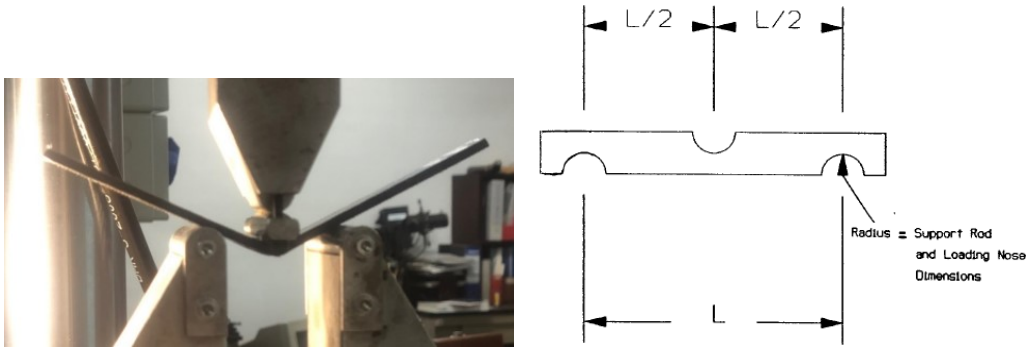

(a) Characterizing flexural properties (b) Schematic representation of the test

Fig. 4.3 (a) CFRP specimen undergoing flexural characterization experiment and (b) schematic representation of the support rods and loading nose positions based on ASTM D790 standard [2].

The loading nose and supporting rods had radii of 5.0 *mm* and the test speed was set to 1.25 mm/min. Force displacement data were acquired through the same 100 *kN* load cell as in the previous experiments. Figure 4.4 illustrates the obtained stress-strain results.

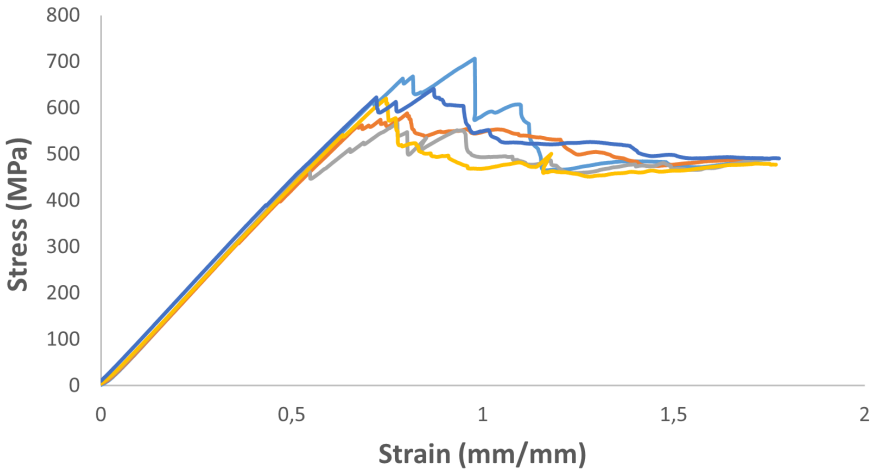

Fig. 4.4 Stress strain curves of the flexural properties for the CFRP coupons.

Stress was calculated using the equation below:

$$\sigma = 3PL/2bd^2 \tag{4.3}$$

where σ is the stress in the outer fibers at midpoint in *MPa*, P is the load at a given point in N, L is the support span (47.04 *mm*), b is the width of the coupon in *mm*, and d is its depth in *mm*. Strain was also calculated as follows:

$$\varepsilon = 6Dd/L^2 \tag{4.4}$$

where ε is the strain in the outer surface in mm/mm and D is the maximum deflection of the center of the beam in *mm* [2]. Table 4.2 summarizes the calculated flexural strength and modulus of the specimens.

Table 4.2 Flexural properties of CFRP specimens measured with respect to the ASTM D790 standard [2].

	Flexural Strength (MPa)	Flexural Modulus (GPa)
B1	706	73.0
B2	588	66.9
B3	567	68.9
B4	620	69.8
B5	641	71.1
Average	624	70.0
Std Dev	48.1	2.1

To calculate in-plane shear properties of our CFRP material, rectangular samples with 250 *mm* length and 25 *mm* width were cut in a way that fibers were oriented in $\pm 45^\circ$ inside the test specimen. Then, HBM® 1-XY38-6/350 double strain gauges with 350 Ω resistance and measuring grid lengths of 6 *mm* were attached to the center of coupons to measure the strain in both longitudinal and lateral directions. The cross heads were moving with the constant speed of 2 mm/min until the failure of the coupons. ASTM D3518 standard [3] recommendations were followed during these steps of characterizations. Figure 4.5a schematically represents the loading direction and fibers' $\pm 45^\circ$ orientations.

In-plane shear stress was calculated as:

$$\tau_{12_i} = \frac{P_i}{2A} \tag{4.5}$$

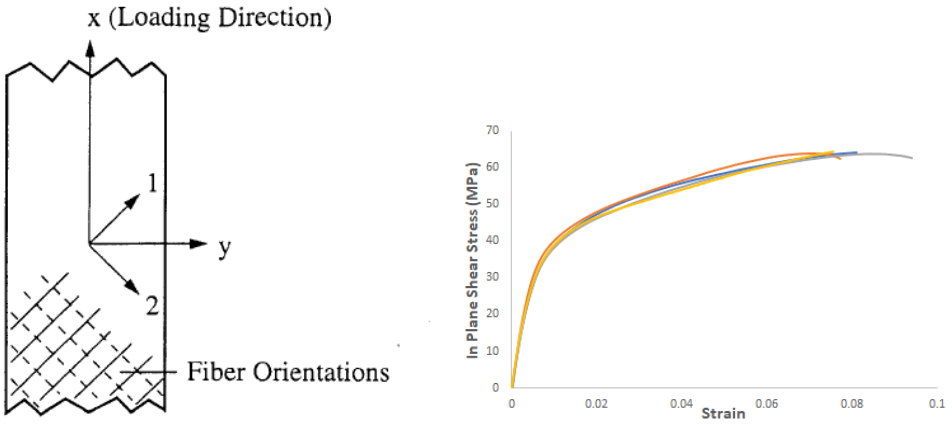

(a) Loading direction and fiber orientations (b) in-plane shear stress-strain curves

Fig. 4.5 (a) Representation of the loading direction and fibers $\pm 45^{\circ}$ orientation during the experiment [3] and (b) in-plane shear stress-strain properties of the CFRP coupons

where τ_{12i} is the shear stress at i^{th} data point in MPa, P is the load at that point in N, and A is the cross sectional area in mm^2 [3]. In-plain shear strain is also calculated using the formula below:

$$\gamma_{12_i} = \varepsilon_{x_i} - \varepsilon_{y_i} \tag{4.6}$$

where γ_{12_i} is the shear strain at i^{th} data point and ε_{x_i} and ε_{y_i} are the longitudinal and lateral normal strains at i^{th} data point, respectively [3]. Shear modulus of elasticity was simply calculated by dividing the shear stress by shear strain in the initial linear part of the experiment, 1500 $\mu\varepsilon$ – 4000 $\mu\varepsilon$ shear strain range. Table 4.3 reports the measured values for in-plane shear strengths and modulus.

Table 4.3 In-plane shear properties of CFRP specimens measured with respect to the ASTM D3518 standard [3].

	Shear Strength (MPa)	Shear Modulus (GPa)
Z2	59	3.3
Z3	60	4.2
Z4	59	3.9
Z5	59	3.4
Average	59	3.7
Std Dev	0.4	0.3

Eventually, compressive properties of the specimens were measured following ASTM D3410 standard test method [4]. Two small HBM® 1-LY48-0.6/120 strain gauges were attached on both sides of the specimens for measuring the strain and calculating the bending percentage during the experiment. Figure 4.6 illustrates the schematic representation of stain gauges positions and an image of the unsupported section of the CFRP coupon being compressed by shear loading alongside the grips.

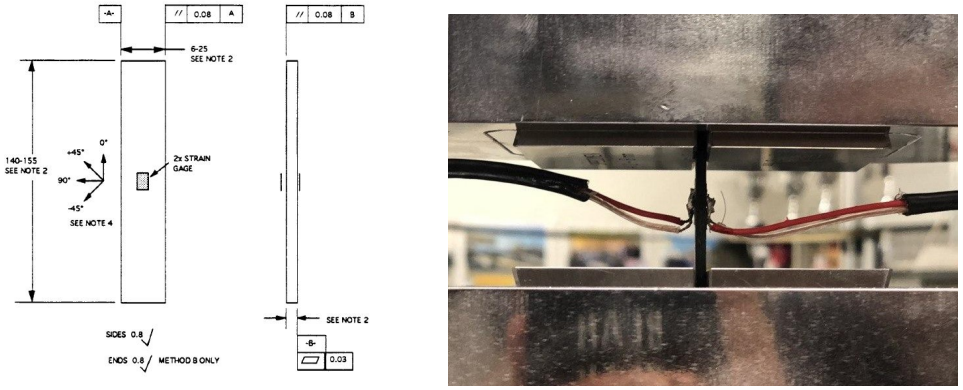

(a) Schematic of the strain gauges positions [4] (b) Compression test using strain gauges

Fig. 4.6 (a) Schematic of the strain gauges positions on the coupon for compressive characterizations according to the ASTM 3410 standard and (b) CFRP coupon under compression with strain gauges attached on both sides.

The coupons had widths of 12.9 *mm* and thicknesses of 2.5 *mm*. Around 20 *mm* of their 150 *mm* overall length was in the unsupported section of the test fixture, Figure 4.6b. That was short enough to ensure avoiding Euler buckling and long enough to guarantee uniaxial compression [4]. HBM® 1-LY48-0.6/120 strain gauges with 6 *mm* carrier length and 120 Ω resistance were installed in their centers. The crosshead was moving downward at the constant rate of 1.5 mm/min until the failure of the specimen.

Stress was simply calculated with diving the force by cross sectional area in each data point ($\frac{F}{A}$) and strain was the average of values acquired from both gauges ($\frac{\varepsilon_1+\varepsilon_2}{2}$). The compressive chord modulus of elasticity was computed in the $1000-3000\ \mu\varepsilon$ range as:

$$E^{chord} = \Delta\sigma/\Delta\varepsilon \tag{4.7}$$

where $\Delta\sigma$ and $\Delta\varepsilon$ are the differences in compressive strength and strain in that range, respectively. The middle point of this range, 2000 $\mu\varepsilon$ was used to assess the bending

percentage using the formula:

$$B_y = \frac{\varepsilon_1 - \varepsilon_2}{\varepsilon_1 + \varepsilon_2} \times 100 \tag{4.8}$$

where B_y is the bending percentage and ε_1 and ε_2 are the gained strains from gauges 1 and 2. Bending percentages of 10% and lower validated the reliability of the obtained results for elastic properties characterizations [4]. The measured values for compressive strength and modulus are reported in Table 4.4.

Table 4.4 Compressive properties of CFRP specimens measured with respect to the ASTM D3410 standard [4].

	Compressive Strength (MPa)	Compressive Modulus (GPa)
C1	307	59.1
C2	330	55.8
C3	338	58.5
Average	325	57.8
Std Dev	13.1	1.5

Successful characterization of compressive properties of the CFRP coupons completed the first block of our approach. Table 4.5 summarizes all of the obtained results in this basic level.

Table 4.5 Mechanical properties of GG 630T-37 carbon fiber laminate [5].

Characterization	Value	Standard
Density	1.56 kg/dm^3	
Tensile Modulus	59.8 (±2.2) *Gpa*	ASTM D3039
Tensile Strength	946 (±37.5) *MPa*	ASTM D3039
Compressive Modulus	57.8 (±1.5) *Gpa*	ASTM D3410
Compressive Strength	325 (±13.1) *MPa*	ASTM D3410
Shear Modulus	3.7 (±0.3) *Gpa*	ASTM D3518
Shear Strength	59 (±0.4) *MPa*	ASTM D3518
Flexural Modulus	70.0 (±2.1) *Gpa*	ASTM D0790
Flexural Strength	624 (±48.1) *MPa*	ASTM D0790
Poisson's Ratio	0.074 (±0.006)	ASTM D3039
Yield Strain	0.017 (±0.001)	ASTM D3039

In the next section, using the new developed fixture explained in the previous chapter, results from different impact experiment trials performed on both glass and carbon fiber reinforced elements are thoroughly discussed.

4.2 Element Level

In order to evaluate the energy absorption of the composite elements, either the test specimens should be self supportive or there must be a fixture to support them from buckling. Manufacturing self supporting elements will cause deviation in their actual mechanical properties from the ones characterized in the previous block. To avoid this critical problem, flat specimens were cut from the same sheets of material used for previous coupon level tests. Solving this problem was essentially important for the simulation procedures.

Using this fixture (Figure 4.7), effects of unsupported lengths, impact speed, and impact mass were studied. In some cases, for preliminary evaluations, only glass fiber samples were tested due to the scarcity of CFRP elements.

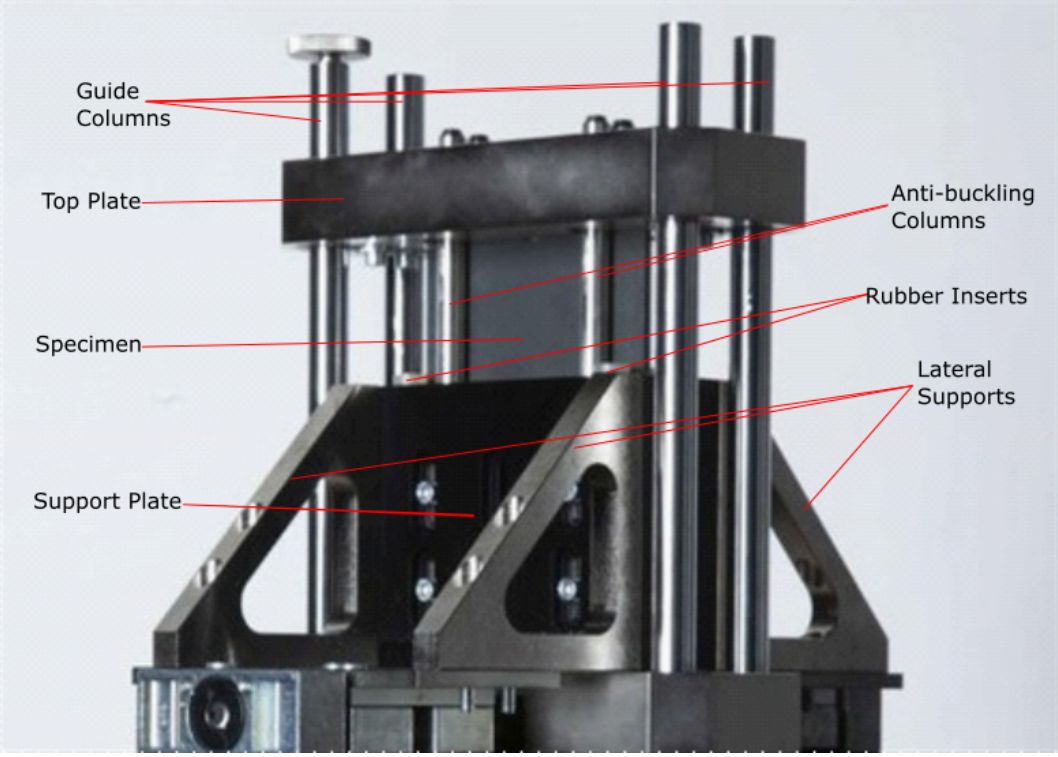

Fig. 4.7 Image of the newly developed fixture with different parts indicated.

4.2.1 Unsupported Length

One of this fixture characteristics is the possibility to adjust the support length by regulating the position of four supporting columns. Researchers have already shown that length of unsupported height affects the energy absorption of composite elements [21, 98]. Therefore, it was necessary to first study these effects in this new fixture as well and then, based on the results, design the next experiments.

For these sets of preliminary evaluations, only GFRP elements were tested. Four different unsupported lengths were studied: 5, 10, 20, and 35 *mm*. Figure 4.8 illustrates the effects of unsupported length on the energy absorption mechanisms of the elements. Too short lengths, 5 *mm*, do not allow the splaying to take place and by over constraining the element mostly fragmentation occurs. On the other side of the spectrum, high unsupported lengths like 35 *mm* cause bending and asymmetrical breakage of the elements. Evaluations with 20 *mm* of unsupported length showed more delamination compared to ones with 10 *mm* of unsupported height.

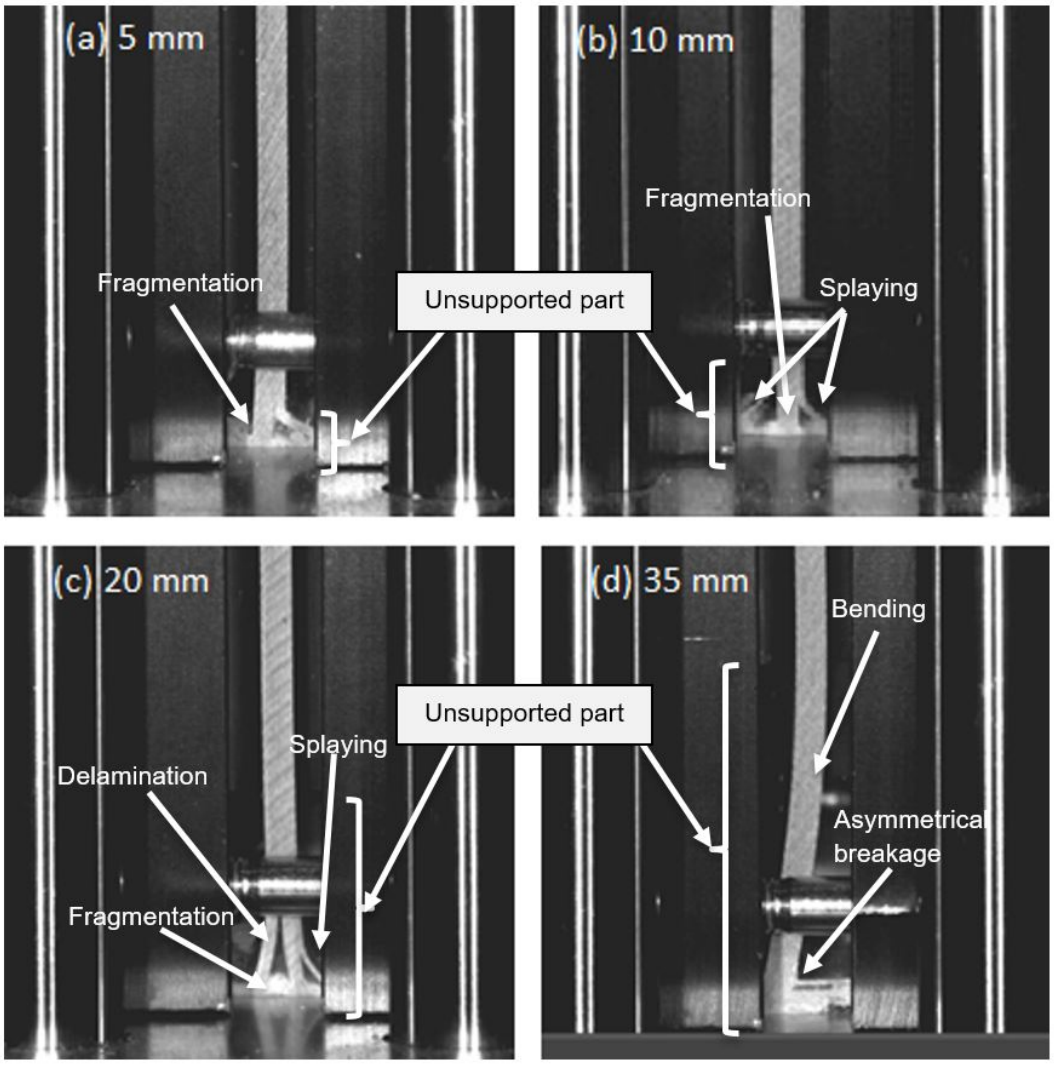

Fig. 4.8 Snapshots of the glass fiber reinforced elements under impact at different unsupported lengths. The higher unsupported heights allow bending and other less resistant fracture mechanisms, such as delamination and asymmetrical breakage, to occur.

The unsupported length also affected the obtained force displacement results, Figure 4.9. Naturally, the first peak was not different since it is related to the impact between the falling cross head and the metallic upper plate. However, it can be noted that higher unsupported lengths cause more oscillations in the force and lower mean force values. It is due to the fact that delamination and bending, main fracture mechanisms in the higher unsupported lengths, are less resistant compared to fragmentation and splaying [21].

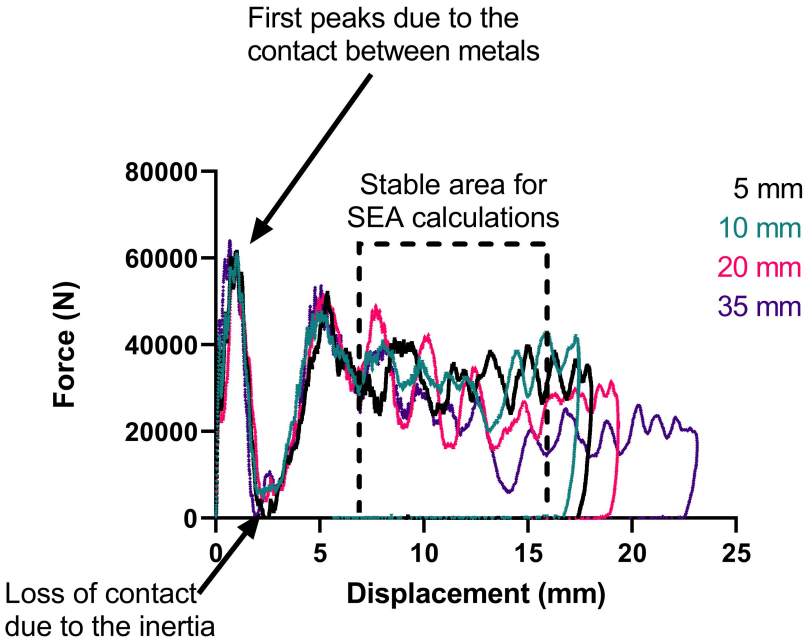

Fig. 4.9 Representative force displacement graphs of GFRP flat elements being impacted. Drop of mean force values by increasing the unsupported height can be seen.

Table 4.6 gives the measured and calculated values for mean forces and SEA at different unsupported lengths. These results were obtained from the more stable area of the results as shown in Figure 4.9. Numerical results in Table 4.6 confirm what was shown in Figure 4.9.

Table 4.6 Mean forces and specific energy absorption values of GFRP elements at different unsupported heights.

Unsupported Height (mm)	Mean Force (kN)	SEA (kJ/kg)
5	32.383 ± 0.76	52.167 ± 0.91
10	31.633 ± 0.77	51.316 ± 0.79
20	30.635 ± 3.81	49.861 ± 5.33
35	22.350 ± 3.85	37.618 ± 6.70

After finding the reliable unsupported length of 10 *mm*, experiments were designed to study the effects of various impact masses and velocities on the energy absorption capabilities of the both GFRP and CFRP flat elements. In the next sections these effects are discussed.

4.2.2 Impact Mass

In the Instron 9450 drop weight tower testing machine used for our impact analysis in the element level, the impact energy is simply provided by converting the potential energy, $U = mgh$, into the kinetic energy, $K = \frac{1}{2}mv^2$. Thus, the impact energy, mass, and speed are dependent on each other.

Therefore, two different sets of experiments were designed. First, impact speed was kept constant and impact mass was changed, so impact energy was changed too. In the second set, impact energy was fixed and impact mass and velocity were varied in each experiment. These tests were performed on both glass fiber and carbon fiber reinforced elements. The results obtained from each of these materials are reported in the next pages.

GFRP Elements

In the first set of experiments on the glass fiber reinforced elements, impact velocity was kept constant at 4.69 m/s and impact mass was increased for each test. In the second set, impact energy remained unchanged at 550 J while impact mass kept changing for each test. Due to the scarcity of the flat elements, two tests were performed under each condition. Figure 4.10 shows force displacement results from these sets of experiments. Only one curve per testing condition is illustrated to keep them comparable and to simplify the interpretation.

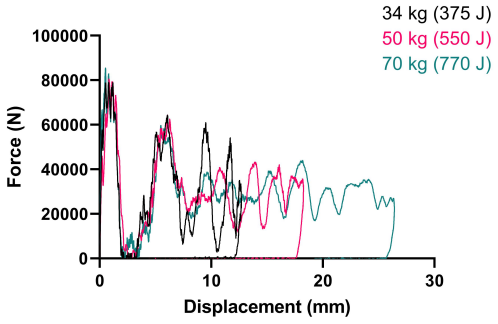

(a) Impact velocity kept constant at 4.69 m/s.

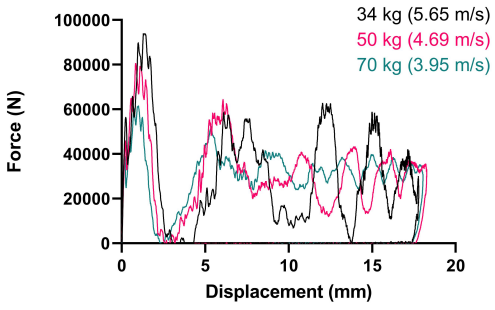

(b) Impact Energy kept constant at 550 J.

Fig. 4.10 Effects of impacting mass on the acquired force displacement data from impact tests on GFRP elements using the newly developed fixture.

Table 4.7 gives the averages of mean forces and standard deviations of the force data for each impact mass. This table concludes the higher oscillations of force data in lower impact masses, which could be figured as well from Figure 4.10. As explained in the methodology chapter, only the more stable section of the data, $40-90\%$ of the total displacement, are used for these calculations. Figure 3.14 in the previous chapter explains these areas.

Table 4.7 Average of mean forces and standard deviations of force for tests on GFRP elements with different impacting masses.

Impact Mass (kg)	Mean Force (kN)	Standard Deviation (kN)	SEA (kJ/kg)
34 kg	30.853 ± 1.76	17.685 ± 2.12	50.892 ± 4.02
50 kg	30.646 ± 2.09	10.044 ± 1.27	50.452 ± 2.54
70 kg	31.296 ± 1.06	5.206 ± 0.65	50.663 ± 1.85

CFRP Elements

Similar sets of experiments were designed for carbon fiber reinforced elements. Tests were carried out at constant impact velocity of 4.69 m/s and different masses and energies. The same trend as for the GFRP elements was observed also in the obtained results from tests on CFRP flat plates. Lower masses caused higher oscillations of force data but did not affect mean force or SEA. Table 4.8 summarizes these results.

Table 4.8 Averages of mean forces and standard deviations of force for tests on CFRP elements with different impacting masses at 4.69 m/s impact velocity.

Impact Mass (kg)	Mean Force (kN)	Standard Deviation (kN)	SEA (kJ/kg)
34 kg	17.330 ± 0.10	9.579 ± 0.37	45.537 ± 1.30
50 kg	18.145 ± 2.11	3.029 ± 1.16	44.976 ± 1.99
70 kg	16.687 ± 1.77	3.007 ± 0.74	45.945 ± 2.96

Figure 4.14 shows three of these samples at the end of experiment. The white lines of the specimens are due to the contact between anti-buckling columns and flat elements while being crushed. As it can be seen, samples are crushed quite symmetrically with the splaying of outer layers. It is observed also here that the 10 *mm* gap

allows the outward curling up of the crushed parts and the newly developed fixture does not intervene with the crushing procedure.

Fig. 4.11 Samples crushed with impact velocity of 4.69 m/s and different impact masses. From left to right impact masses were: 34 kg (375 J), 50 kg (550 J), and 70 kg (770 J).

It was concluded that impact mass does not affect the energy absorption capabilities of the tested elements. Only, due to the differences in inertia between the anti-buckling fixture and falling masses, lower masses lead to higher oscillations in the measured force data. In the next section, impact velocity effects are studied.

4.2.3 Impact Velocity

Similar to the previous section, two sets of experiments were designed to study effects of impact velocity on the energy absorption characteristics of the specimens and also the functionality of anti-buckling fixture. In one set, impact mass was kept constant in each group of the experiments and only impact velocity was changed. In the other one, impact energy was kept constant and impact velocity was varied in each test.

GFRP Elements

For the first set of experiments, impact energy was kept constant at 550 J and impact velocities were changed. Figure 4.12 illustrates these obtained results for tests on NEMA FR4 glass fiber reinforced elements [94]. It summarizes effects of both impact mass and velocity on the acquired data from the newly developed anti-buckling fixture. Higher impact velocities cause greater peak forces and lower impact masses result in more oscillation of the force data.

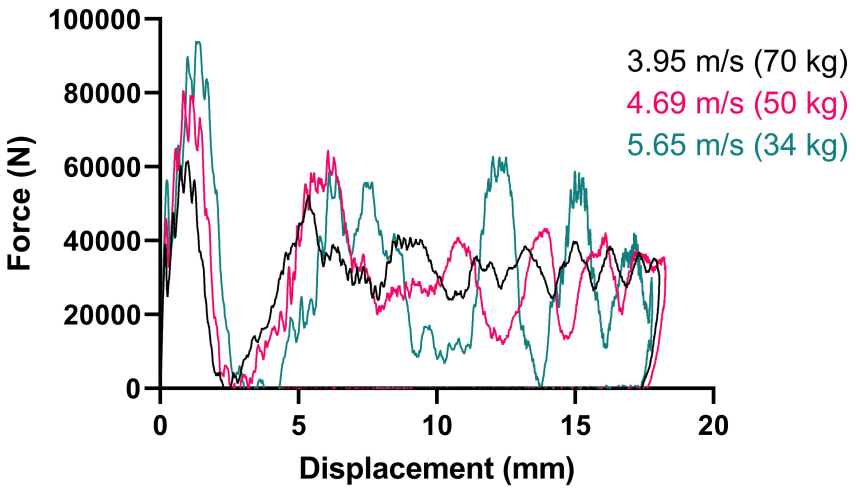

Fig. 4.12 Force displacement results of impacting GFRP flat elements with impact energy of 550 J and different velocities and masses.

Table 4.9 summarizes the obtained results from tests on GFRP plates at different impact velocities. These results suggest that impact velocity, in the studied range of $3.96 - 5.65\ m/s$, does not affect the energy absorption capabilities of the elements.

Table 4.9 Mean force and specific energy absorption of GFRP elements at different velocities.

Impact Velocity (m/s)	Peak Force (kN)	Mean Force (kN)	SEA (kJ/kg)
3.96	62.261 ± 0.77	31.633 ± 0.77	51.316 ± 0.79
4.73	81.873 ± 2.80	30.947 ± 1.89	50.729 ± 3.52
5.65	93.814 ± 0.01	29.951 ± 0.28	50.599 ± 0.68

Mean crush forces sustained by the specimens were close to each other. Only the peak force was increased which is again related to the difference of inertia between impacting mass and metallic upper plate. If this effect is neglected while designing experiments, the load cell limits might be reached and force data acquisition system would be damaged.

CFRP Elements

Figure 4.13 shows some of the obtained results from impact tests on carbon fiber reinforced elements at different velocities. In one set the impact mass was 50 kg and in the other one it was 70 kg. Also here only two tests were performed under each condition and just one of them is depicted to keep the graphs more straightforward.

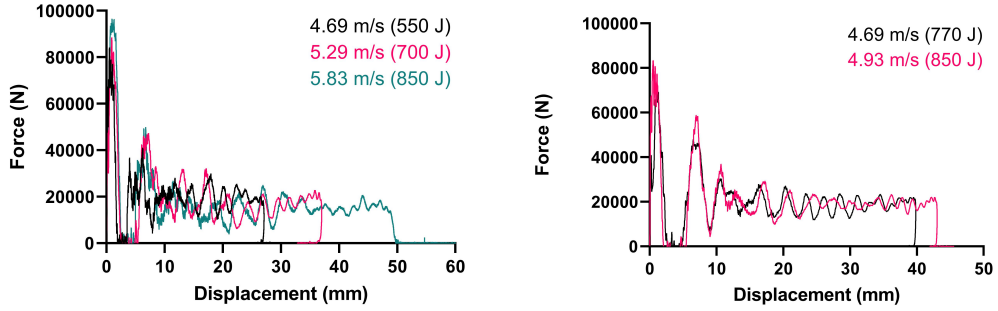

(a) Impact mass: 50 kg

(b) Impact mass: 70 kg

Fig. 4.13 Force displacement results of the impact tests performed on CFRP flat elements at different impact velocities while maintaining the mass at (a) 50 kg, and (b) 70 kg.

Table 4.10 numerically reports the results of impacting saw-tooth triggered CFRP flat plates at different velocities. It can be noted that higher impact velocities caused superior initial peaks. However, the mean forces are similar which indicates that

impact velocity, like impact mass, has no effect on the energy absorption capabilities of the material in the studied range of $4.69 - 5.83\ m/s$.

Table 4.10 Mean force and specific energy absorption of CFRP elements at different velocities.

Impact Velocity (m/s)	Peak Force (kN)	Mean Force (kN)	SEA (kJ/kg)
4.69	77.309 ± 4.38	17.585 ± 1.65	46.208 ± 3.08
5.29	86.286 ± 2.65	17.101 ± 1.85	45.350 ± 2.46
5.83	99.703 ± 3.42	17.108 ± 0.65	45.002 ± 1.83

Figure 4.14 exhibits three crushed CFRP samples. They were crushed under same impact mass of 50 *kg* but different impact velocities (Figure 4.13a). It was observed that by increasing the impact velocity, or energy, the specimen is crushed in a similar manner but for a longer distance. Also here, it is proved again, for these sets of experiments, that 10 *mm* gap of unsupported height is sufficient and elements are crushed without the interference of the newly developed fixture in the outward splaying and curling up of the layers.

Fig. 4.14 Samples crushed under impact mass of 50 *kg* and different velocities. From left to right: 4.69 m/s (550 *J*), 5.29 m/s (700 *J*), and 5.83 m/s (850 *J*).

These results are in accordance with the previously published studies in the literature [44, 60]. Mamalis et al. [104] conclude that SEA is independent of impact velocity as far as energy absorption mechanisms are not changed. In the

range of impact velocities studied in these experiments, $3.96 - 5.83\ m/s$, the failure mechanisms of outer layers splaying and inner layers fragmentation did not change and therefor calculated SEA values were similar for different impact velocities.

Figure 4.15 depicts snapshots of high-speed camera recorded video at four different time intervals. The video was captured with Photron FASTCAM Mini AX high speed camera and analyzed by Photron FASTCAM Viewer software. The saw-tooth triggered flat CFRP element in this test was crushed under impact energy of 850 J, impact mass of 70 kg, and with 4.93 m/s of impact velocity.

From Figure 4.15b, it can be understood that the saw-tooth triggering system is helpful in initiating the crash from the bottom of the plate and in avoiding catastrophic failures of the specimens. Similar results were reported by other researchers as well in the literature [21, 98].

Once the triggered section is completely crushed, stable and progressive crushing of the flat plate starts. During this stage, the impact energy is absorbed by the fragmentation of the inner layers and splaying of the outer ones. Figure 4.15c shows these mechanisms taking place. From the videos, and also observations of the specimens at the end of each test, it was reassured that 10 mm unsupported gap at the bottom of the fixture permits the element to crush progressively.

Figure 4.15d shows the propagation of the large crack which occur as the element keeps crushing. These large cracks result in the vast delamination in the center of the elements which are less favorable for the energy absorption capabilities. The fact that the newly developed fixture makes it possible to observe and investigate these cracks initiation and propagation, provides a great research potential for studying other material systems such as Non Crimp Fabric (NCF) or 3D woven composites were crack propagation should be suppressed.

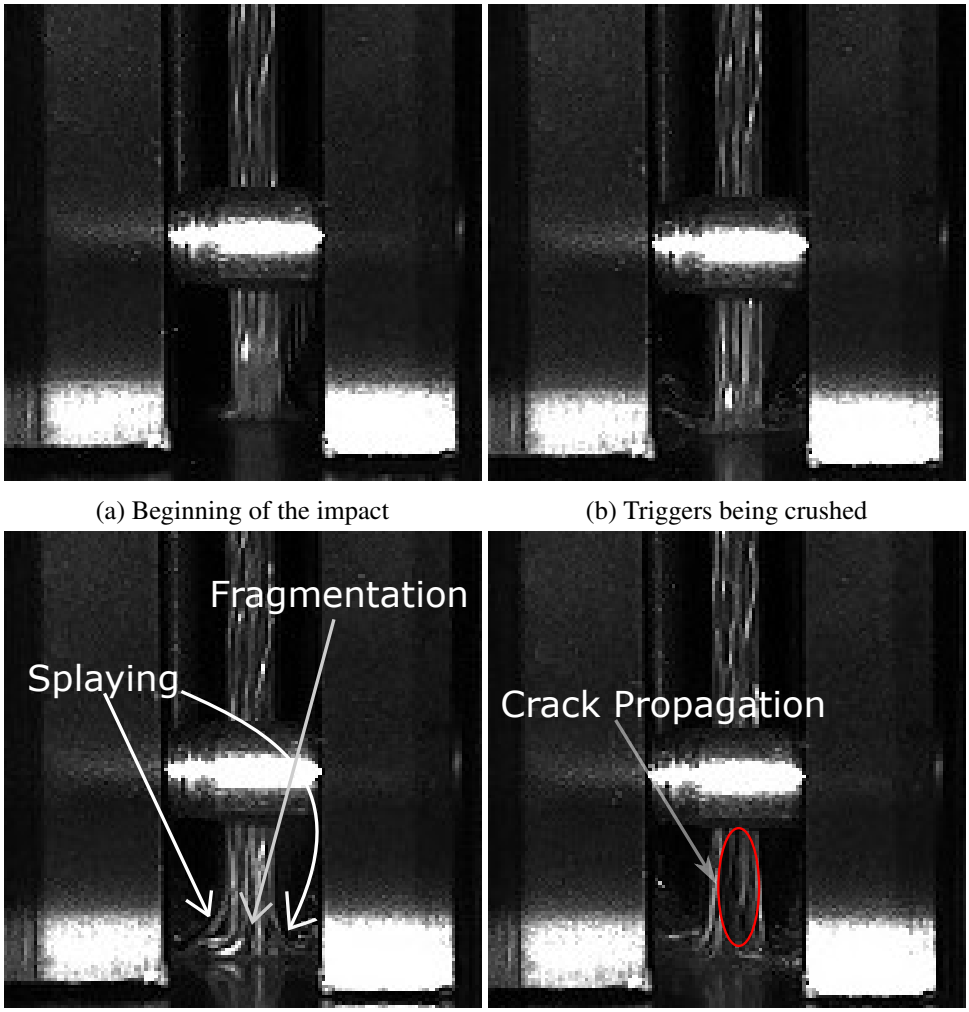

(a) Beginning of the impact (b) Triggers being crushed

(c) Energy absorption mechanisms (d) Crack propagation causing delamination

Fig. 4.15 Snapshots of flat CFRP element while being crushed under impact energy of 850 J, impact mass of 70 kg, and impact velocity of 4.93 m/s. Splaying of the two outer layers and fragmentation of the inner ones were the main energy absorption mechanisms, (c). Large crack propagation which could cause delamination in the middle of the specimen, (d).

Figure 4.16 shows the same specimen of the previous figure at the end of the experiment. The side and top views show the symmetrical crushing of the flat element and prove that it could freely curl outward while crushing. The bottom view image illustrates the delamination in the middle of the element and fragmented parts of the inner layers.

(a) Side view

(b) Top view

(c) Bottom view

Fig. 4.16 Images of CFRP element after being crushed under impact energy of 850 *J* from different angles. Side and top views show the symmetrical crushing of element by not intervening with the newly developed fixture. The bottom view image shows the delamination in the middle of the element and fragmented parts of the inner layers.

The repeatability of the tests and reproducibility of the results proved the newly developed anti-buckling fixture to be reliable. The results from CFRP elements were later used by another PhD candidate, Ravin Garg, for predicting the composite behavior in the component level [105]. By applying parametric optimization, Garg et al. tuned the related material card in Radioss and increased the efficiency of development process by substituting the trial-and-error approach [105].

4.3 Component Level

The last level in our building block approach was component level. Six Formula SAE crash attenuators were manufactured for this purpose. These experiments were designed to work as the proof of concept for the experimental and numerical crashworthiness research activities inside ICONIC [1]network. The first two tests in the component level were performed under quasi-static conditions to understand the effectiveness of the attenuator design. Afterwards, four dynamic tests were performed on the remaining demonstrators. Results and images are reported in the following pages.

4.3.1 Quasi-Static Tests

In order to satisfy the requirements for quasi-static conditions, tests were performed at the constant speed of 10 mm/min. Since total height of the component was 216 mm, this speed resulted in strain rates lower than 0.13 per minute throughout the test procedure. At the very beginning it was 0.045 $/min$, which reached 0.13 $/min$ towards the ends, due to the shorter heights of the remaining uncrushed sections.

Figure 4.17 shows an image of the second quasi-static test using ZwickRoell® electromechanical testing machine at DYNLAB laboratory[2] in Politecnico di Torino. Steady crushing of the component from the top and removal of the crushed parts confirmed the functionality of the triggered design. This was reported by Boria et al. for the frontal crash structure made with with similar design but different materials

[1]Improving the crashworthiness of composite transportation structures https://blog.qub.ac.uk/wordpress/iconic/

[2]https://www.polito.it/ricerca/infrastrutture/dynlab4jmat/

[103]. Inward and outward buckling of lateral sides were observed as the test moved forwards.

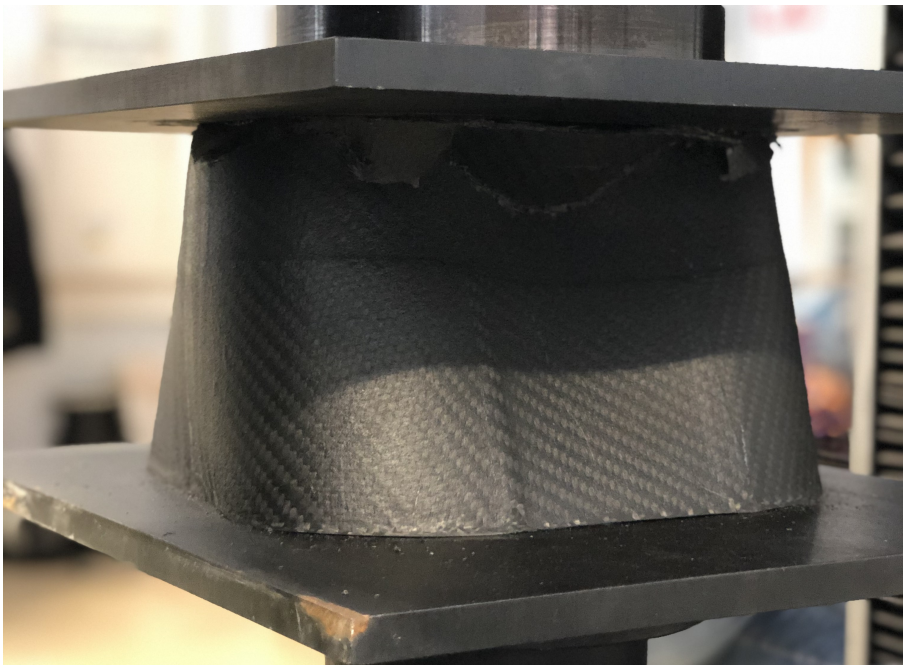

Fig. 4.17 CFRP Formula SAE crash attenuator under quasi-static compression with Zwick-Roell electromechanical testing machine at 10 mm/min speed.

Figure 4.18 reports the acquired load displacement data from electromechanical testing apparatus. Two vertical red dashed lines in the Figure 4.18 indicate the areas where thickness of the sections (number of the plies) changes. These areas were schematically illustrated in Figure 3.18 in the previous chapter. It can be noticed that close to these displacements where the thickness changes, there is a local increase in the obtained force data. This could be due to the higher resistance of the crack initiations in the thicker section. Once they are initiated, their propagation continues with the similar increasing pattern.

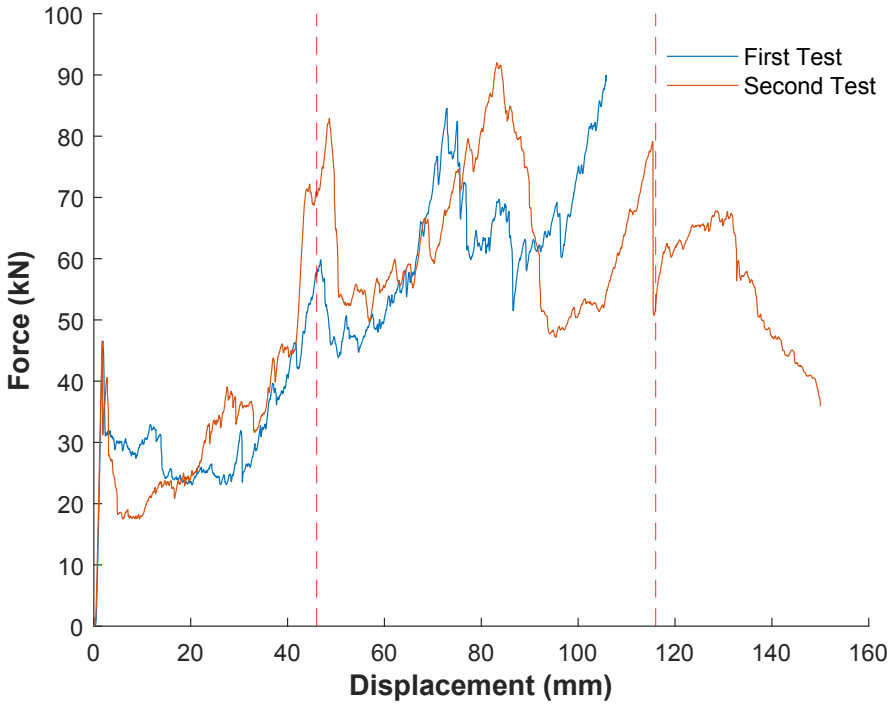

Fig. 4.18 Force displacement results obtained from crushing CFRP crash attenuator at the speed of 10 mm/min. Red dashed lines indicate sections with different thicknesses.

The conical design of these components, Figure 3.18b, meant that the cross sectional area increased by further displacement of the crushing plate. Using the cross sectional view of the SolidWorks software and measuring the surface area at different intersects, Figure 4.19, the relation between the height and cross sectional area was calculated.

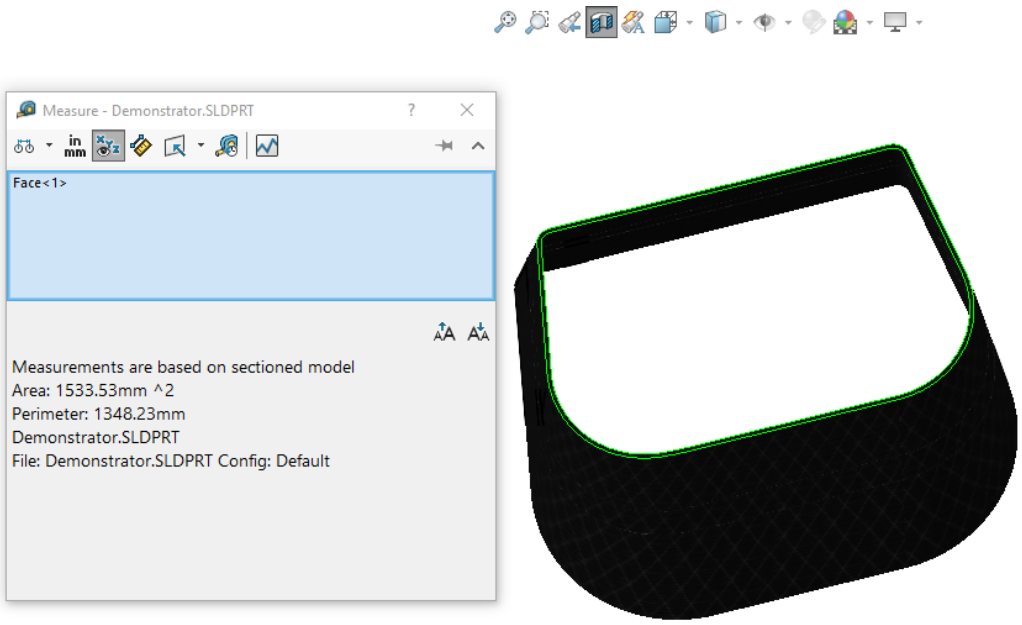

Fig. 4.19 Cross sectional surface area measurement of the CFRP component at different intersections using the SolidWorks software.

Figure 4.20 illustrates the gradual increase of the cross sectional area in these three sections of the component with various thicknesses. Stress displacement results were calculated by using these relationships between the displacement and surface area of the component.

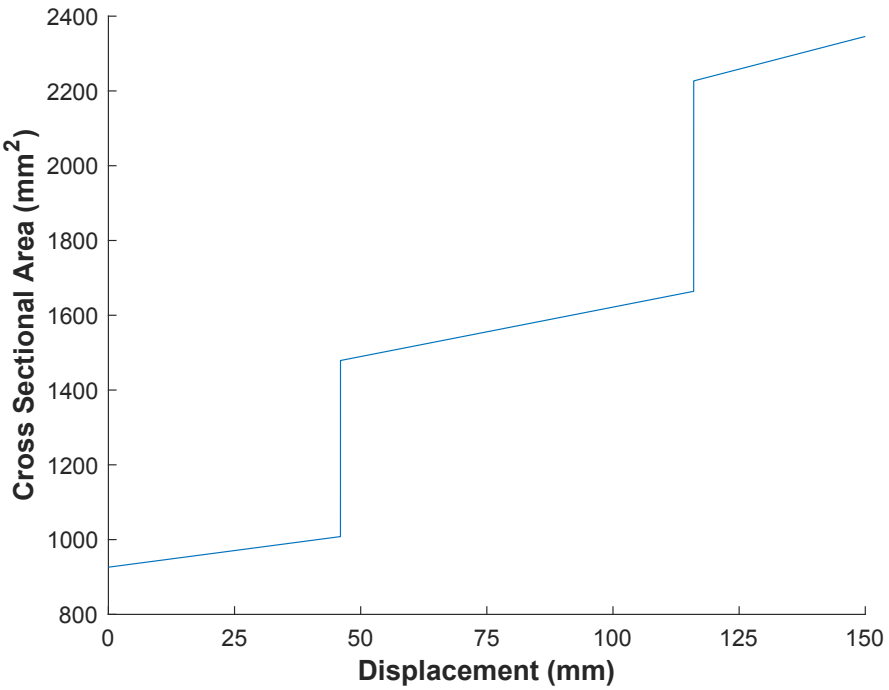

Fig. 4.20 Cross sectional surface area versus displacement from the top of CFRP Formula SAE crash attenuator.

Figure 4.21 depicts the stress versus displacement for these two tests under quasi-static conditions. As it can be noticed from the graphs, local peaks close the dashed lines still exist. As mentioned earlier, one possible reason could be that sections with different thicknesses stop the crack propagation and some extra force (stress) is required to either transfer these cracks to the new sections or initiate new ones.

Comparing Figures 4.21 and 4.18, it can be observed that stress values do not increase as steep as force ones. The average force values in the first section are 30 *kN* and 32 *kN* for tests 1 and 2, respectively. These values are 62 *kN* and 64 *kN* in the middle section with three layers of CFRP material. On the other hand, average stress values in these sections are 32 *MPa* and 40 *MPa* for both tests which numerically confirms what was visually observed comparing the graphs.

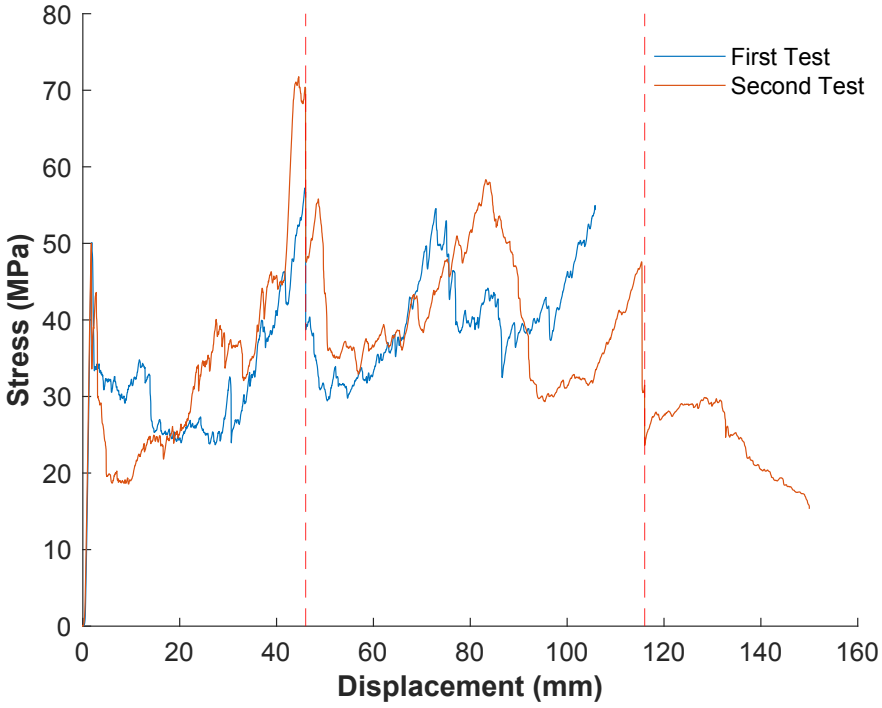

Fig. 4.21 Stress displacement results obtained from crushing CFRP crash attenuator at the constant speed of 10 mm/min. Red dashed lines indicate sections with different thicknesses.

Similar to the element level tests, Equation 2.3 was used to calculate specific energy absorption of the components and compare them with the previously calculated values for flat specimens. Table 4.11 gives the results for both tests. These values are lower than the average SEA of the element level experiments. Also, comparing the average stress values with the ones calculated for the element level experiments, 72.933 ± 5.12 MPa, is another confirmation that bulky breakage of the component parts does not allow the attenuator to absorb energies up to its full potentials.

Table 4.11 Specific energy absorption and average stress for CFRP components under quasi-static compression.

	SEA (kJ/kg)	Average Stress (MPa)
Test 1	27.367	36.397
Test 2	28.211	37.639

These two tests helped to assess the trigger usefulness and understand the fracture and energy absorption mechanisms that the specimen experiences under compression.

Fig. 4.22 Crushed CFRP components after quasi-static tests performed at 10 mm/min rate.

Figure 4.22 illustrates the two crushed components after the test is finished. Visual investigation at the end of experiments showed the crushing of specimen at the curves and side walls. However, bulky breakage of the front and back walls showed that the attenuator has not fully exploited the material energy absorption capabilities.

4.3.2 Dynamic Tests

The first two tests were performed at 7.10 m/s impact speed and 7561 J impact energy. These values were chosen based on the previous knowledge and experience with the similar experiments. After each test, the remaining length was measured and high speed camera videos were observed to check for any irregularities. Then, the impact energy was increased around 20 and 25 percent for the third and fourth tests respectively. Table 4.12 summarizes these conditions.

Table 4.12 Dynamic tests conditions with the impact mass of 300 kg.

	Impact Velocity (m/s)	Impact Energy (J)
Test 1	7.10	7561
Test 2	7.10	7561
Test 3	7.77	9055
Test 4	8.04	9696

MMF KD38V piezoelectric accelerometer [3] with compression design and $+5000/-1000$ g range was used to obtain the force versus time data. Figure 4.23 shows the raw data with 50 kHz acquisition frequency during the first impact test.

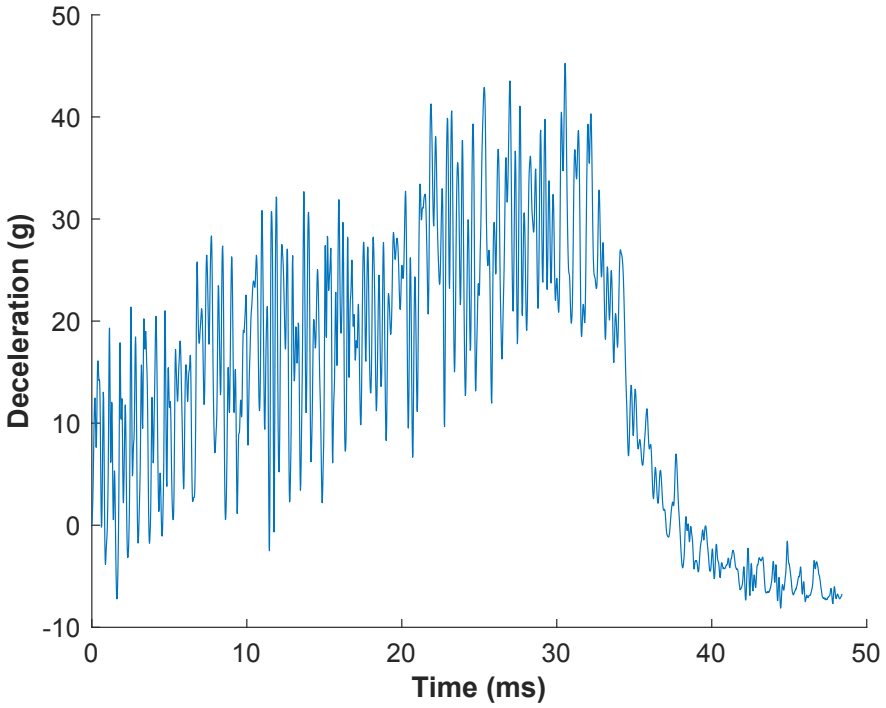

Fig. 4.23 Deceleration (g) versus time (ms) obtained from a piezoelectric accelerometer with 50 kHz data acquisition frequency.

High oscillation of data due to the high sampling frequency must be filtered out. One way to do it, as recommended by ISO 6487 [106] and SAE J211/1_201403 [107] standards regarding the instrumentation for impacts tests of road vehicles, is to apply Channel Frequency Class (CFC) filters. Equation 4.9 shows the general formula of CFC filters [107]:

$$Y[t] = a_0X[t] + a_1X[t-1] + a_2X[t-2] + b_1Y[t-1] + b_2Y[t-2] \tag{4.9}$$

where $X[t]$ is the input data and $Y[t]$ is the filtered data. The other constants are calculated as below:

$$w_d = 2 * \pi * CFC * 2.0755$$

[3] Metra Mess- und Frequenztechnik in Radebeul, Germnay
https://www.mmf.de/english.htm

$$
\begin{aligned}
w_a &= \sin(w_d * T/2)/\cos(w_d * T/2) \\
a_0 &= {w_a}^2/(1.0+\sqrt{2}*w_a+{w_a}^2) \\
a_1 &= 2*a_0 \\
a_2 &= a_0 \\
b_1 &= -2*({w_a}^2-1)/(1.0+\sqrt{2}*w_a+{w_a}^2) \\
b_2 &= (1.0-\sqrt{2}*w_a-{w_a}^2)/(1.0+\sqrt{2}*w_a+{w_a}^2)
\end{aligned}
$$

where T is the sampling frequency and CFC is the filter that is being used. For example if CFC 60 is being applied, CFC equals 60 in the equation to calculate w_d. Figure 4.24 shows filtered data using three different CFC filters.

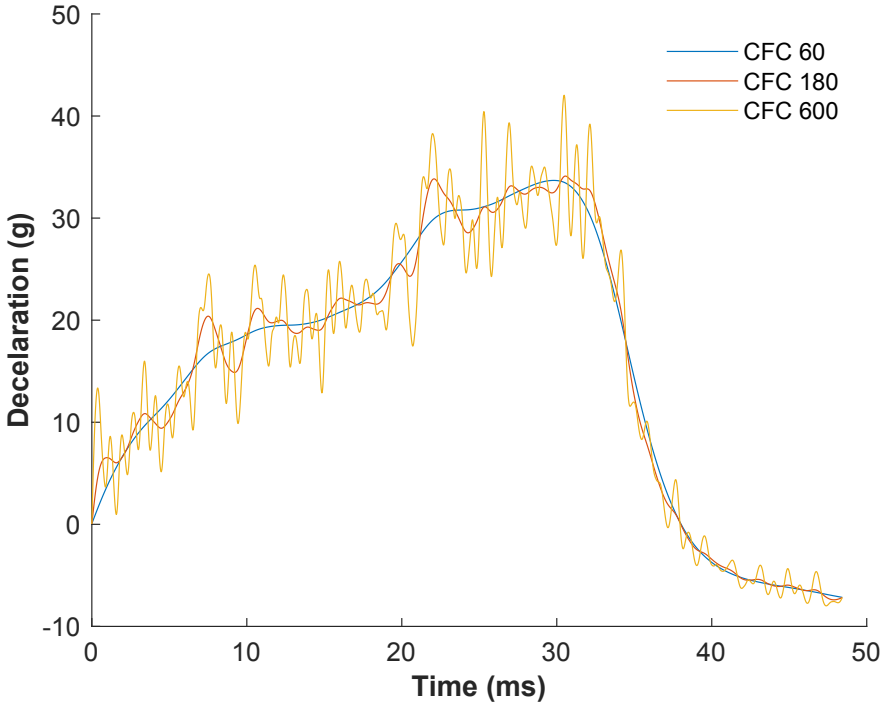

Fig. 4.24 Differences between various CFC filters on the raw deceleration (g) versus time (ms) data.

As it can be noticed, CFC 60 filter provides the smoothest filtered data and gradually increases the force, but it misses to capture the initial peak. On the other hand, CFC 600 filter manages to restore the initial peak forces at the very beginning of the tests, but the final results have higher oscillation.

The other data acquisition equipment was a high speed camera recording the impact at the 1000 frames per second rate. Photron[4] FASTCAM Analysis software

[4]https://www.photron.com/

(PFV) was used to tack the movements of the falling mass and measure the displacement versus time. Figure 4.25 illustrates series of images from the high speed camera during the impact.

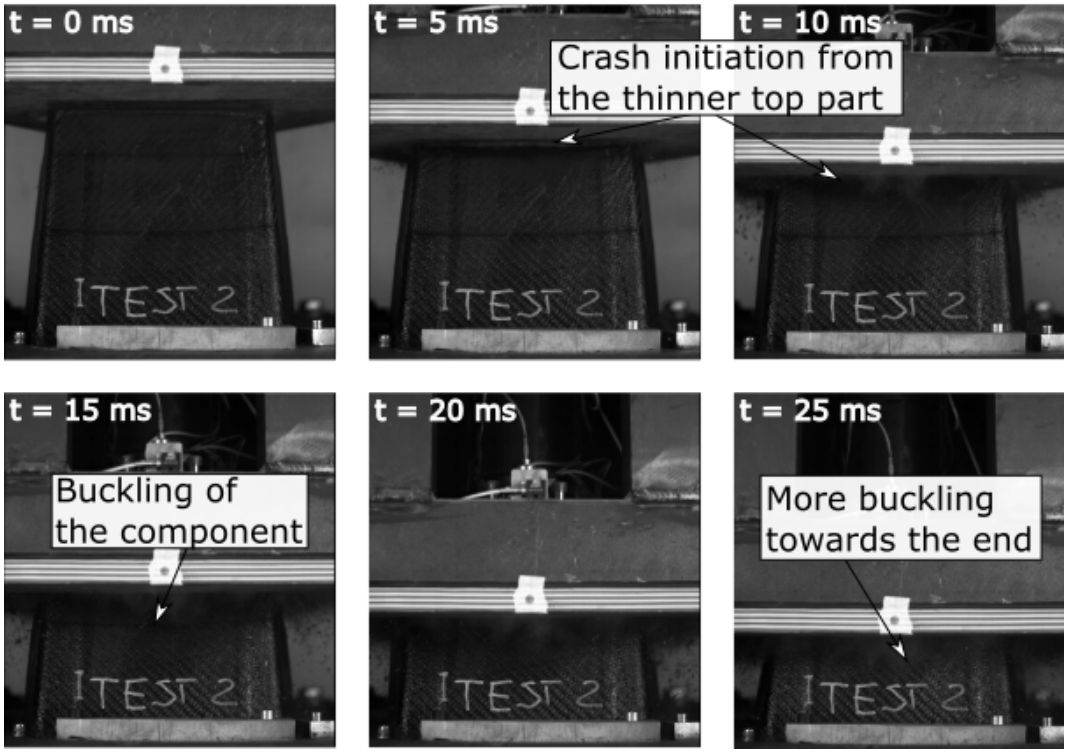

Fig. 4.25 Formula SAE crash attenuator crushing under the impact energy of 7561 J, velocity of 7.10 m/s, and mass of 300 kg.

With the application of these devices, force displacement data for each test was captured, calculated, and verified by comparing with the high speed camera videos. Figure 4.26 shows force displacement data for all these four dynamic tests. The initial peaks are similar for all four tests. In the case of the third test, with 7.77 m/s impact velocity and 9055 J energy, the higher resistive forces exhibited by the component have caused the test to have a final displacements similar to the previous ones. On the other hand, for the last experiment with 8.04 m/s impact velocity and 9696 J energy, no excessive resistive forces were observed and higher final displacement was reached.

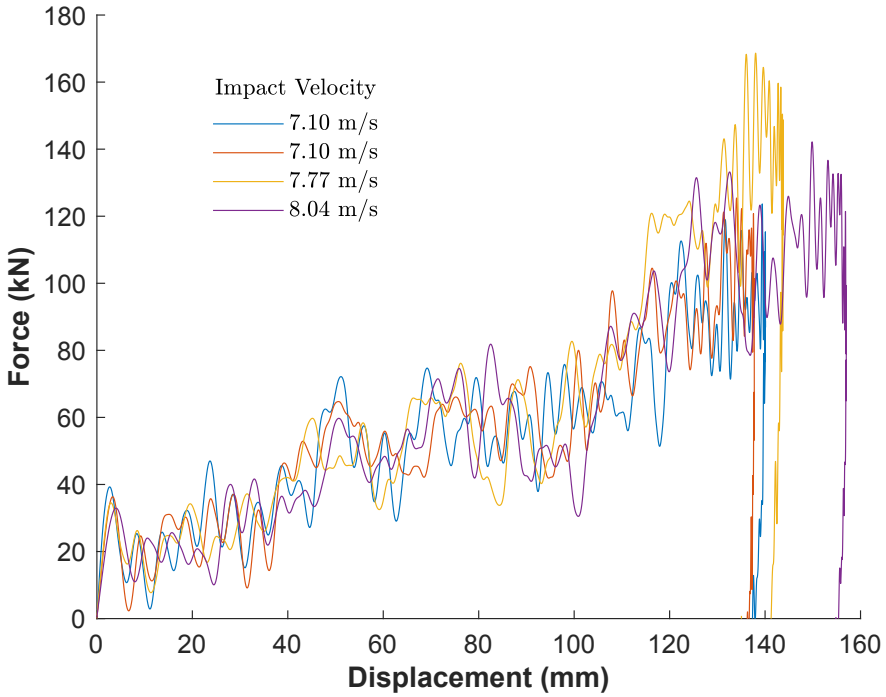

Fig. 4.26 Force displacement results for dynamic tests of CFRP crash attenuators with impact mass of 300 kg and different velocities.

Similar to the quasi-static results, Table 4.13 gives the SEA and average stress values calculated for dynamic tests. The SEA values were calculated from 10 to 120 *mm* of the displacement, similar to the calculations in the element level.

Table 4.13 Specific energy absorption and average stress for CFRP components under quasi-static compression.

	SEA (kJ/kg)	Average Stress (MPa)
Test 1	24.930	33.830
Test 2	23.755	34.034
Test 3	22.438	35.600
Test 4	23.988	36.574

Figure 4.27 shows one of the crash attenuators after being crushed under impact. Other specimens looked similar at the end of experiments. Comparison of Figures 4.27 and 4.22, crushed components after quasi-static tests, can explain the similarities

between SEA and average stress values reported in Tables 4.11 and 4.13, for quasi-static and dynamic tests, respectively. In both cases, force concentrations in the corners leading to the rupture and breakage of the component parts blocked them from reaching the values calculated during the element level evaluations. Similar results and failure modes due to the stress concentration was reported earlier in the literature [22].

Fig. 4.27 Crushed CFRP component after impact with mass 300 kg and velocity 7.77 m/s.

It should be mentioned again that these tests were performed as a proof of concept studies and final validation of the computational methodology for the research activities done inside ICONIC network. Specifically Ravin Garg, PhD candidate in PoliTo, has worked on predicting composite component characteristics under impact. Figure 4.28 shows one of his results comparing the final crushed components from simulation and experiment [105].

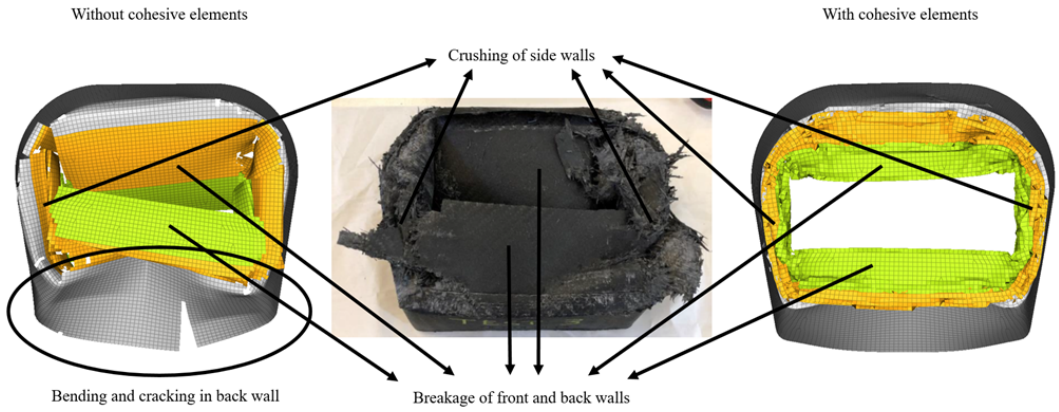

Fig. 4.28 Comparison between the final damages of experimental impact tests on CFRP components and their simulations [105].

Figure 4.29 illustrates force displacement results for all these six experiments under both quasi-static and dynamic conditions. As discussed in the previous paragraphs, the attenuators crush in the same way which can perfectly explain the similarity in the force displacement results of the quasi-static and dynamic tests.

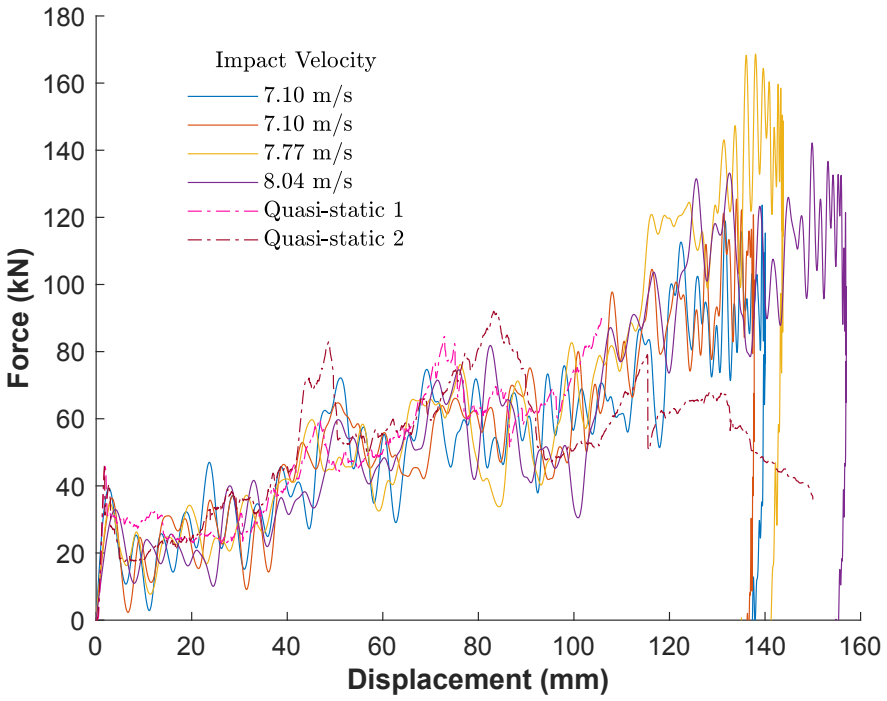

Fig. 4.29 Force displacement results for all the tests in component level.

Chapter 5

Conclusions and Further Research

First, standard mechanical characterization tests on coupons were performed for the basic level of the building block approach. For the second level, flat rectangular elements were chosen for in-plane impact analysis and crashworthiness evaluations. Since they tend to buckle and fail catastrophically, a new anti-buckling fixture was designed and manufactured to sustain the flat elements while being crushed.

Results from the coupon level characterizations provided the necessary input for the numerical simulations of the fixture design. The fixture was specifically designed to be incorporated with the drop tower testing machines. This helped to benefit from the properly elaborated sensors and other data acquisition facilities used for the well known and consolidated characterizations such as drop dart tests.

The adjustable support height feature of the fixture, helped us to study the effect of unsupported height on the crashworthiness and fracture mechanisms of the composite elements. It was shown that the higher free length at the bottom part of the specimen caused more buckling and delamination and lower specific energy absorption values. Unsupported length of 10 mm showed the best combination of supporting the specimen from buckling while crushing and allowing the various fracture mechanisms to take place.

Later, effects of impact velocity and mass were studied as well. It was observed that in the studied ranges of $3.96-5.83$ m/s of velocity and $34-70$ kg of mass, crashworthiness was not changed. The main reason is that in these ranges fracture mechanisms remained the same. Only the first peak force and the oscillations of the acquired force data varied. These were due to the changes in the inertia of the

falling mass and impacting the 30 *mm* thick metallic upper plate at the top of the flat specimen.

All tests performed on GFRP and CFRP specimens proved the fixture :

- To be able to initiate progressive stable crush without affecting the failure modes of the elements.
- To allow testing various thicknesses of specimens, up to 16 *mm* with crushable lengths of up to 50 *mm*.
- To avoid specimen tearing because of the cylindrical shapes of the supporting columns.
- To permit using the same dimension for specimens as in other standards like ASTM D7137 and D7136 for composite plates characterizations.

The obtained results prove that using a 30 *mm* thick metallic upper plate is useful in transferring the impact energy to the flat specimen and forcing it to crush from the bottom part. However, it causes unrealistically high force peaks in the force-displacement curves which have nothing to do with the tested material. In this research study only the stable part of the force data, $40\% - 90\%$ of the final displacement, was used to avoid these unrealistic peaks and their possible effects on the SEA and mean crush force calculations.

Another possible solution could be eliminating this thick metallic upper plate and impacting the specimen directly. Figures 3.15 and 3.16 illustrate the falling disk impactor and preliminary outcomes obtained from that. Even though these results look potentially promising, 50% of the specimens failed from the upper part which is not wanted and encourages further modifications in the future. This is an ongoing research activity being pursued by Lorenzo Vigna, a PhD student in Politecnico di Torino.

As it was reported in the second chapter, researchers report the SEA of composite materials under static and dynamic conditions. During this study only the dynamic impact tests were performed on the flat elements. Preliminary attempts to use this fixture for the quasi-static characterization were not successful due to the failure of the elements from the upper parts. Therefore, further modifications of the fixture are necessary to achieve reliable quasi-static characterization results.

Finally, for the component level of the BBA, 6 crash demonstrators were manufactured and tested. It was observed that different CFC filters have incompatible

effects on the raw data from dynamic impact tests. Some make the data smoother but miss the initial peaks, while others capture the initial peaks but still end up with oscillations in the data. Since the area under the force-displacement data for different filters does not differ, they are all fine for the SEA calculations. However, non of them alone can perfectly illustrate the actual data for the comparison and represent the whole impact experiment.

One solution could be using various filters in different sections of the force versus displacement curves. Figure 5.1 gives an example of this solution. At the beginning section CFC 600 filter is applied to capture the initial peaks. Then, in the middle section raw data is filtered with CFC 180 and in the final section CFC 60 is used. These section were chosen based on an arbitrary decision and after comparing the different combinations. Having a more specific and standardized way in the future could provide more solid solutions.

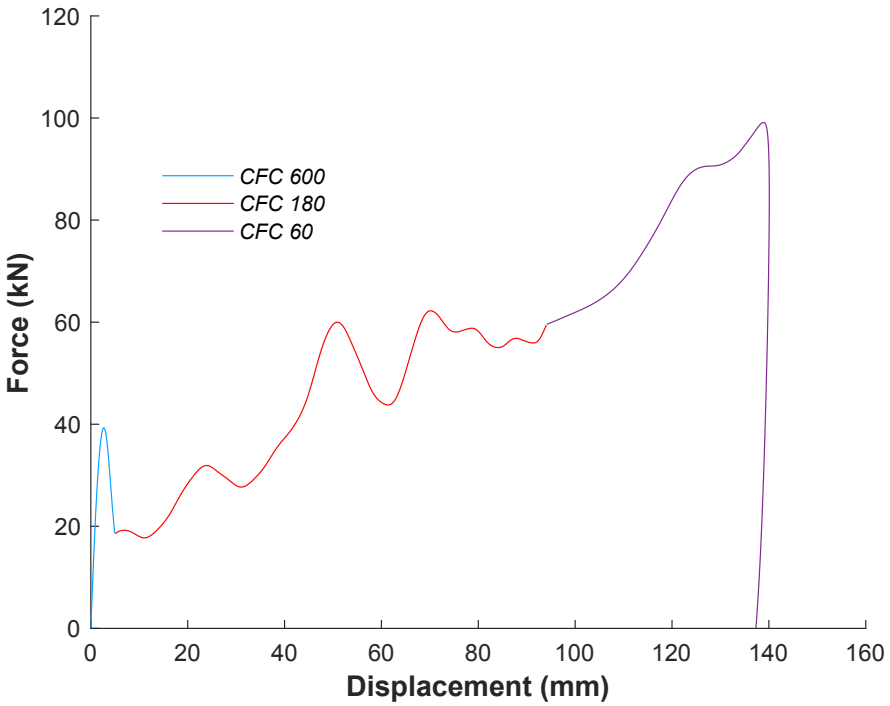

Fig. 5.1 Transverse and lateral strains during tensile characterization of CFRP coupons used for calculations of Poisson's ratio.

These results were used as a proof of concept for the validation of the numerical simulations performed in a companion PhD research performed by Ravin Garg. The characterizations in the coupon block provided the input data for the material cards and model definition. Then, results from the element block were used for the optimization and refining of the model. Finally, the whole process was validated in comparison with the experimental data of the component level.

References

[1] S. Ramakrishna, H. Hamada, Z. Maekawa, and H. Sato. Energy absorption behavior of carbon-fiber-reinforced thermoplastic composite tubes. *Journal of Thermoplastic Composite Materials*, 8(3):323–344, 1995.

[2] ASTM D790-17, Standard Test Methods for Flexural Properties of Unreinforced and Reinforced Plastics and Electrical Insulating . Standard, ASTM International, West Conshohocken, PA, 2017.

[3] ASTM D3518 / D3518M-13, Standard Test Method for In-Plane Shear Response of Polymer Matrix Composite Materials by Tensile Test of a ±45° Laminate. Standard, ASTM International, West Conshohocken, PA, 2013.

[4] ASTM D3410 / D3410M-16, Standard Test Method for Compressive Properties of Polymer Matrix Composite Materials with Unsupported Gage Section by Shear Loading. Standard, ASTM International, West Conshohocken, PA, 2016.

[5] *GG 630 T » Microtex Composites*. Available at https://microtexcomposites.com/en/p/gg-630-t/, (accessed 2020-07-20).

[6] P.W. Huber and R.E. Litan. *The Liability Maze: The Impact of Liability Law on Safety and Innovation*. Brookings Institution Press, 2010.

[7] CMH-17. Composite materials handbook, volume 3 - polymer matrix composites: Materials usage, design and analysis, 2012.

[8] Dirk H.-J.A. Lukaszewicz. Automotive composite structures for crashworthiness. In Ahmed Elmarakbi, editor, *Advanced Composite Materials for Automotive Applications*, chapter 5, pages 99–127. John Wiley & Sons, Ltd, 2013.

[9] Y. Okitsu and N. Tsuji. Nanostructured steel for automotive body structures. In Jason Rowe, editor, *Advanced Materials in Automotive Engineering*, chapter 4, pages 57 – 84. Woodhead Publishing, 2012.

[10] George Jacob, John F Fellers, Srdan Simunovic, and J Michael Starbuck. Energy absorption in polymer composite materials for automotive crash worthiness. Master's thesis, University of Tennessee, Knoxville, 2001.

[11] P.H. Thornton. Energy absorption in composite structures. *Journal of Composite Materials*, 13(3):247–262, 1979.

[12] Gary L. Farley. Energy absorption of composite materials. *Journal of Composite Materials*, 17(3):267–279, 1983.

[13] D. Hull. A unified approach to progressive crushing of fibre-reinforced composite tubes. *Composites Science and Technology*, 40(4):377 – 421, 1991.

[14] Gary L Farley and Robert M Jones. *Energy-absorption capability of composite tubes and beams*. PhD thesis, Virginia Polytechnic Inst. and State Univ. Blacksburg, United States, 9 1989. Nasa Report: NASA TM-101634.

[15] Simonetta Boria and Giovanni Belingardi. Numerical investigation of energy absorbers in composite materials for automotive applications. *International Journal of Crashworthiness*, 17(4):345–356, 2012.

[16] Kyle Indermuehle, Graham Barnes, Stuart Nixon, and Marc Schrank. Simulating composites crush and crash events using abaqus. In *50th AIAA/ASME/ASCE/AHS/ASC Structures, Structural Dynamics, and Materials Conference 17th AIAA/ASME/AHS Adaptive Structures Conference 11th AIAA No*, page 2551, 2009.

[17] Marc A Courteau. Investigating the crashworthiness characteristics of carbon fiber/epoxy tubes. Master's thesis, The University of Utah, Salt Lake City, UT 84112, USA, 2011.

[18] J. J. Carruthers, A. P. Kettle, and A. M. Robinson. Energy Absorption Capability and Crashworthiness of Composite Material Structures: A Review. *Applied Mechanics Reviews*, 51(10):635–649, 10 1998.

[19] Chiara Bisagni. Experimental investigation of the collapse modes and energy absorption characteristics of composite tubes. *International Journal of Crashworthiness*, 14(4):365–378, 2009.

[20] E. Mahdi and T.A. Sebaey. An experimental investigation into crushing behavior of radially stiffened gfrp composite tubes. *Thin-Walled Structures*, 76:8 – 13, 2014.

[21] Bonnie Wade. *Capturing the energy absorbing mechanisms of composite structures under crash loading*. PhD thesis, University of Washington, 2014.

[22] P.H. Thornton and P.J. Edwards. Energy absorption in composite tubes. *Journal of Composite Materials*, 16(6):521–545, 1982.

[23] Gary L Farley and Robert M Jones. Crushing characteristics of continuous fiber-reinforced composite tubes. *Journal of composite Materials*, 26(1):37–50, 1992.

[24] G. Schinner, J. Brandt, and H. Richter. Recycling carbon-fiber-reinforced thermoplastic composites. *Journal of Thermoplastic Composite Materials*, 9(3):239–245, 1996.

[25] H. Hamada, J.C. Coppola, D. Hull, Z. Maekawa, and H. Sato. Comparison of energy absorption of carbon/epoxy and carbon/peek composite tubes. *Composites*, 23(4):245 – 252, 1992.

[26] H. Hamada and S. Ramakrishna. Effect of fiber material on the energy absorption behavior of thermoplastic composite tubes. *Journal of Thermoplastic Composite Materials*, 9(3):259–279, 1996.

[27] S. Boria, A. Scattina, and G. Belingardi. Experimental evaluation of a fully recyclable thermoplastic composite. *Composite Structures*, 140:21 – 35, 2016.

[28] Hongyong Jiang, Yiru Ren, Binhua Gao, and Jinwu Xiang. Numerical investigation on links between the stacking sequence and energy absorption characteristics of fabric and unidirectional composite sinusoidal plate. *Composite Structures*, 171:382 – 402, 2017.

[29] Gary L. Farley. Effect of specimen geometry on the energy absorption capability of composite materials. *Journal of Composite Materials*, 20(4):390–400, 1986.

[30] E. Mahdi, A.S.M. Hamouda, A.S. Mokhtar, and D.L. Majid. Many aspects to improve damage tolerance of collapsible composite energy absorber devices. *Composite Structures*, 67(2):175 – 187, 2005. US Air Force Workshop Damage Assessment of Composite Structures.

[31] Yifan Wang, Jiusheng Feng, Jianghao Wu, and Dayong Hu. Effects of fiber orientation and wall thickness on energy absorption characteristics of carbon-reinforced composite tubes under different loading conditions. *Composite Structures*, 153:356 – 368, 2016.

[32] Mou Haolei, Xie Jiang, Zou Jun, and Feng Zhenyu. Experimental researches on failure and energy absorption of composite laminated thin-walled structures. *Journal of Composite Materials*, 54(27):4253–4268, 2020.

[33] Ali Rabiee and Hessammaddin Ghasemnejad. Progressive crushing of polymer matrix composite tubular structures. *Open Journal of Composite Materials*, 7(1):14–48, 2017.

[34] S. Cauchi Savona and P.J. Hogg. Effect of fracture toughness properties on the crushing of flat composite plates. *Composites Science and Technology*, 66(13):2317 – 2328, 2006.

[35] Masahito Ueda, Shunsuke Anzai, and Takanori Kubo. Progressive crushing of a unidirectional cfrp plate with v-shaped trigger. *Advanced Composite Materials*, 24(1):85–95, 2015.

[36] Yan Ma, Shanshan Jin, and Songlin Zhang. Effect of trigger on crashworthiness of unidirectional carbon fibre reinforced polyamide 6 composites. *Plastics, Rubber and Composites*, 47(5):208–220, 2018.

[37] Damien Guillon, Samuel Rivallant, Jean-Jacques Barrau, Caroline Petiot, Pascal Thévenet, and Nicolas Pechnik. Initiation and propagation mechanisms of progressive crushing in carbon-epoxy laminated plates. In *ECCM13 - 13th European Conference on Composite Materials*, Stockholm, Sweden, 2008.

[38] Redouane Lombarkia, Augustin Gakwaya, Dennis Nandlall, Marie-Laure Dano, Julie Lévesque, and Philippe Vachon-Joannette. Experimental investigation and finite-element modeling of the crushing response of hat shape open section composite. *International Journal of Crashworthiness*, 0(0):1–12, 2020.

[39] Yan Tong and Yuanming Xu. Improvement of crash energy absorption of 2d braided composite tubes through an innovative chamfer external triggers. *International Journal of Impact Engineering*, 111:11 – 20, 2018.

[40] G. Belingardi, S. Boria, and J. Obradovic. *Energy Absorbing Sacrificial Structures Made of Composite Materials for Vehicle Crash Design*, pages 577–609. Springer Netherlands, Dordrecht, 2013.

[41] Hiroyuki Hamada and Seeram Ramakrishna. Comparison of static and impact energy absorption of carbon fiber/peek composite tubes. In *Composite Materials: Testing and Design: Twelfth Volume*. ASTM International, 1996.

[42] DC Bannermann and CM Kindervater. Crash energy absorption properties of composite structural elements. *High performance composite materials: New applications and industrial production*, pages 155–167, 1983.

[43] V.M. Karbhari and J.E. Haller. Rate and architecture effects on progressive crush of braided tubes. *Composite Structures*, 43(2):93 – 108, 1998.

[44] Rebecca A Cutting, Federico Rios-Tascon, and Johnathan E Goodsell. Experimental investigation of the crush performance of prepreg platelet molding compound tubes. *Journal of Composite Materials*, 54(27):4311–4324, 2020.

[45] P.H. Thornton. The crush behavior of pultruded tubes at high strain rates. *Journal of Composite Materials*, 24(6):594–615, 1990.

[46] A.G. Mamalis, D.E. Manolakos, and G.L. Viegelahn. Crashworthy behaviour of thin-walled tubes of fibreglass composite materials subjected to axial loading. *Journal of Composite Materials*, 24(1):72–91, 1990.

[47] Matej Vesenjak, Lovre Krstulović-Opara, and Zoran Ren. Mechanical properties of advanced pore morphology foam composites. In Ahmed Elmarakbi, editor, *Advanced Composite Materials for Automotive Applications*, pages 75–98. John Wiley & Sons, Ltd, 2013.

[48] William F. Hosford. *Mechanical Behavior of Materials*, chapter Strain Rate and Temperature Dependence of Flow Stress, page 92–112. Cambridge University Press, 2 edition, 2009.

[49] SM Walley and JE Field. Strain rate sensitivity of polymers in compression from low to high rates. *DYMAT j*, 1(3):211–227, September 1994.

[50] Zhouhua Li and John Lambros. Strain rate effects on the thermomechanical behavior of polymers. *International Journal of Solids and Structures*, 38(20):3549 – 3562, 2001.

[51] Ellen M. Arruda, Mary C. Boyce, and R. Jayachandran. Effects of strain rate, temperature and thermomechanical coupling on the finite strain deformation of glassy polymers. *Mechanics of Materials*, 19(2):193 – 212, 1995.

[52] A.D. Mulliken and M.C. Boyce. Mechanics of the rate-dependent elastic–plastic deformation of glassy polymers from low to high strain rates. *International Journal of Solids and Structures*, 43(5):1331 – 1356, 2006.

[53] D. Rittel. On the conversion of plastic work to heat during high strain rate deformation of glassy polymers. *Mechanics of Materials*, 31(2):131 – 139, 1999.

[54] Bertram Hopkinson. A method of measuring the pressure produced in the detonation of high explosives or by the impact of bullets. *Proceedings of the Royal Society of London. Series A, Containing Papers of a Mathematical and Physical Character*, 89(612):411–413, 1914.

[55] A. Gilat, R. K. Goldberg, and G. D. Roberts. High strain rate response of epoxy in tensile and shear loading. *J. Phys. IV France*, 110:123–127, 2003.

[56] Sandeep Tamrakar, Raja Ganesh, Subramani Sockalingam, Bazle Z Haque, and John W Gillespie. Experimental investigation of strain rate and temperature dependent response of an epoxy resin undergoing large deformation. *Journal of Dynamic Behavior of Materials*, 4(1):114–128, 2018.

[57] Takeshi Iwamoto, Toshimasa Nagai, and Toshiyuki Sawa. Experimental and computational investigations on strain rate sensitivity and deformation behavior of bulk materials made of epoxy resin structural adhesive. *International Journal of Solids and Structures*, 47(2):175 – 185, 2010.

[58] T. Gómez-del Río and J. Rodríguez. Compression yielding of epoxy: Strain rate and temperature effect. *Materials Design*, 35:369 – 373, 2012. New Rubber Materials, Test Methods and Processes.

[59] T.E. Tay, H.G. Ang, and V.P.W. Shim. An empirical strain rate-dependent constitutive relationship for glass-fibre reinforced epoxy and pure epoxy. *Composite Structures*, 33(4):201 – 210, 1995.

[60] Gary L. Farley. The effects of crushing speed on the energy-absorption capability of composite tubes. *Journal of Composite Materials*, 25(10):1314–1329, 1991.

[61] Okenwa I Okoli. The effects of strain rate and failure modes on the failure energy of fibre reinforced composites. *Composite Structures*, 54(2):299 – 303, 2001. Third International Conference on Composite Science and Technology.

[62] George C. Jacob, J. Michael Starbuck, John F. Fellers, Srdan Simunovic, and Raymond G. Boeman. Strain rate effects on the mechanical properties of polymer composite materials. *Journal of Applied Polymer Science*, 94(1):296–301, 2004.

[63] Experimental study of strain-rate-dependent behavior of carbon/epoxy composite. *Composites Science and Technology*, 62(10):1469 – 1476, 2002.

[64] Zheyi Zhang, Shujuan Hou, Yiqi Mao, Liping He, and Xu Han. Rate-related study on the ply orientation of carbon fiber reinforced epoxy composite laminates. *International Journal of Mechanical Sciences*, 188:105968, 2020.

[65] M.W. Joosten, C. Hirth, R. Thomson, and H. Koerber. Effect of environmental conditions on the failure mechanisms and energy absorption of open-section crush elements under quasi-static loading. *Composite Structures*, 209:747 – 753, 2019.

[66] Zian Jia, Tiantian Li, Fu pen Chiang, and Lifeng Wang. An experimental investigation of the temperature effect on the mechanics of carbon fiber reinforced polymer composites. *Composites Science and Technology*, 154:53 – 63, 2018.

[67] Jiayi Liu, Wufeng Qiao, Jingxi Liu, De Xie, Zhengong Zhou, Linzhi Wu, and Li Ma. High temperature indentation behaviors of carbon fiber composite pyramidal truss structures. *Composite Structures*, 131:266 – 272, 2015.

[68] Ileana Panaitescu, Thomas Koch, and Vasiliki-Maria Archodoulaki. Effects of temperature, humidity and automotive fluids exposure on glass fiber/polyurethane composites. *Polymer Composites*, 40(6):2357–2367, 2019.

[69] Renaud Gutkin and Silvestre T Pinho. Combining damage and friction to model compressive damage growth in fibre-reinforced composites. *Journal of Composite Materials*, 49(20):2483–2495, 2015.

[70] Thomas Bru, Paul Waldenström, Renaud Gutkin, Robin Olsson, and Gaurav M Vyas. Development of a test method for evaluating the crushing behaviour of unidirectional laminates. *Journal of Composite Materials*, 51(29):4041–4051, 2017.

[71] D. Dalli, L.F. Varandas, G. Catalanotti, S. Foster, and B.G. Falzon. Assessing the current modelling approach for predicting the crashworthiness of formula one composite structures. *Composites Part B: Engineering*, 201:108242, 2020.

[72] Thomas Bru, R Olsson, GM Vyas, S Costa, and Swerea SICOMP. Validation of a novel model for the compressive response of frp: experiments with different fibre orientations. *Proceedings of the 21st International Conference on Composite Materials ICCM-21 (Xi'an, China, 20-25 August 2017)*, 2017.

[73] Sérgio Costa, Martin Fagerström, and Robin Olsson. Development and validation of a finite deformation fibre kinking model for crushing of composites. *Composites Science and Technology*, 197:108236, 2020.

[74] Wei Tan and Brian G. Falzon. Modelling the crush behaviour of thermoplastic composites. *Composites Science and Technology*, 134:57 – 71, 2016.

[75] Paolo Feraboli, Bonnie Wade, Francesco Deleo, and Mostafa Rassaian. Crush energy absorption of composite channel section specimens. *Composites Part A: Applied Science and Manufacturing*, 40(8):1248 – 1256, 2009. Special Issue: 15th French National Conference on Composites - JNC15.

[76] Qiang Liu, Zhengyan Ou, Zhengwei Mo, Qing Li, and Dapeng Qu. Experimental investigation into dynamic axial impact responses of double hat shaped cfrp tubes. *Composites Part B: Engineering*, 79:494 – 504, 2015.

[77] S. Boria, A. Scattina, and G. Belingardi. Axial energy absorption of cfrp truncated cones. *Composite Structures*, 130:18 – 28, 2015.

[78] J André Lavoie. Design and application of a quasistatic crush test fixture for investigating scale effects in energy absorbing composite plates. Master's thesis, Virginia Polytechnic Institute and State University, 1993.

[79] Karen Jackson, John Morton, J. Andre´Lavoie, and Richard Boitnott. Scaling of energy absorbing composite plates. *Journal of the American Helicopter Society*, 39(1), 1994.

[80] J.André Lavoie and Sotiris Kellas. Dynamic crush tests of energy-absorbing laminated composite plates. *Composites Part A: Applied Science and Manufacturing*, 27(6):467 – 475, 1996.

[81] Dean D. Dubey and Anthony J. Vizzini. Energy absorption of composite plates and tubes. *Journal of Composite Materials*, 32(2):158–176, 1998.

[82] L Daniel, P.J Hogg, and P.T Curtis. The relative effects of through-thickness properties and fibre orientation on energy absorption by continuous fibre composites. *Composites Part B: Engineering*, 30(3):257 – 266, 1999.

[83] L Daniel, P.J Hogg, and P.T Curtis. The crush behaviour of carbon fibre angle-ply reinforcement and the effect of interlaminar shear strength on energy absorption capability. *Composites Part B: Engineering*, 31(5):435 – 440, 2000.

[84] George C. Jacob, J. Michael Starbuck, Srdan Simunovic, and John F. Fellers. New test method for determining energy absorption mechanisms in polymer composite plates. *Polymer Composites*, 24(6):706–715, 2003.

[85] George C. Jacob, John F. Fellers, J. Michael Starbuck, and Srdan Simunovic. Crashworthiness of automotive composite material systems. *Journal of Applied Polymer Science*, 92(5):3218–3225, 2004.

[86] Paolo Feraboli. Development of a corrugated test specimen for composite materials energy absorption. *Journal of Composite Materials*, 42(3):229–256, 2008.

[87] Graham Heeps. Carbon footprint. *Crash Test Technology International*, 2(1):36–40, 2012.

[88] Paolo Feraboli. Development of a modified flat-plate test specimen and fixture for composite materials crush energy absorption. *Journal of Composite Materials*, 43(19):1967–1990, 2009.

[89] Francesca Garattoni. *Crashworthiness and composite materials: development of an experimental test method for the energy absorption determination and implementation of the relative numerical model*. PhD thesis, ALMA MATER STUDIORUM - Università di Bologna, May 2011.

[90] ASTM D7136/D7136M - 15, Standard Test Method for Measuring the Damage Resistance of a Fiber-Reinforced Polymer Matrix Composite to a Drop-Weight Impact Event. Standard, ASTM International, West Conshohocken, PA, 2015.

[91] ASTM D7137/D7137M - 17, Standard Test Method for Compressive Residual Strength Properties of Damaged Polymer Matrix Composite Plates. Standard, ASTM International, West Conshohocken, PA, 2017.

[92] Nico Feindler. *Charakterisierungs- und Simulationsmethodik zum Versagensverhalten energieabsorbierender Faserverbundstrukturen*. PhD thesis, Technische Universität München, München, 2012.

[93] J. Lausch, M. Takla, and H.-G. Schweiger. Crush testing approach for flat-plate fibrous materials. *Composites Part B: Engineering*, 200:108333, 2020.

[94] NEMA LI 1-1998 (R2011): Industrial Laminated Thermosetting Products. Technical report, National Electrical Manufacturers Association, 1998.

[95] ASTM D3039 / D3039M-17, Standard Test Method for Tensile Properties of Polymer Matrix Composite Materials. Standard, ASTM International, West Conshohocken, PA, 2017.

[96] Paolo Feraboli. Development of a modified flat-plate test specimen and fixture for composite materials crush energy absorption. *Journal of composite materials*, 43(19):1967–1990, 2009.

[97] Iman Babaei, Ravin Garg, Lorenzo Vigna, Davide Salvatore Paolino, Giovanni Belingardi, Lucio Cascone, Andrea Calzolari, and Giuseppe Galizia. Newly developed anti-buckling fixture to assess the in-plane crashworthiness of flat composite specimens. *Applied Sciences*, 10(21):7797, 2020.

[98] Paolo Feraboli. Development of a modified flat-plate test specimen and fixture for composite materials crush energy absorption. *Journal of composite materials*, 43(19):1967–1990, 2009.

[99] J André Lavoie. *Design and application of a quasistatic crush test fixture for investigating scale effects in energy absorbing composite plates*, volume 4526. NASA, 1993.

[100] L Daniel, PJ Hogg, and PT Curtis. The relative effects of through-thickness properties and fibre orientation on energy absorption by continuous fibre composites. *Composites Part B: Engineering*, 30(3):257–266, 1999.

[101] Instron 9400 Series Impact Drop Tower System. Technical report, Instron, 2020.

[102] Lorenzo Vigna, Iman Babaei, Ravin Garg, Giovanni Belingardi, Davide Salvatore Paolino, Andrea Calzolari, and Giuseppe Galizia. An innovative fixture for testing the crashworthiness of composite materials. *Frattura ed Integrità Strutturale*, 15(55):76–87, 2020.

[103] S. Boria, J. Obradovic, and G. Belingardi. Experimental and numerical investigations of the impact behaviour of composite frontal crash structures. *Composites Part B: Engineering*, 79:20 – 27, 2015.

[104] A.G Mamalis, M. Robinson, D.E. Manolakos, G.A. Demosthenous, M.B. Ioannidis, and J. Carruthers. Crashworthy capability of composite material structures. *Composite Structures*, 37(2):109 – 134, 1997.

[105] Ravin Garg, Iman Babaei, Davide Salvatore Paolino, Lorenzo Vigna, Lucio Cascone, Andrea Calzolari, Giuseppe Galizia, and Giovanni Belingardi. Predicting composite component behavior using element level crashworthiness tests, finite element analysis and automated parametric identification. *Materials*, 13(20):4501, 2020.

[106] ISO 6487:2015 Road Vehicles — Measurement Techniques in Impact Tests — Instrumentation. Standard, International Organization for Standardization, Geneva, CH, 2015.

[107] SAE J211/1–Instrumentation for Impact Test-Part 1-Electronic Instrumentation. Standard, Society of Automotive Engineers, Warrendale, PA, 2014.